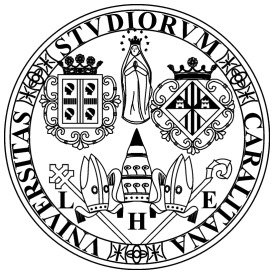

UNIVERSITÀ DEGLI STUDI DI CAGLIARI

DOTTORATO DI RICERCA IN FISICA
Ciclo XXVI

Low mass dimuon production with the ALICE muon spectrometer

Settore scientifico disciplinare di afferenza
Fisica Nucleare, Subnucleare e Astrofisica

Presentata da: Ester Anna Rita Casula
Relatore: Dr. Alessandro De Falco

Esame finale anno accademico 2012-2013

REGIONE AUTONOMA DELLA SARDEGNA

A Ubaldo

Acknowledgments

La presente tesi è stata prodotta durante la frequenza del corso di dottorato in Fisica dell'Università degli Studi di Cagliari, A.A. 2012-2013 - XXVI ciclo, con il supporto di una borsa di studio finanziata con le risorse del P.O.R. SARDEGNA F.S.E. 2007-2013 - Obiettivo competitività regionale e occupazione, Asse IV Capitale Umano, Linea di Attività l.3.1 "Finanziamento di corsi di dottorato finalizzati alla formazione di capitale umano altamente specializzato, in particolare per i settori dell'ICT, delle nanotecnologie e delle biotecnologie, dell'energia e dello sviluppo sostenibile, dell'agroalimentare e dei materiali tradizionali".

Ester Anna Rita Casula gratefully acknowledges Sardinia Regional Government for the financial support of her PhD scholarship (P.O.R. Sardegna F.S.E., Operational Programme of the Autonomous Region of Sardinia, European Social Fund 2007-2013 - Axis IV Human Resources, Objective l.3, Line of Activity l.3.1).

Contents

Introduction

Low mass vector meson (ρ, ω, ϕ) production provides key information on the hot and dense state of strongly interacting matter produced in high-energy heavy ion collisions. Among the different probes, strangeness enhancement can be accessed through the measurement of ϕ meson production, while the measurement of the ϕ nuclear modification factor provides a powerful tool to probe the production dynamics and hadronization process in relativistic heavy ion collisions.

The ϕ meson production in heavy ion collisions has been studied at the CERN Super Proton Synchrotron (SPS) by NA38, CERES, NA49, NA50 and NA60 experiments, and at Brookhaven's Relativistic Heavy Ion Collider (RHIC) by PHENIX and STAR experiments. The results obtained by these experiments present however some discrepancies, such as the measurement of the ϕ R_{AA} (consistent with binary scaling in the intermediate p_T region in central collisions at STAR and suppressed in the same p_T region and centrality at PHENIX).

The aim of this work is the study of ϕ meson production at forward rapidity in pp, p-Pb and Pb-Pb collisions in the muon channel with the ALICE apparatus.

The importance of the pp analysis is mostly related to the necessity of having a baseline for the nucleus-nucleus (A-A) collisions, where the Quark Gluon Plasma is supposed to be formed, while the p-A collisions provide not only a reference for the A-A collisions, but can also give an insight on soft particle production in cold nuclear matter, being a system where no hot, dense medium is formed in the final state, while its initial state is similar to that in A-A collisions.

The data analyzed in the pp analysis were the ones collected by ALICE in 2013: the ϕ differential and integrated cross sections for $1 < p_T < 5$ GeV/c have been extracted.

p-Pb analysis was based on the data collected in 2013 at both forward and backward rapidity: the ϕ yield as a function of p_T, together with the ϕ nuclear modification factor

R_{pPb} as a function of p_T at both forward and backward rapidity, and the yield ratio of forward to backward rapidity R_{FB} in the common rapidity window have been studied. The Pb-Pb data were collected in 2011. The main focus of this analysis has been the study of the ϕ yield and nuclear modification factor R_{AA} as a function of the number of participating nucleons N_{part}.

In Chapter 1 the description of the dominant processes in the dimuon mass spectrum in the low-mass region and the importance of ϕ meson as a probe of the Quark Gluon Plasma, together with the results on ϕ meson production obtained by previous experiments at the SPS and at RHIC are reported.

In Chapter 2 the ALICE apparatus is described, with particular attention to the muon spectrometer.

Chapter 3 describes the parametrization of the Monte Carlo generator used to calculate the acceptance $\times$ efficiency correction.

The results obtained in pp analysis are shown in Chapter 4.

Chapter 5 presents the results obtained in p-Pb analysis, while the Pb-Pb analysis is reported in Chapter 6.

1

Low mass dimuons in heavy ion collisions

Contents

1.1 A brief introduction to Quantum Chromodynamics

According to the *standard model*, besides the gravitational interaction, there are three types of elementary interactions that are mediated by specific bosons. They are the strong, electromagnetic and weak interactions.

The Quantum Chromodynamics (QCD) is the theory that describes strong interactions: according to QCD, the quarks are characterized not just by certain values of spin, charge and momentum, but also by a certain *color charge*, that can assume three different values, red (r), blue (b) and green (g); an anti-quark is different from the corresponding quark because of its anti-color ($\bar{\mathrm{r}}, \bar{\mathrm{b}}, \bar{\mathrm{g}}$) and the opposite sign of the charge and the other quantum numbers.

The bosons that mediate the strong interaction among quarks are called *gluons* and unlike the chargeless photon, they carry color charge. A gluon carries at the same time color and anti-color and according to the Group theory, excluding the "white" combinations, the possible combinations are:

$$r\bar{g}, r\bar{b}, g\bar{b}, g\bar{r}, b\bar{r}, b\bar{g}, \sqrt{\tfrac{1}{2}}(r\bar{r} - g\bar{g}), \sqrt{\tfrac{1}{6}}(r\bar{r} + g\bar{g} - 2b\bar{b}).$$

They correspond to a gluon octet. The interactions among the particles carrying color (both gluons and quarks) occur via the exchange of the gluons of the octet.
With the color, the quarks acquire one additional degree of freedom, but the fact that we cannot observe quarks as free particles implies that only particles of neutral color (i.e. white) can exist. At low energies, a single quark cannot be teared off from an hadron, because two "colored" objects would result (the quark and what would remain of the original hadron): this is the so called *confinement*. The potential that acts on the quarks grows infinitely with the growing of the distance between the quark and the original hadron and has the form:

$$V = -\frac{4}{3}\frac{\alpha_s \hbar c}{r} + kr, \tag{1.1}$$

where α_s is the strong coupling constant, r is the distance between the partons and k is a constant whose value (experimentally measured) is 0.85 GeV/fm.
Combining a color with its anti-color, or combining the three colors or the three anti-colors, a white state is obtained. The hadrons can be divided into baryons (constituted by three quarks) and mesons (constituted by a quark and an anti-quark).

1.2 Resonances in the low-mass region

A way to obtain hadrons is through e^+e^- collisions in colliders.
The production cross section of dimuons and hadrons in e^+e^- collisions as a function of the centre-of-mass energy $\sqrt{s}$ has a trend that goes as 1/s and it is interrupted by the presence of some peaks, called *resonances* (see fig. 1.1), that are quark-antiquark ($q\bar{q}$) bound states, with a rather short mean lifetime and well defined quantum numbers: they are indeed particles and their masses are equal to the total energy available in the centre-of-mass of the reaction.

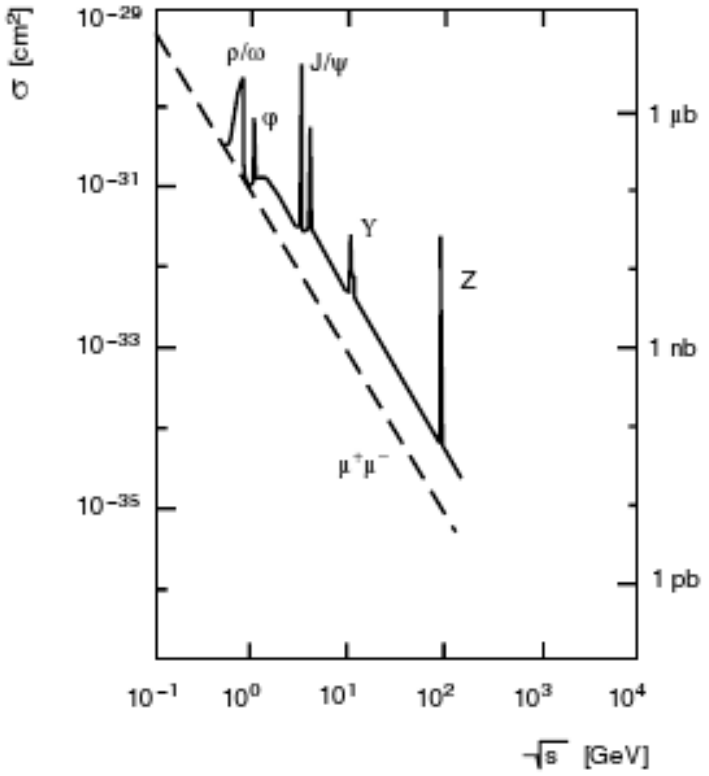

Figure 1.1: Cross sections for the $e^+e^- \to hadrons$ reactions as a function of the centre-of-mass energy $\sqrt{s}$; the dashed line represents the direct dimuon production cross section [1].

Resonances can be produced also in hadron colliders, for instance with a reaction $pp \to R + X$, where R is the resonance. One way to observe them is through their decay into dileptons.

The dominant processes in the dimuon mass spectrum, for invariant masses smaller than 1.5 GeV (the so called *low-mass region*), are the electromagnetic decays of the η, η', ρ, ω and ϕ mesons (see fig. 1.2).

The continuum in the low-mass region is due mostly to the uncorrelated muon pairs coming from the semi-leptonic decays of open charm mesons $D^{\pm} \to \mu^{\pm} + \nu_{\mu}(\bar{\nu}_{\mu})$ and from the Drell-Yan process (in which a quark and an antiquark annihilate, creating a virtual photon or a Z boson that decays then into a pair of opposite-sign leptons).

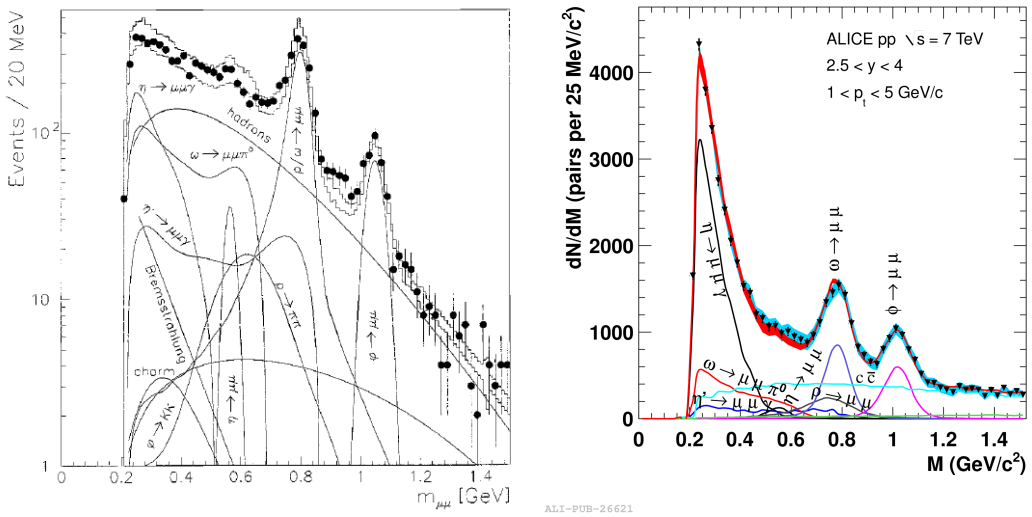

Figure 1.2: Invariant mass spectrum in the low mass region in the dimuon channel as measured by HELIOS-1 experiment in p-Be collisions at 450 GeV/c [2] and by ALICE in pp collisions at 7 TeV [3].

1.2.1 η and η' mesons

η and η' mesons are pseudo-scalar mesons, characterized by total angular momentum J = 0 (together with orbital angular momentum L = 0 and spin angular momentum S = 0); they have negative parity and are a linear combination of the states $u\bar{u}$, $d\bar{d}$ e $s\bar{s}$:

$$\eta = \left(\frac{cos\theta_P}{\sqrt{6}} - \frac{sin\theta_P}{\sqrt{3}}\right) u\bar{u} + \left(\frac{cos\theta_P}{\sqrt{6}} - \frac{sin\theta_P}{\sqrt{3}}\right) d\bar{d} - \left(\frac{cos\theta_P}{\sqrt{6}/2} - \frac{sin\theta_P}{\sqrt{3}}\right) s\bar{s}$$

$$\eta' = \left(\frac{sin\theta_P}{\sqrt{6}} + \frac{cos\theta_P}{\sqrt{3}}\right) u\bar{u} + \left(\frac{sin\theta_P}{\sqrt{6}} + \frac{cos\theta_P}{\sqrt{3}}\right) d\bar{d} - \left(\frac{sin\theta_P}{\sqrt{6}/2} - \frac{cos\theta_P}{\sqrt{3}}\right) s\bar{s}$$

where $\theta_P = 11.5°$ is the mixing angle.

They have a mass of 547.853 ± 0.024 MeV and 957.78 ± 0.06 MeV respectively; considering the muon channel, η meson can decay in the 2-body decay $\mu^+\mu^-$ and both η and η' can decay in $\mu^+\mu^-\gamma$ (*Dalitz* decay).

In the Dalitz decay, η and η' mesons decay in two photons, one of which is virtual and decays in two muons: $\eta \to \gamma^*\gamma \to \mu^+\mu^-\gamma$.

η mesons can also decay with a double Dalitz decay, in which both virtual photons decay in two muons, but this kind of decay has a much smaller branching ratio with respect to the single Dalitz decay.

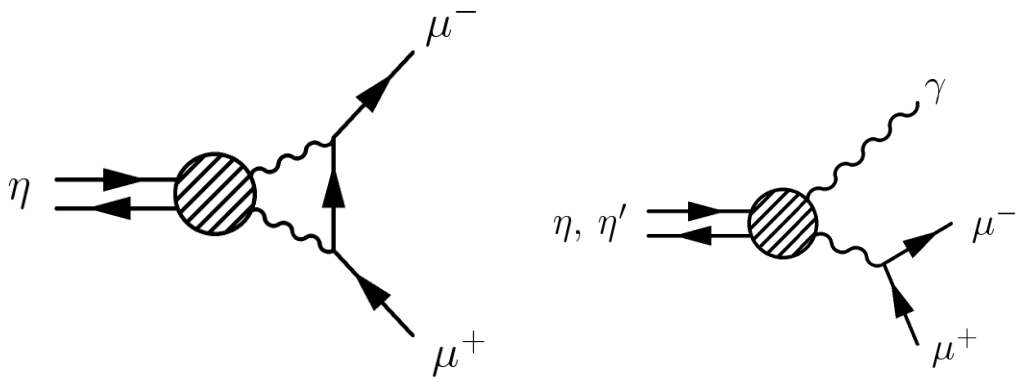

Figure 1.3: Feynman diagrams of 2-body decay (left) and Dalitz decay (right) of η e η'.

The 2-body decay of η' is strongly suppressed, because the branching ratio of a pseudoscalar meson into a lepton pair is proportional to $(m_l/m_p)^2$, where m_l and m_p are the masses of the lepton and of the pseudoscalar meson respectively [4].

1.2.2 ρ, ω and ϕ mesons

ρ, ω and ϕ are vector mesons, characterized by total angular momentum J = 1 (S =1, L = 0) and negative parity.

The peak at 770-780 MeV (see fig. 1.2) is given by the superposition of ρ (mass 775.26 $\pm$ 0.25 MeV) and ω (mass 782.65 $\pm$ 0.12 MeV) resonances. ρ and ω are mixed states of $u\bar{u}$ and $d\bar{d}$ quarks:

$$\rho = \frac{1}{\sqrt{2}}(u\bar{u} - d\bar{d})$$

$$\omega = \frac{1}{\sqrt{2}}(u\bar{u} + d\bar{d})$$

The ϕ meson (mass 1019.455 $\pm$ 0.020 MeV) is a $s\bar{s}$ bound state, characterized by a width of only 4.26 MeV, that implies a rather large mean lifetime (10^{-22} s).

ρ, ω and ϕ decay mostly through the mediation of a virtual photon: $V \to \gamma^* \to \mu^+\mu^-$.

The ω meson presents also a Dalitz decay channel, decaying at first in a neutral pion and a virtual photon, which decays into two muons: $\omega \to \gamma^0\pi^0 \to \mu^+\mu^-\pi^0$ (see fig. 1.4).

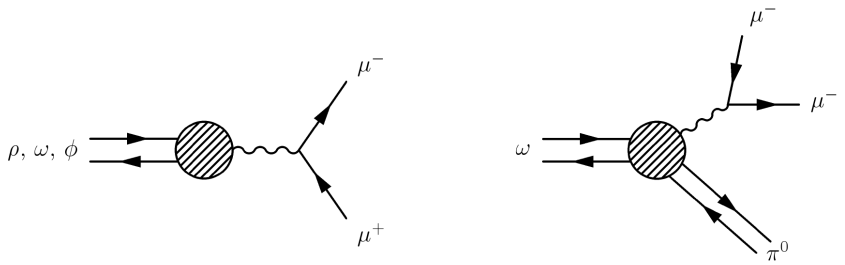

Figure 1.4: Feynman diagrams of the 2-body decay of ρ, ω and ϕ mesons (left) and of the Dalitz decay of the ω meson (right).

1.3 Quark-Gluon Plasma and phase diagram of the strongly interacting matter

As mentioned before, the force that keeps a hadronic system together is too strong, at long distances, to allow us to treat quarks and gluons as essentially free particles.
The strength of the quark-gluon and gluon-gluon coupling is parametrized by the strong coupling constant α_s, whose value is not constant but depends on the energy of the process. At low energies the coupling is so strong that the Perturbation Theory can not be applied to the system; at larger energies (that is, for $E \geq 1$ GeV), the value of α_s decreases, until it becomes small enough to apply the Perturbation Theory.
The energy dependence of the coupling constant corresponds to a dependence on the separation between the partons. For very small distances and correspondingly high values of the energy, α_s decreases, vanishing asymptotically, so that quarks and gluons can be considered "free": this is called *asymptotic freedom*.
This state can be recreated in high energy heavy ion collisions: viewed from the centre-of-mass system, the nuclei approach each other not as symmetric spheres, but as thin, Lorentz contracted disks. The *participating nucleons* are the ones that participate in the collision in the overlap region, while those that are not involved and continue to travel along the direction of the beam axis are called *spectators*.
The time-space evolution of the matter created in heavy ion collisions is shown in fig. 1.5.
Immediately after the impact, the collision system is in a pre-equilibrium state. The participants transfer their original kinetic energy into the system and some of this energy is used for parton production. The hadronic density and the frequency of the

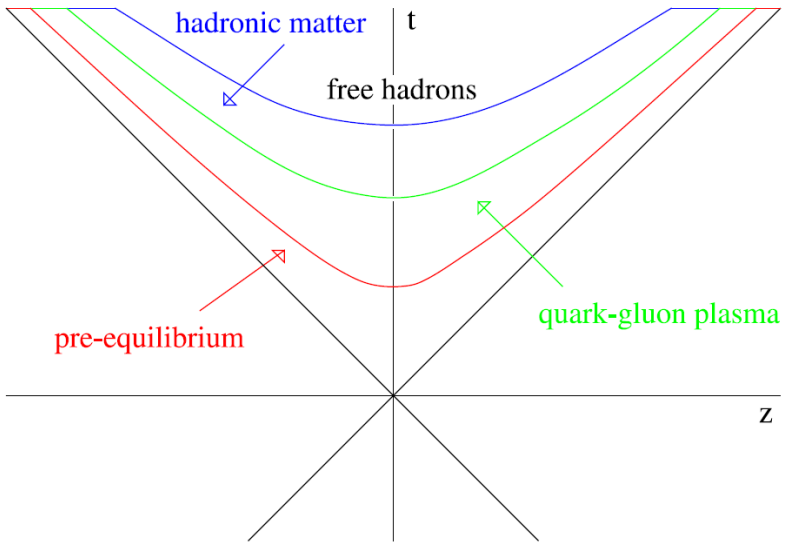

Figure 1.5: Time-space evolution of the matter created in heavy ion collisions [5].

collisions between quarks and gluons increase so much, that the value of α_s decreases and the partons start to act as essentially free particles: this state is known as *Quark-Gluon Plasma* (QGP).

Parton interactions lead to thermal equilibrium during this early stage: the primary, relatively hard gluons produce many soft gluons, which quickly thermalize, and the resulting heat bath draws energy from the remaining hard gluons, leading eventually to thermalization [5][6]. Once equilibrium is achieved, common thermodynamic quantities like temperature and pressure can be used to characterize the system, and its evolution from now on can be modeled by relativistic hydrodynamics.

The high pressure of the plasma makes the fireball expand. As it expands, the temperature drops, eventually crossing the transition temperature ($\sim$ 150-160 MeV) and leading to hadronization from the quarks and the gluons of the plasma. The system at this stage is in fact composed of deconfined quarks and gluons and of hadrons. This mixed phase would exist only if the transition is of the first order. Inelastic collisions between the newly formed hadrons continue to occur until the system cools to the *chemical freeze-out* point. At this point the multiplicity of the newborn particles and so the chemical composition of the fireball are fixed.

Elastic collisions between the hadrons cease at the *thermal freeze-out* point ($\sim$ 100 MeV), when the momentum distributions of all the particles are frozen too.

The thermal freeze-out occurs only after the chemical one, due to the fact that the cross sections of the inelastic processes are much smaller than the ones of the elastic processes (the first are of the order of the mb, while the latter are of the order of the hundred of mb). This is what causes the ceasing of the strong short-range interactions and the freeze-out of the particles spectra.

After the thermal freeze-out, the particles produced in the collision stream freely and can be measured by the detectors. The hot and dense medium created in heavy ion collisions is extremely short-lived ($\sim$ 5-10 fm/c, that is, $\sim 10^{-23}$ s), so that to characterize the system properties, final state observables have to be studied.

The different evolution stages, from primary collisions to freeze-out, require very different probes for their investigation. To make an example, pions appear at the very end, either directly or as decay products of resonances, so they do not retain much of the very early phases of the system; on the contrary, hard Drell-Yan dileptons are produced essentially at the time of the collision and then remain unaffected by the subsequent history of the system: hence they are not able to provide information on thermalization and freeze-out.

The basis for a quark-gluon plasma is the high parton density in the early stages after the collision; this effectively screens all confining long-range forces, so that only short-range interactions remain.

So far, two types of probes have been considered to study the quark-gluon plasma: the *external probes*, produced essentially by primary parton collisions before the existence of any medium, and the *internal probes*, produced by the quark-gluon plasma itself.

The external probes indicate, by their observed behaviour, whether the subsequent medium was deconfined or not. The production of quarkonium states (J/ψ, Υ) provides one of the best known examples of such a probe. Short distance QCD predicts that the dissociation of quarkonia, that results then in their suppression [7], is possible only in a deconfined medium, since it requires harder gluons than those present in hadrons. Another very promising probe to study the QGP are the quarkonia regeneration phenomena, due to the statistical recombination of $q\bar{q}$ pairs emerging from the medium, that are expected to be more and more important as the centre of mass energy increases and a higher number of heavy quarks is produced. A third example of external probe is the energy loss or attenuation of hard jets, which is expected to increase considerably in a deconfined medium (*jet quenching*).

Dileptons and photons produced by the quark-gluon plasma constitute the internal probes: they leave the medium without being affected by its subsequent states, undergoing only weak or electromagnetic interactions after their formation. However, since both can also be produced by a confined medium, they can serve as thermometer of the medium rather than as probe for its confinement status. Even if isolating a possible thermal component is quite challenging, since both dileptons and photons are produced abundantly in hadron decays, this kind of measurements has been performed with good precision at both CERN SPS and RHIC [8][9].

At the present stage, quarkonia dissociation, jet quenching and quarkonia recombination appear anyway the most promising direct signatures for deconfinement [10].

1.3.1 Phase diagram of the strongly interacting matter

The different phases of strongly interacting matter are summarized in fig. 1.6 [5].

Low temperatures and values of baryochemical potential [1] $\mu \sim 1$ GeV (corresponding to the nuclear density) identify the region of the ordinary hadronic matter.

Color deconfinement can be obtained either by compression of the nuclear matter (i.e. increasing μ) or by heating (that is, increasing T).

For sufficiently high values of the baryochemical potential, the system exhibits a first-order transition between hadronic matter and the QGP. Lattice calculations at non-zero chemical potential suggest the existence of a critical point (μ_c, T_c), such that the transition is no longer of the first order for $\mu < \mu_c$.

In particular, lattice calculations show that the nature of the transition for a value of the baryochemical potential $\mu = 0$ would be a crossover [11][12].

At low temperatures and high values of the chemical potential, nuclear matter consists of interacting and degenerate Fermi gas of quarks at high density. The interaction among the quarks can be attractive in specific combinations of color states, leading to the formation of quark-quark pairs, which determine a color superconducting phase.

Besides deconfinement, another phase transition occurs with increasing density: *chiral symmetry restoration.*

[1] In statistical mechanics, the chemical potential is the energy necessary to add (or extract) a particle to a system: $\mu = dE/dN$. The baryochemical potential is directly related to the baryon-number density. For example, in a non-interacting gas of nucleons at zero temperature, $\mu = \epsilon_F \equiv p_F^2/2m \propto \rho^{2/3}$.

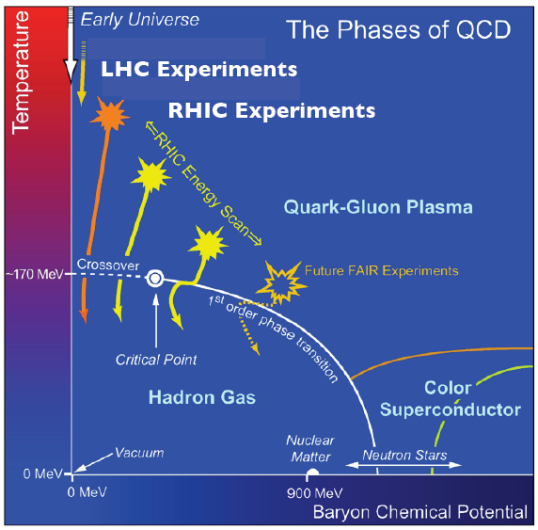

Figure 1.6: Phase diagram for strongly interacting matter [13].

1.3.2 Chiral Symmetry Restoration

When matter passes from confined to deconfined phase, the effective mass of the quarks is expected to change. When they are confined in hadrons, the light quarks acquire through "dressing" with gluons an "effective constituent quark" mass of about 300 MeV. On the other hand, the quarks in the Lagrangian of QCD are almost massless. This means that the mass of the constituent quarks in the confined phase is generated spontaneously, through the confinement interaction itself. Hence it is likely that, when deconfinement occurs, the quarks revert to the intrinsic mass they have in the Lagrangian.

A shift in the effective quark mass is a further transition to look for, as the density of strongly interacting matter increases. Massless fermions possess chiral symmetry: they can be decomposed into independent left- and right-handed massless spin one-half particles. In the case of massive fermions, these two handed components are mixed. In the limit of vanishing quark mass, the confinement interaction must lead to a spontaneous breaking of this symmetry, which should be restored in the deconfined phase (*chiral symmetry restoration*) [5].

With increasing density, it is expected that this critical behavior occurs in strongly interacting matter, leading to deconfinement and chiral symmetry restoration.

While deconfinement is basically the transition from bound to unbound quark constituents, from a state of color-neutral hadrons to one of colored quarks, chiral symmetry restoration is the transition from a state of massive "dressed" constituent quarks to one of massless current quarks. These two phenomena do not need to coincide, and there are theories in which they do not [14][15]: in this case, deconfinement occurs at a much lower temperature than chiral symmetry restoration. However, rather basic arguments suggest that chiral symmetry restoration occurs either together with or after color deconfinement [16].

1.4 ϕ-meson production as a probe of the Quark-Gluon Plasma

ϕ meson is an excellent probe of the Quark-Gluon Plasma, due to its small inelastic cross section for interaction with non-strange hadrons, that makes ϕ less affected by hadronic rescattering during the expanding hadronic phase and reflects better the initial evolution of the system. Hence the ϕ spectra produced during this phase will not be altered during the expanding hadronic phase.

The mechanism for ϕ meson production in high energy heavy ion collisions is still not completely clear. As the lightest bound state of strange quarks, ϕ meson is suppressed in elementary collisions because of the Okubo-Zweig-Iizuka (OZI) rule [17][18][19]. The OZI rule states that processes with disconnected quark lines in the initial and final state are suppressed.

In an environment with many strange quarks, such as the QGP, s and $\bar{s}$ would be produced primarily by gluon-gluon interactions. These interactions occur very rapidly, so that the s abundance approaches soon the equilibrium level. During the hadronization phase, ϕ mesons can be produced through coalescence, not being subjected to the OZI rule anymore. The lifting of OZI suppression, together with the large abundance of s quarks in the plasma, results in a production of ϕ mesons enhanced with respect to the production of other vector mesons of similar mass, like ρ and ω, that are linear combinations of u and d quarks. This means that the $\phi/(\rho + \omega)$ ratio would be a sensitive probe of QGP formation [20][21][22][23].

It was also suggested that the ϕ meson enhancement in heavy ion collisions could have been due to the ϕ meson being produced via $K\bar{K} \rightarrow \phi$ in the hadronic rescattering

stage. Models such as RQMD [24] and UrQMD [25] have predicted an increase of the ϕ to K^- production ratio at midrapidity as a function of the number of participating nucleons, but this prediction was disproved by STAR experiment at RHIC in Au-Au collisions at $\sqrt{s_{NN}} = 200$ GeV [26][27].

The in-medium properties of vector mesons in the hot and dense matter are also interesting: it has been predicted that the mass and width of ϕ could change because of the partial restoration of chiral symmetry in the nuclear medium. In particular, the ϕ mass decreases as a result of many-body effects in the hadronic medium [28][29].

It has also been proposed, as a signature of the phase transition from Quark-Gluon Plasma to the hadronic matter, that a double ϕ peak structure should appear in the dilepton invariant mass spectrum in relativistic heavy ion collisions [30]. The low mass ϕ peak results from the decay of ϕ mesons with reduced in-medium mass during the transition.

Other calculations have predicted that the ϕ meson width can be widened significantly because of the nuclear medium effects [31][32][33].

KEK-PS E325 experiment observed a mass modification of ϕ meson at normal nuclear density in p-A collisions at 12 GeV in the e^+e^- channel [34][35]. The leptonic channel is quite interesting in the study of the in-medium properties of the ϕ with respect to the dominant hadronic channel $\phi \to KK$. In fact, differently from the leptons, the kaons coming from the hadronic channel are unlikely to escape without reacting further, thus destroying any useful information possessed about the ϕ.

The elliptic flow parameter v_2 is another probe to study the Quark Gluon Plasma. STAR experiment observed that the dependence of v_2 on the particle mass at low p_T ($0 < p_T < 2$ GeV/c) in Au-Au collisions at 130 and 200 GeV [36][37] is consistent with hydrodynamic calculations in which local thermal equilibrium of partons has been assumed [38][39][40]. This observation implies the creation of a thermally equilibrated partonic matter. However, at intermediate p_T ($2 < p_T < 5$ GeV/c), v_2 for various hadrons seems to depend on the number of the constituent quarks in the hadron, rather than on its mass: this scenario is consistent with coalescence/recombination models [41][42][43][44]. Being the ϕ a meson with a mass close to that of the proton, the measurement of ϕ elliptic flow should provide a powerful tool for testing this point.

1.4.0.1 Nuclear Modification Factors

Nuclear modification factors are a powerful tool to probe the production dynamics and hadronization process in relativistic heavy ion collisions [42][44][45].
R_{AB} is defined as the yield ratio of nucleus A + nucleus B collisions to inelastic pp collisions, normalized by N_{bin} (that is, the number of binary inelastic nucleon-nucleon collisions determined from Glauber model calculations [46]). It can be written as a function of transverse momentum p_T as well as a function of other variables:

$$R_{AB}(p_T) = \frac{\left[\frac{1}{N_{bin}}\frac{dn}{dp_T}\right]^{A+B}}{\left[\frac{dn}{dp_T}\right]^{pp}} \tag{1.2}$$

R_{cp} is often used instead of R_{AB} in absence of a pp reference to nucleus-nucleus measurement; it is defined as the ratio of the yields in central to peripheral collisions normalized by N_{bin}:

$$R_{cp}(p_T) = \frac{\left[\frac{1}{N_{bin}}\frac{dn}{dp_T}\right]^{central}}{\left[\frac{1}{N_{bin}}\frac{dn}{dp_T}\right]^{peripheral}} \tag{1.3}$$

These factors will be equal to unity if nucleus-nucleus collisions are just simple superpositions of nucleon-nucleon collisions. Deviation from unity may imply contributions from nuclear or Quark-Gluon Plasma effects.
In fact, in absence of medium-induced effects, particle production in nucleus-nucleus collisions should scale with the number of binary collisions in the high p_T region, resulting in $R_{AB} = 1$, while in the low p_T region, the yield is not expected to scale with N_{bin} but with the number of participating nucleons N_{part}, reflecting the bulk properties of the system.
This scaling can be modified when the initial parton distribution is changed in the nuclear environment or when the partons lose energy in the medium prior to fragmentation, resulting in $R_{AB} < 1$.

1.5 Experimental results on ϕ meson

The production of ϕ mesons has been studied systematically at ever increasing $\sqrt{s}$, since the Alternating Gradient Synchrotron (AGS) at the Brookhaven National Laboratory,

with the E802 experiment in Si-Au collisions at 14.6 AGeV and the E917 experiment in Au-Au collisions at 11.7 AGeV. The ϕ production has been studied at the CERN Super Proton Synchrotron (SPS) by NA38, CERES, NA49, NA50 and NA60 experiments, and at Brookhaven's Relativistic Heavy Ion Collider (RHIC) by PHENIX and STAR experiments.

1.5.1 Results from CERN SPS

NA38 and NA50 have studied the production of vector mesons (ρ, ω, ϕ) through their decay into muon pairs in d-C, p-W, d-U, S-S, S-Cu and S-U collisions at 200 AGeV (NA38) and in Pb-Pb collisions at 158 AGeV (NA50).
The relative yield $R = \frac{B_\phi \sigma_\phi}{B_\rho \sigma_\rho + B_\omega \sigma_\omega}$ (from now on indicated as $\phi/(\rho+\omega)$) has been studied for the dimuon transverse momentum region ($0.6 \leq P_{T,\mu\mu} \leq 3.0$ GeV/c) by the NA38 experiment [47]. In order to obtain an integrated result, an extrapolation from $P_{T,\mu\mu} \geq 0.6$ GeV/c was done. The measured ratio is 2.5 times larger in S-U than in p-W collisions, independently of p_T.

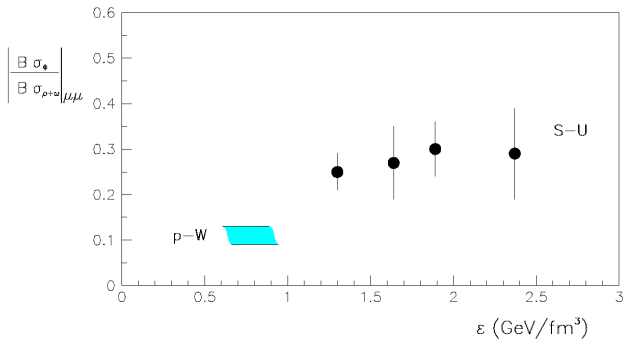

Figure 1.7: NA38 - Ratio $R = \frac{B_\phi \sigma_\phi}{B_\rho \sigma_\rho + B_\omega \sigma_\omega}$ in the dimuon channel, integrated in p_T, as a function of energy density ϵ in S-U collisions, compared with the value in p-W (represented by the shaded area).

The increase of the $\phi/(\rho+\omega)$ ratio depending on the size of the interacting nuclei is clearer in fig. 1.8, where the ratio $\phi/(\rho+\omega)$ is shown as a function of p_T, for transvere mass[1] $m_T > 1.5$ GeV/c^2 in central collisions, for different colliding nuclei. The value of this ratio appears to be constant as a function of p_T [48][49].

[1]The transverse mass is defined as $m_T = \sqrt{m^2 + p_T^2}$.

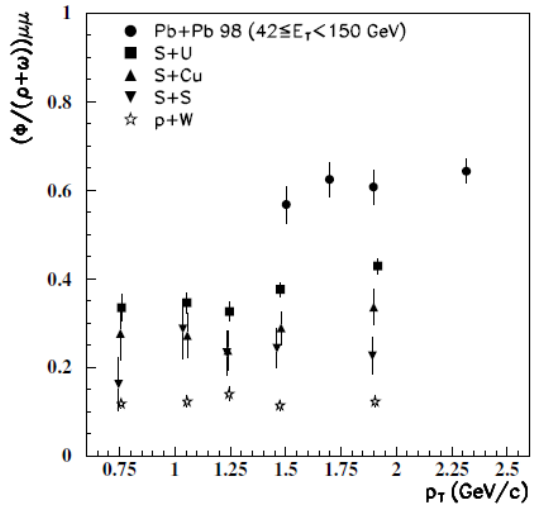

Figure 1.8: NA38/50 - $\phi/(\rho+\omega)$ as a function of p_T for different colliding nuclei, for $m_T > 1.5$ GeV/c^2.

In fig. 1.9 $\phi/(\rho+\omega)$ ratio is shown as a function of the number of participating nucleons N_{part}, for $1.4 < p_T < 3.5$ GeV/c in the case of Pb-Pb collisions and for $0.6 < p_T < 3.0$ GeV/c in the case of the other colliding systems: the ratio increases as a function of N_{part}, up to $N_{part} \sim 250$, where it starts to saturate. This increase can be interpreted as an enhancement of ϕ production with respect to ρ and ω mesons.

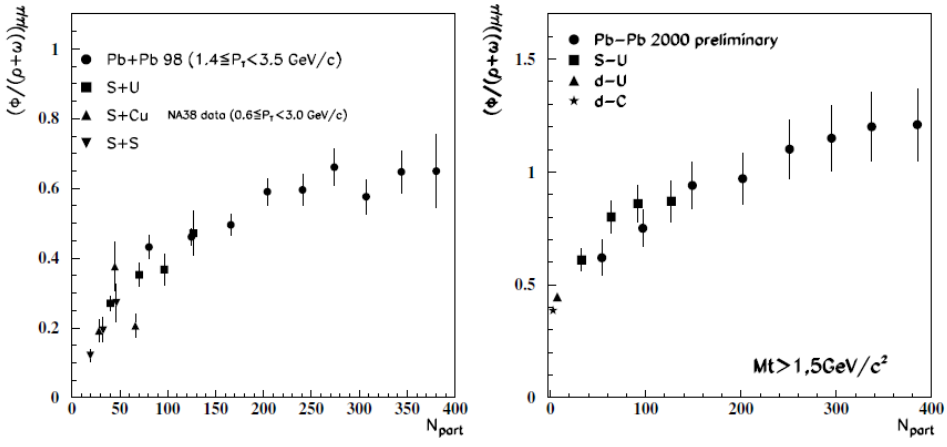

Figure 1.9: NA38/50 - $\phi/(\rho+\omega)$ as a function of N_{part} for different colliding nuclei

NA50 has also measured the ϕ yield as a function of the transverse mass in Pb-Pb central collisions, shown in fig. 1.10, compared with the results obtained by NA49 and

by CERES.

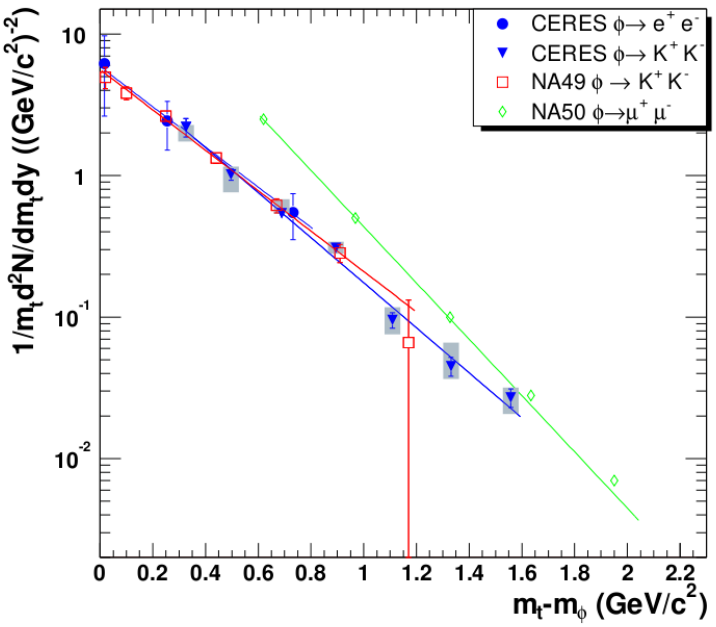

Figure 1.10: Comparison of ϕ transverse mass distribution obtained by CERES, NA49 and NA50 in Pb-Au (CERES) and Pb-Pb (NA49 and NA50) central collisions at 158 AGeV.

NA49 has measured the ϕ meson production in pp, p-Pb and Pb-Pb collisions at various energies from 20 AGeV to 158 AGeV, in the hadronic channel $\phi \to K^+K^-$ [50], while CERES has measured the ϕ meson production in p-Be and p-W collision at 450 GeV per nucleon, in S-Au collisions at 200 GeV per nucleon and in Pb-Au collisions at 40 and 158 GeV per nucleon. The measurements were performed in both the dilepton channel $\phi \to e^+e^-$ and the hadronic channel $\phi \to K^+K^-$ [51].

Fig. 1.10 compares the transverse mass distribution of ϕ meson obtained by CERES in both the dielectron and hadronic channels in Pb-Au central collisions at 158 AGeV, by NA49 in the hadronic channel in Pb-Pb central collisions at 158 AGeV and by NA50 in the dimuon channel in Pb-Pb central collisions at 158 AGeV. CERES results are in agreement with the ones by NA49, while in the case of NA50, the values of the T parameter in the transverse momentum distribution $\frac{dN}{dp_T} \propto p_T e^{-m_T/T}$ are different with respect to the ones obtained by the other two experiments. Moreover, the ϕ multiplicity measured in Pb-Pb collisions by NA50 is higher by about a factor 4 with respect to the

corresponding NA49 one in the K^+K^- channel. This discrepancy, known as ϕ *puzzle*, has not been totally clarified yet: it was argued that in-medium effects may affect the spectral function of the ϕ, causing a modification of its mass and partial decay widths. Moreover, kaon absorption and rescattering in the medium can result in a loss of signal in the region of ϕ invariant mass in the K^+K^- channel, reducing the observed yield. This effect would be concentrated at low p_T, causing a hardening of the p_T spectrum in this channel [52][53]. Anyway, according to those calculations, the yield in lepton pairs is expected to exceed the one in kaons by about 50%, which is much lower than the observed differences.

The NA60 experiment has measured ϕ production in In-In collisions at 158 AGeV, in both the K^+K^- and $\mu^+\mu^-$ channels [54][55].

Fig. 1.11, left side, shows the normalized transverse mass spectra for semicentral and central collisions in the hadronic channel, compared with the corresponding spectra in the dimuon channel.

The ratio $\langle\phi\rangle / \langle N_{part}\rangle$ as a function of $\langle N_{part}\rangle$ in both the $\phi \to K^+K^-$ and $\phi \to \mu^+\mu^-$ channels is shown in fig. 1.11, right side. The yields in the two channels are in agreement within the errors.

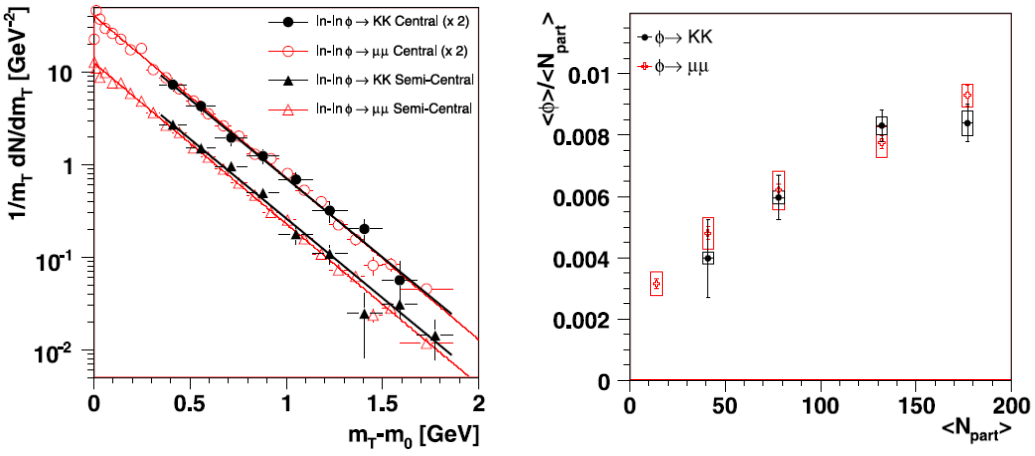

Figure 1.11: NA60 - left side: ϕ transverse mass distribution for central and semicentral collisions in $\phi \to K^+K^-$ and $\phi \to \mu^+\mu^-$ channels; right side: $\langle\phi\rangle / \langle N_{part}\rangle$ as a function of $\langle N_{part}\rangle$ in both channels.

Fig. 1.12 shows both the inverse slope and the $\langle\phi\rangle / \langle N_{part}\rangle$ ratio as a function of $\langle N_{part}\rangle$, for central C-C, Si-Si, In-In and Pb-Pb collisions. The value measured by

NA60 is compared to the ones obtained by CERES, NA49 and NA50. The inverse slope shows an initial fast increase at low $\langle N_{part} \rangle$ values, that becomes less pronounced going towards higher $\langle N_{part} \rangle$. NA50 observed a lower value with respect to the CERES and NA49 measurements in Pb-Pb and to the NA60 ones in In-In collisions in both the hadronic and dimuon channels.

Concerning the $\langle \phi \rangle$ / $\langle N_{part} \rangle$ ratio, the NA50 measurement exceeds by at least a factor of ~ 2 the central Pb-Pb values obtained by NA49 and CERES. Moreover, the CERES measurement in dielectrons and kaon pairs are in agreement within the errors, excluding a yield in dileptons exceeding the one in kaons by more than 60% at a 95% C.L.

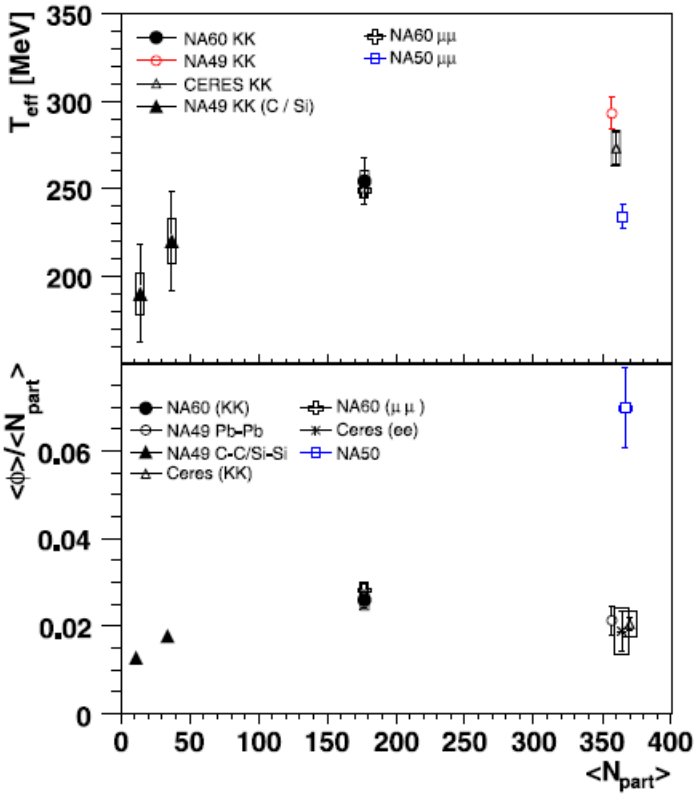

Figure 1.12: NA60 - inverse slope T_{eff} (top) and $\langle \phi \rangle$ / $\langle N_{part} \rangle$ ratio (bottom) as a function of $\langle N_{part} \rangle$, for central C-C, Si-Si, In-In and Pb-Pb collisions. Values from NA60 are compared with CERES, NA49 and NA50 results.

1.5.2 Results from RHIC

The STAR experiment has measured ϕ meson production via the hadronic decay channel $\phi \to K^+K^-$ in Au-Au collisions at $\sqrt{s_{NN}} = 62.4$, 130 and 200 GeV, and in pp and d-Au collisions at $\sqrt{s_{NN}} = 200$ GeV.
In particular, STAR has measured the ϕ nuclear modification factors R_{cp} and R_{AB}.

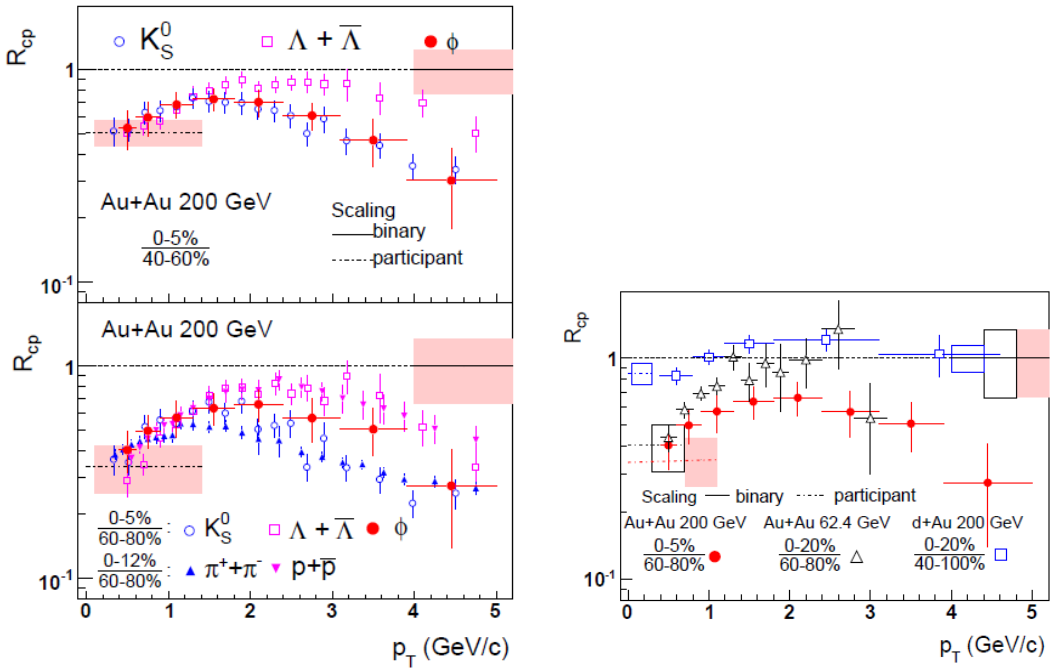

Figure 1.13: STAR - left side: top panel: ϕ R_{cp} with respect to midperipheral collisions, compared with the R_{cp} of $\Lambda + \overline{\Lambda}$ and K^0_S; bottom panel: ϕ R_{cp} with respect to most peripheral collisions, compared with the R_{cp} of $\Lambda + \overline{\Lambda}$, K^0_S, $\pi^+ + \pi^-$ and pp. Right side: ϕ R_{cp} as a function of p_T for Au-Au collisions at 62.4 and 200 GeV, compared with d-Au collisions at 200 GeV. The rectangular bands represent the uncertainties of binary and participant scalings.

ϕ R_{cp} as a function of p_T in Au-Au collisions at 200 GeV is shown on the left side of fig.1.13. The top panel shows the values of ϕ R_{cp} with respect to midperipheral collisions, compared with the R_{cp} of $\Lambda + \overline{\Lambda}$ and K^0_S. The bottom panel shows ϕ R_{cp} with respect to most peripheral collisions, compared with the R_{cp} of $\Lambda+\overline{\Lambda}$, K^0_S, $\pi^+ + \pi^-$ and pp [27].
In the measured p_T region, the ϕ R_{cp} is consistent with N_{part} scaling at lowest p_T (represented in the figure by the dot-dashed line) and is significantly suppressed relative

to the binary collision scale (dashed horizontal line at unity in the figure) for all values of p_T in Au+Au collisions at 200 GeV. Comparing ϕ R_{cp} with the one of $\Lambda + \overline{\Lambda}$ and K^0_S measured by STAR as well, ϕ R_{cp} is similar to that of K^0_S, especially for the case 0-5%/40-60%, rather than to the R_{cp} of Λ, which has a similar mass but is a baryon. For 0-5%/60-80%, ϕ R_{cp} sits between those of Λ and K^0_S. This may be attributed to the shape change of the ϕ p_T spectra from exponential at 40-60% centrality to Levy-Tsallis[1] at 60-80% centrality observed at STAR, which may be due to the change of the ϕ production mechanism at intermediate p_T in different environments.

Fig.1.13, right side, shows ϕ R_{cp} as a function of p_T in Au-Au collisions at 62.4 and 200 GeV and in d-Au collisions at 200 GeV. From this plot we can see that the R_{cp} follows N_{part} scaling at low p_T for the three collision systems. However, at intermediate p_T R_{cp} is strongly suppressed in Au-Au collisions at 200 GeV, weakly suppressed in Au-Au collisions at 62.4 GeV and not suppressed in d-Au collisions at 200 GeV. This measurement can support the partonic coalescence/recombination scenario at intermediate p_T [43][45], where the centrality dependence of the particle yield depends on the number of constituent quarks, rather than on the mass of the particle.

ϕ R_{AB} as a function of p_T for Au-Au and d-Au most central collisions at 200 GeV is shown in fig. 1.14, compared with the R_{dAu} of $\pi^+ + \pi^-$ and $p + \bar{p}$. R_{dAu} for ϕ follows a similar trend as $\pi^+ + \pi^-$ and $p + \bar{p}$ at intermediate p_T, with the same enhancement attributed to the Cronin effect [56][57][58]. R_{AA} in Au-Au collisions at 200 GeV is instead lower than in d-Au at the same energy, and consistent with the binary collision scaling at intermediate p_T.

PHENIX has measured the ϕ meson production in the $\phi \to K^+K^-$ channel on pp, d-Au, Cu-Cu and Au-Au collisions at $\sqrt{s_{NN}} = 200$ GeV.

Fig. 1.15, shows the ϕ nuclear modification factor R_{AA} as a function of p_T in Au-Au collisions at 200 GeV, compared with the R_{AA} of π^0, $K^+ + K^-$, $p + \bar{p}$ and η. ϕ meson exhibits a different suppression pattern with respect to the one of lighter non-strange mesons and baryons. In most central collisions (see top panel), ϕ R_{AA} shows less suppression than π^0 and η in the intermediate p_T range of $2 < p_T < 5$ GeV/c, while at higher p_T values, $p_T > 5$ GeV/c, the ϕ R_{AA} becomes comparable to the one of π^0 and η. The behaviour of ϕ R_{AA} as a function of p_T compared with the R_{AA} π^0 is similar

[1]The Levy-Tsallis function is defined as $f_{Levy} = p_T \frac{A(n-1)(n-2)}{nT[nT+M(n-2)]} \left[1 + \frac{m_T - M}{nT}\right]^{-n}$. Here M is the ϕ meson mass, m_T is the transverse mass, A, n and T are the free parameters.

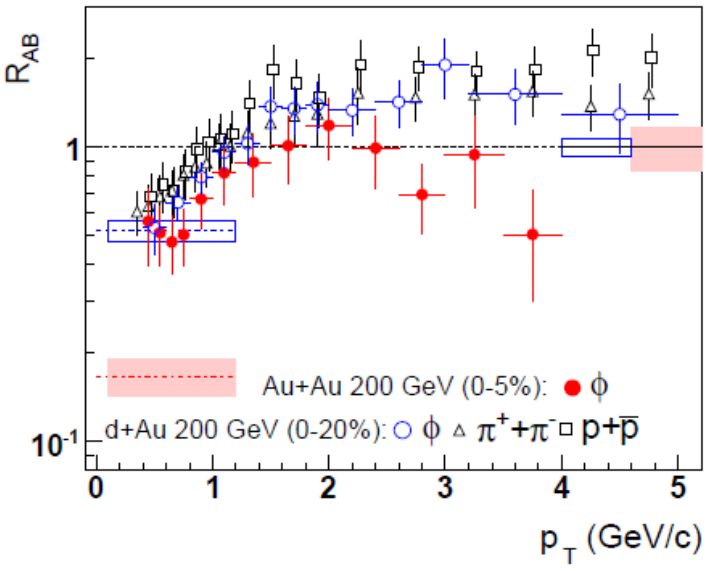

Figure 1.14: STAR - ϕ R_{AB} as a function of p_T for Au-Au and d-Au collisions at 200 GeV, compared with $\pi^+ + \pi^-$ and $p + \bar{p}$ values. Rectangular bands represent the uncertainties of binary (solid line) and participant (dot-dash line) scalings.

also in semi-central (central panel) and peripheral Au-Au collisions (bottom panel). In particular, π^0 is slightly suppressed at a level of $\sim 20\%$ in peripheral collisions, whereas the ϕ is not suppressed.

The $K^+ + K^-$ data in central collisions cover only a very limited range at low $p_T < 2$ GeV/c, but in this range they seem to follow the ϕ R_{AA} trend better than that of π^0 and η. $p+\bar{p}$ show instead no suppression but rather an enhancement at $p_T > 1.5$ GeV/c in central collisions, whereas the ϕ meson is suppressed. The difference between ϕ and protons disappears in the most peripheral collisions, where their R_{AA} is very similar (see bottom panel).

PHENIX results for ϕ R_{AA} in Au-Au collisions differ from the ones obtained by the other RHIC experiment, STAR, which showed that the R_{AA} is consistent with binary scaling in the intermediate p_T region where R_{cp} shows a remarkable suppression, due to the higher invariant p_T yield measured by STAR of almost a factor of 2 with respect to PHENIX.

Fig. 1.16 shows ϕ R_{AA} as a function of N_{part} for $p_T > 2.2$ GeV/c in Cu-Cu and Au-Au collisions. The fact that there is no difference in the R_{AA} between the two systems

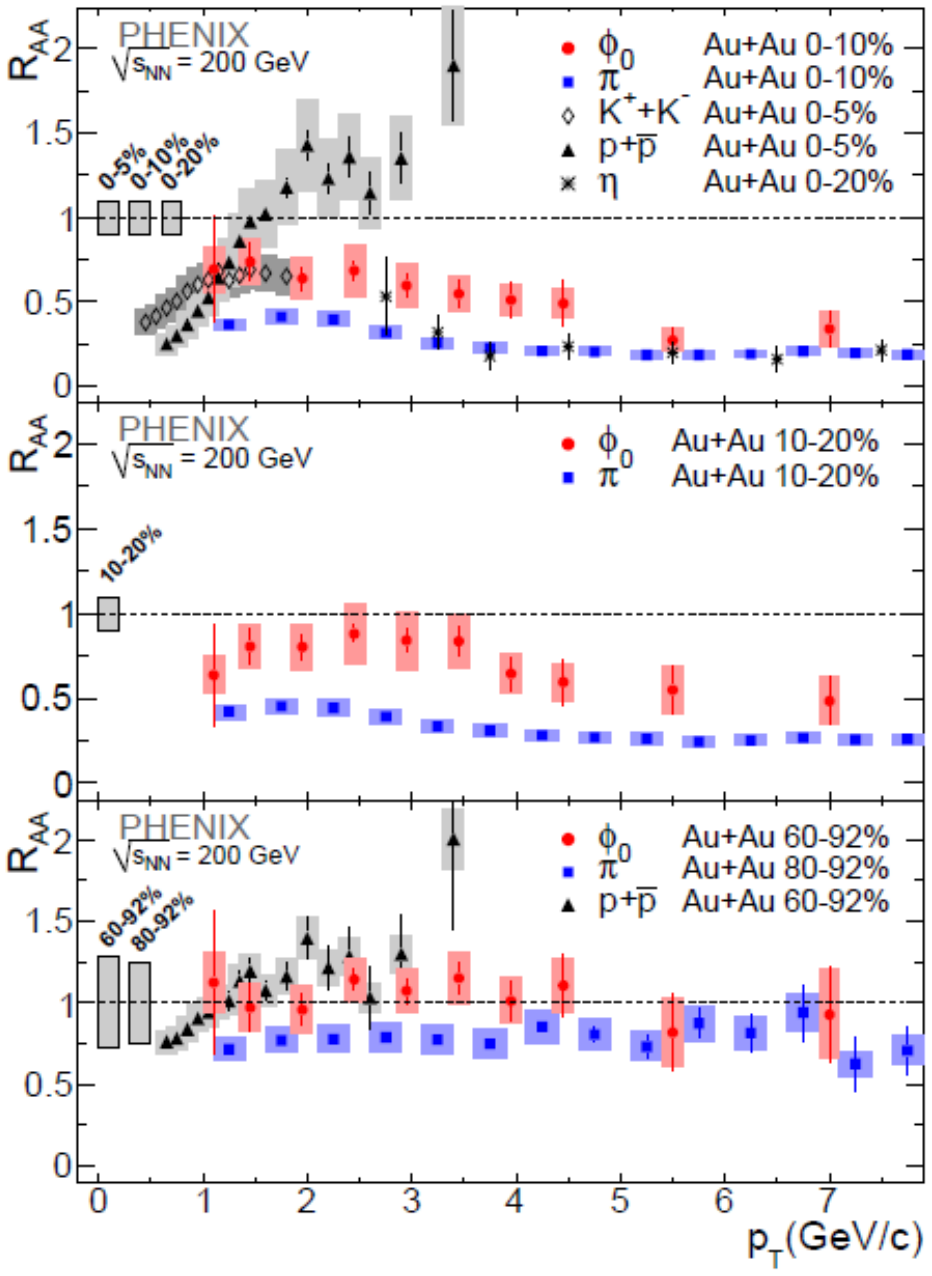

Figure 1.15: PHENIX - ϕ R_{AA} of ϕ, π^0, $K^+ + K^-$, $p + \bar{p}$ and η as a function of p_T in Au-Au collisions for different centralities. The uncertainty in the determination of $\langle N_{coll} \rangle$ is shown as a box on the left.

indicates that it scales with the average size of the colliding system [59].

Fig. 1.17 shows the R_{dAu} as a function of p_T in central d-Au collisions at $\sqrt{s} = 200$

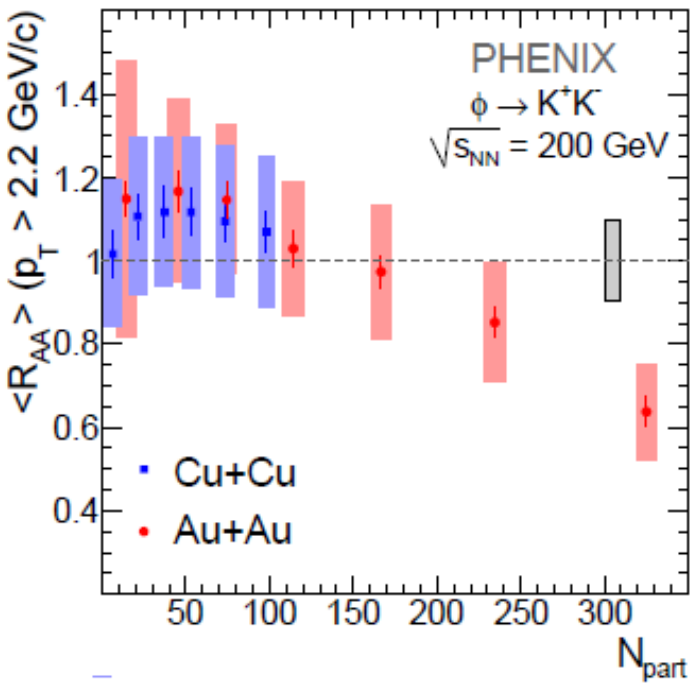

Figure 1.16: PHENIX - ϕ R_{AA} as a function of N_{part} in Au-Au and Cu-Cu collisions at $\sqrt{s}$ = 200 GeV. The uncertainty in the determination of $\langle N_{coll} \rangle$ is shown as a box on the left.

GeV of ϕ, π^0 and p+$\bar{\text{p}}$ for central (top panel) and peripheral (bottom panel) d-Au collisions. ϕ and π^0 have similar R_{dAu} in both centralities, indicating that cold nuclear effects are not responsible for the differences between ϕ and π^0 seen in Au-Au and Cu-Cu collisions. The proton exhibits instead an enhancement in its R_{dAu} for $2 < p_T < 4$ GeV/c, attributed to the Cronin effect, while ϕ and π^0 R_{dAu} shows little or no enhancement [59].

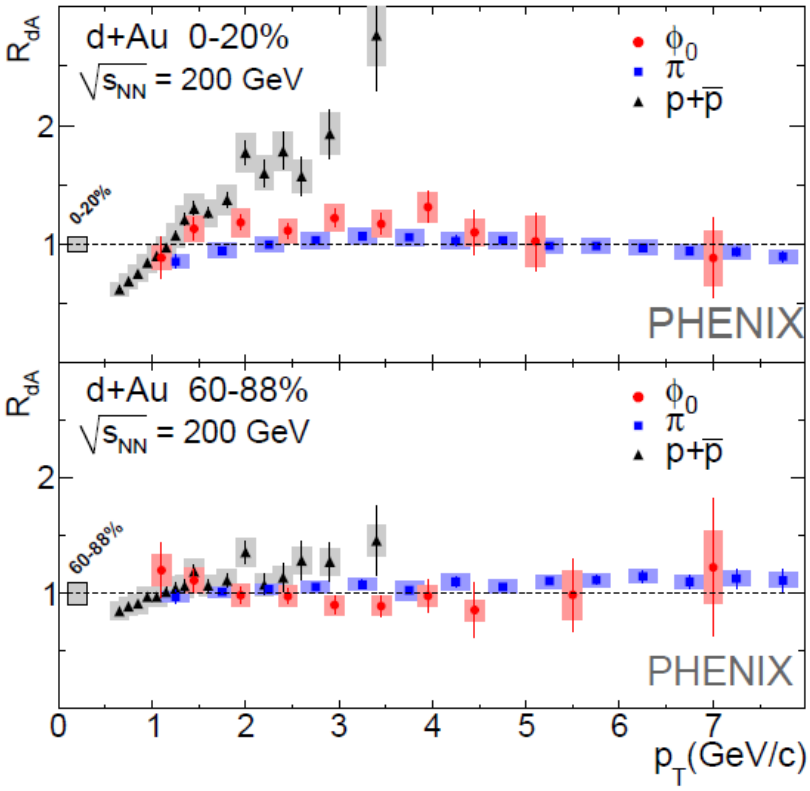

Figure 1.17: PHENIX - Top: R_{dAu} as a function of p_T in central d-Au collisions at $\sqrt{s} =$ 200 GeV of ϕ, π^0 and p+$\bar{\text{p}}$. Bottom: R_{dAu} as a function of p_T in peripheral d-Au collisions at $\sqrt{s} = 200$ GeV. The uncertainty in the determination of $\langle N_{coll} \rangle$ is shown as a box on the left.

2

The ALICE experiment

Contents

2.1 The Large Hadron Collider

The CERN Large Hadron Collider (LHC) is a pp collider, designed to discover the Higgs boson and also to perform heavy ion collisions, reproducing the conditions of the Universe at about 10 μs from the Big Bang and reaching much higher energies with respect to the previous accelerators like LEP, SPS, Tevatron or RHIC.

Built in the same site as the LEP, 100 m underground, 27 km of circumference, LHC has started his activity in 2009, at first with pp collisions at $\sqrt{s}$ = 900 GeV. It has then collected data in pp collisions in 2010 at 7 TeV and in 2012 at 8 TeV. Two short runs at 2.76 TeV were performed in 2011 and 2013. The two runs with Pb-Pb collisions were performed in 2010 and 2011 at 2.76 TeV, while the ones with p-Pb collisions were performed in 2012 and 2013 at 5.02 TeV. The record luminosities achieved are $7.91 \cdot 10^{32}$ cm^{-2}s^{-1} in pp collisions (30 October 2011), $4.27 \cdot 10^{26}$ cm^{-2}s^{-1} in Pb-Pb collisions (5 December 2011) and $1.15 \cdot 10^{29}$ cm^{-2}s^{-1} in p-Pb collisions (10 February 2013). In the future it will run at 14 TeV in pp collisions and at 5.5 TeV in Pb-Pb collisions, with an expected luminosity of 10^{34} cm^{-2}s^{-1} and 10^{27} cm^{-2}s^{-1} respectively.

The major experiments around LHC are ALICE, ATLAS, CMS and LHCb.

LHCb is the experiment dedicated to the study of the B mesons, necessary to explain

the asymmetry between matter and antimatter in the Universe; the aim of ATLAS and CMS is the study of the Higgs boson and of the lightest supersymmetric particles.
ALICE (A Large Ion Collider Experiment) is the experiment dedicated to the study of the heavy ion collisions and of the Quark Gluon Plasma.
A scheme of LHC is shown in fig. 2.1.

2.2 The ALICE detector

ALICE is a general-purpose heavy-ion experiment, with capability of measuring the majority of known observables (such as hadrons, electrons, muons and photons). It was designed to track and identify particles in a wide momentum range (from less than 100 MeV/c up to about 100 GeV/c) and to reconstruct short-living particles such as open heavy flavours and hyperons in a very high multiplicity environment, up to 8000 charged particles per rapidity unit at midrapidity [60][61].
The ALICE detector consists mainly of three parts (see fig. 2.2):

- the *Central Barrel* inside the L3 magnet, covering the pseudorapidity region $|\eta| <$ 0.9 and dedicated to the study of dielectrons, photons and hadrons;
- the muon spectrometer (*Muon Arm*), to detect muons coming from hadrons in the pseudorapidity region -4 $< \eta <$ -2.5;
- the *Forward Detectors*, to evaluate the multiplicity of photons and charged particles and the centrality of the collision, in the pseudorapidity region $\eta > 4$.

2.2.1 The Central Barrel

The Central Barrel is the region inside the L3 magnet. The L3 is a large solenoid (its internal radius is about 5 m), characterized by a magnetic field of 0.5 T.
The Central Barrel is capable of identifying and tracking particles with a transverse momentum down to 80 MeV/c and consists of the following detectors:

- Inner Tracking System (ITS)
- Time Projection Chamber (TPC)

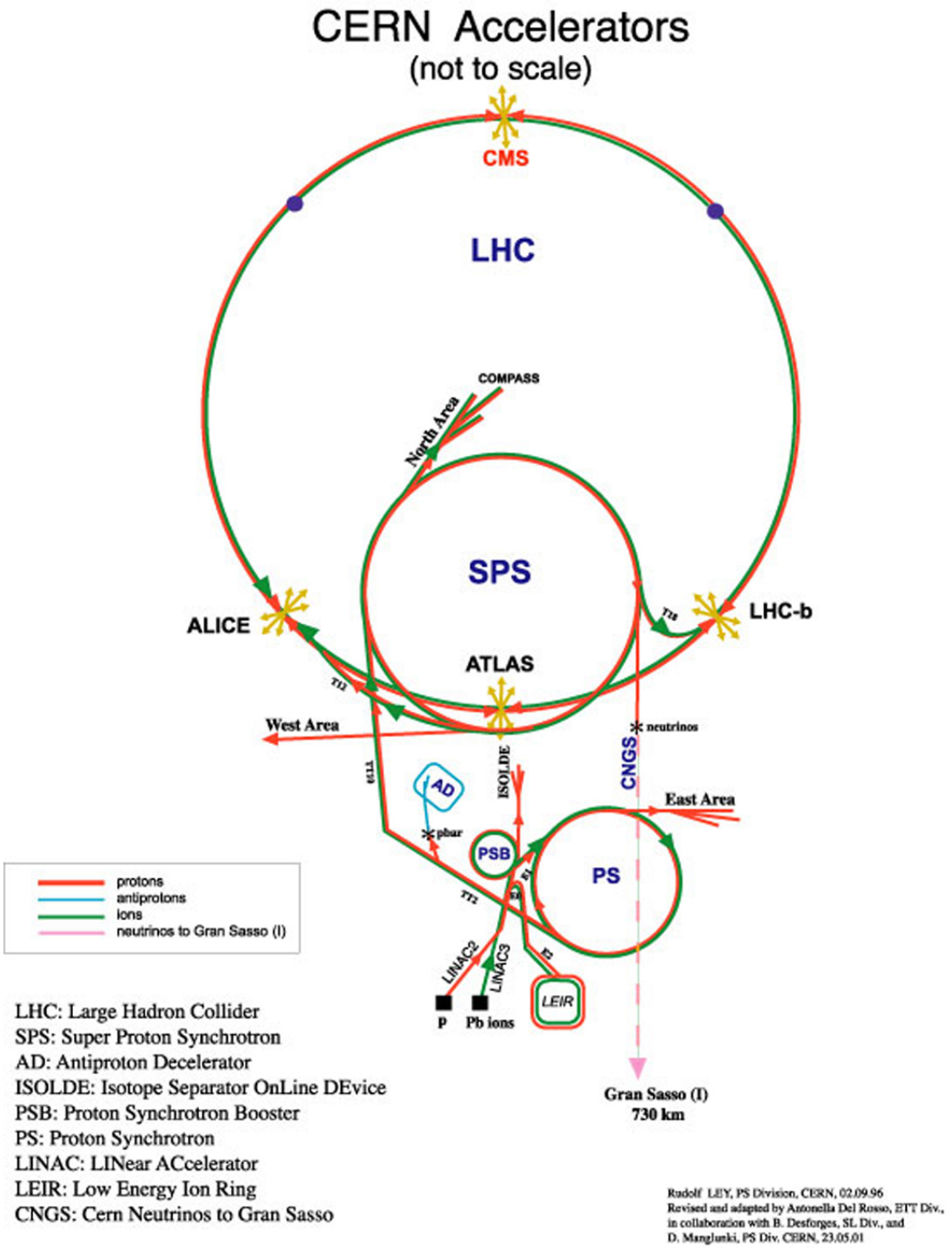

Figure 2.1: Scheme of the Large Hadron Collider

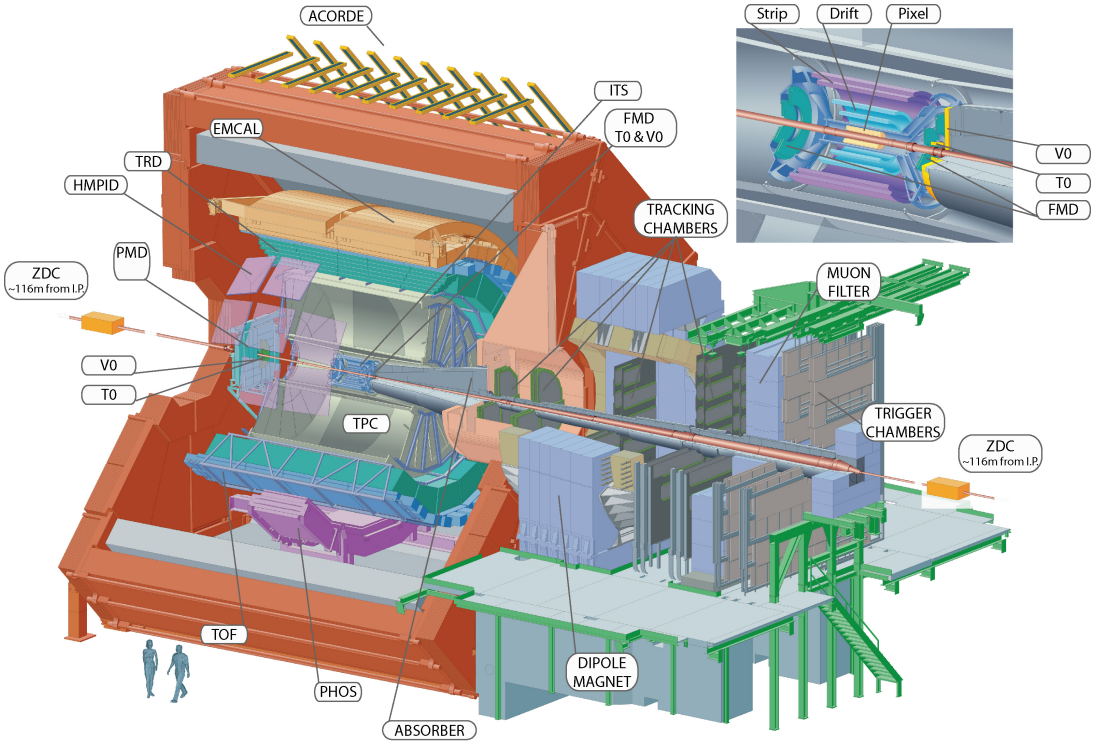

Figure 2.2: Scheme of the ALICE detector

- Transition Radiation Detector (TRD)
- Time Of Flight (TOF)
- High Momentum Particle Identification Detector (HMPID)
- PHOton Spectrometer (PHOS)
- ElectroMagnetic CALorimeter (EMCAL)

The **ITS** allows to determine the primary and secondary vertices of charm and hyperon decays with a resolution better than 60 μm, and to identify and track the particles with a low momentum (p $<$ 80 MeV/c), to improve the momentum and angular resolution for the tracks reconstructed by the TPC or to track the particles that do not reach the TPC. It consists of six cylindrical layers of silicon detectors with a radius varying from 4 to 44 cm, covering the pseudorapidity region $|\eta| < 0.9$. The two inner-most layers are pixel detectors (SPD), while the two intermediate layers are drift detectors (SDD) and the two outer ones are strip detectors (SSD) (see fig. 2.3).

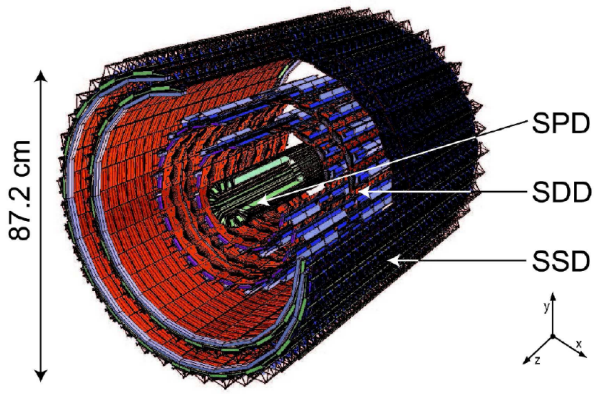

Figure 2.3: Scheme of ALICE ITS

The **TPC** is the main detector of the Central Barrel: it provides particle identification and, together with the TRD and the ITS, it measures the soft and hard probes produced in the dielectron channel, from $p_T \sim 0.1$ GeV/c up to ~ 100 GeV/c; it is also able to distinguish the prompt J/ψ mesons from the ones coming from B meson decays. The low magnetic field (≤ 0.5 T) and a very large volume of the detector, which allows to measure a large section of the track, are what makes possible the identification of both high and low momentum particles.

The TPC has a cylindrical shape, with an internal radius of about 85 cm and an external one of ~ 2.5 m, with a length in the beam direction of 5.1 m. The readout planes are divided in 18 sectors of MWPC.

The gas inside the TPC is a mixture of Ne, CO_2 and N_2. A high voltage electrode divides the gas in two symmetric drift regions, each one of them 250 cm long (fig. 2.4).

The **TRD** identifies the electrons with a momentum greater than 1 GeV/c and in conjuction with the TPC and the ITS, measures the light and heavy vector meson production and the semileptonic decays of hadrons with Open Charm and Beauty.

The detector has a radial position between 2.9 and 3.7 m and consists of 540 modules, organized in 18 supermodules, each one composed of 6 layers of detectors, divided in 5 sections along the beam axis (see fig. 2.5). Each module is made up of a MWPC, a radiator 4.8 cm thick (made of polymethacrylimide foam plates reinforced by glass fibre sheets, with 3.2 cm of polyproylene fibres sandwiched in between) and the readout electronics.

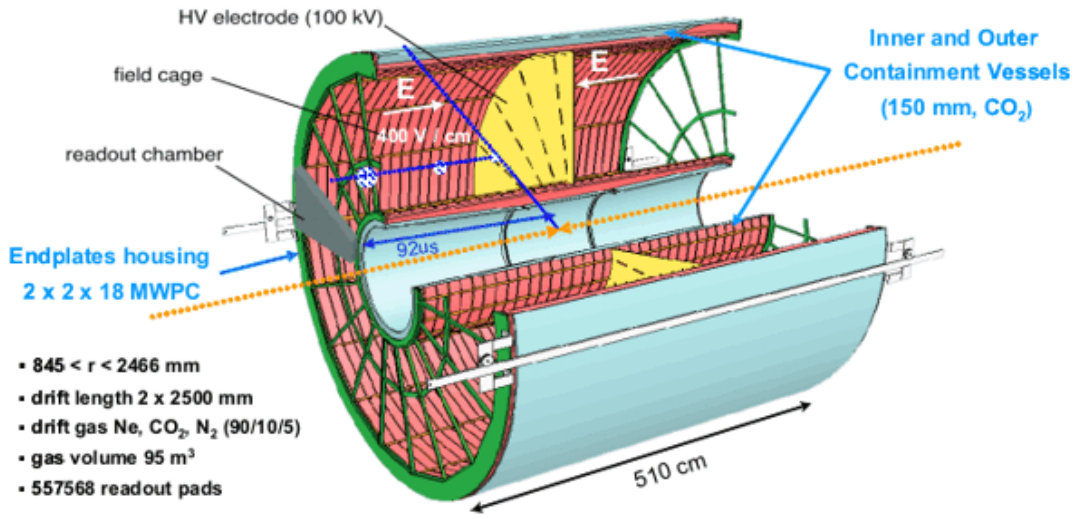

Figure 2.4: Scheme of ALICE TPC

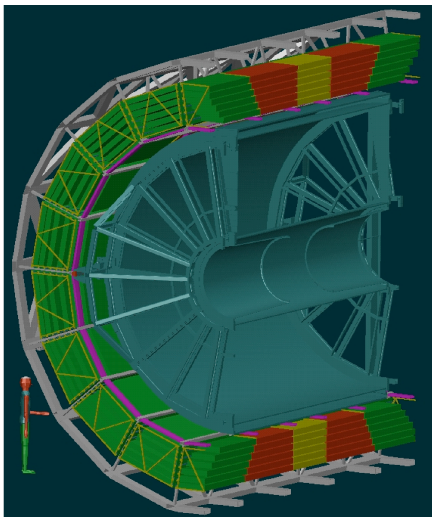

Figure 2.5: Scheme of ALICE TRD

The **TOF** identifies the hadrons with a transverse momentum between 0.5 and 2.5 GeV/c through time-of-flight measurements. Coupled with the ITS and TPC, it provides an event-by-event identification of large samples of pions, kaons and protons. The detector is located at a radial position of 3.7 m and consists of 1638 Multigap Resistive Plate Chambers, organized in 90 modules, sorted in 18 supermodules along the azimuthal angle and in 5 sections along the beam direction, as in the case of the TRD.

The time resolution is 80 ps [62].

The **HMPID** identifies hadrons with $p_T > 1$ GeV/c; it enhances the particle identification capability of ALICE by enabling the identification of particles beyond the momentum interval attainable through energy loss (in ITS and TPC) and time-of-flight measurements (in TOF). The detector is optimized to extend the range for π/K and K/p discrimination, on a track-by-track basis, up to 3 GeV/c and 5 GeV/c respectively. The HMPID is designed as a single-arm array with a pseudo-rapidity acceptance of $|\eta| < 0.5$ and an azimuthal coverage of about 58°, corresponding to 5% of the central barrel phase space; it consists of seven modules of about 1.5×1.5 m^2 RICH (Ring Imaging CHerenkov) counters that detect the Cherenkov light emitted by the particles; it is located near the internal radius of the L3 magnet. The gas inside is C_6F_{14}, transparent to Cherenkov photons in the momentum range between 1 and 5 GeV/c. The photons are detected through a CsI photocatode and a MWPC.

The **PHOS** purpose is the identification of photons and neutral mesons through their two-photon decay channel. The measurement of single photon and di-photon spectra and of Bose-Einstein correlations of direct photons allows to test the properties of the initial phase of the heavy ion collisions, while the detection of high-p_T π^0 allows the investigation of jet quenching as a probe of deconfinement. PHOS is an electromagnetic calorimeter composed of 17280 channels of scintillating PbWO crystals, and a charged particle veto detector consisting of a Multi-Wire Proportional Chamber with cathode-pad readout. They are located in the lower part of the Central Barrel and cover an area of about 8 m^2, corresponding to the pseudorapidity region $|\eta| < 0.12$. The PHOS is capable of measuring photons with a momentum between 0.5 and 10 GeV/c and η mesons with a momentum between 2 and 10 GeV/c.

The **EMCAL** is the last detector added to the ALICE layout; its construction started in 2008. It is located under the ALICE magnet coil at a radius of 4.5 m from the beam line. It covers the pseudorapidity range $|\eta| < 0.7$. The azimuthal acceptance of 107°is limited by the PHOS and the HMPID. It consists of a layered Pb scintillator sampling calorimeter with alternating layers of 1.44 mm of lead and 1.76 mm of polystyrene scintillator. The EMCAL provides a fast and efficient trigger for photons and electrons, and combined with ALICE capabilities to track and identify particles from very low to high p_T, it allows the study of jet interactions in the medium produced in heavy ion collisions.

2.2.2 The Muon Arm

The Muon Arm is the detector dedicated to the study of the muon pairs produced in pp and nucleus-nucleus collisions, paying particular attention to the resonances, like ϕ, J/ψ, Υ. The muon spectrometer has a mass resolution of 55 MeV/c^2 at the ϕ peak. The Muon Arm consists of a big dipole magnet, five tracking stations, two trigger stations, plus a front absorber, a muon filter and a beam shield (see fig. 2.6).

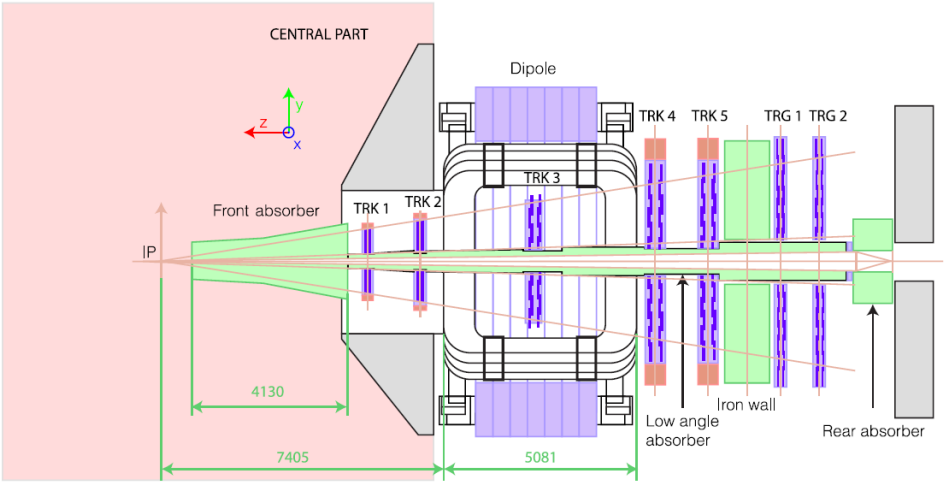

Figure 2.6: Side view of the Muon Arm

2.2.2.1 Absorbers

The three absorbers have been designed to safeguard the detector from the huge particle flux expected in Pb-Pb collisions: about 7000 particles produced inside the spectrometer acceptance and about 6000 particles intercepting the beam-pipe in the region -7 < η < -4.

The **front absorber** covers the pseudorapidity region -4 < η < -2.5; it is located inside the L3 magnet, between the interaction point and the first tracking station, at 90 cm from the interaction point; its length of 4 m corresponds to ten hadronic interaction lengths. The front absorber has the double task of decreasing the background of muons coming from the decay of pions and kaons, absorbing the greater part of these latter

ones before their decay, and attenuating the flux of charged particles by at least two orders of magnitude.
The absorber is designed to provide both a good shielding capability and a limited multiple scattering (which would compromise the spectrometer mass resolution). To obtain this, a low-Z material in the absorber layers close to the vertex, and a high-Z shielding materials at the rear end have been used. A total thickness of 20 cm of Pb interleaved with layers of boronated polyethylene, which can moderate neutrons by quasi-elastic scattering, was chosen for the front part, while lead and tungsten were selected for the rear end. The absorber is completed by a combination of concrete and carbon.
The **muon filter** consists of an iron wall 1.2 m thick, located between the last tracking station and the first trigger station. Its task is to stop the muons with momentum lower than 4 GeV/c, in order to reduce the background due to the decay into muons of kaons and pions, and to improve the performances of the trigger chambers, blocking the hadrons that have not been stopped by the front absorber or that have been produced in the beam pipe, without compromising the spatial resolution of the tracking apparatus.
The **beam shield** protects the detector from the high rapidity secondary particles produced along the beam pipe. It is made of tungsten and lead and it is covered by a layer of stainless steel.

2.2.2.2 Dipole magnet

The dipole magnet (see fig. 2.7) is 5 m long, 6.6 m wide and 8 m high. It provides a maximum central field of 0.7 T and an integral field of 3 Tm. Its aim is to deflect the muons depending on their charge, in order to measure their momentum, that is inversely proportional to the deflection angle. The *bending plane* is directed along the vertical axis, while the *non-bending plane* is along the horizontal axis.

2.2.2.3 Tracking stations

The task of the tracking stations is to reconstruct the muon tracks along the apparatus. There are five tracking stations, each one composed of two chambers: the first two stations are between the front absorber and the dipole magnet, the third one is inside the dipole magnet, the fourth and the fifth ones are located between the magnet and the muon filter.

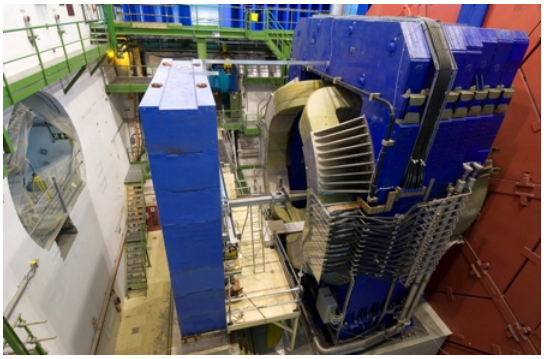

Figure 2.7: The dipole magnet.

The tracking chambers are Multi-Wire Proportional Chambers (MWPC), with the two cathode planes segmented in strips (or divided in pads); they make possible the calculation of the coordinates of the impact point of the muon on the chamber with the weighted average of the charge deposited on a certain strip/pad.
The spatial resolution of the tracking chambers is ~ 100 μm in the bending direction and 1 mm in the non-bending direction.
To keep the occupancy[1] at a 5% level, a very fine segmentation is needed: pads near the beam pipe in the first station are as small as 4.2×6 mm^2 (see fig. 2.8). The total number of read-out channels is about 1 million. The chambers in stations 1 and 2 have a quadrant geometry (see fig. 2.9, left side), with read-out electronics on the surface, while those in stations 3, 4 and 5 have a slat geometry (see fig. 2.9, right side) and read-out electronics on the side. In order to minimize the multiple scattering of the muons, the materials in the tracking system are composite ones, such as carbon fiber, so that the total thickness of a chamber is 0.03 X_0.
To be accepted by the tracking system, a muon track must fire at least one of the two chambers in the stations 1, 2 and 3, and give at least 3 signals in the stations 4 and 5. Fig. 2.10 shows one of the tracking chambers.
The front-end electronics for all stations is based on a 64 channels board (MAnas NUmérique, MANU) On this board the signals of four 16-channels charge amplifier chips (Multiplexed ANAlogic Signal processor, MANAS) are sent to 12-bits ADCs and to a readout chip (Muon Arm Readout Chip, MARC) whose functionalities include

[1]The occupancy is defined as the ratio between the number of pads/strips hit and the total number of pads/strips present in a given detector area.

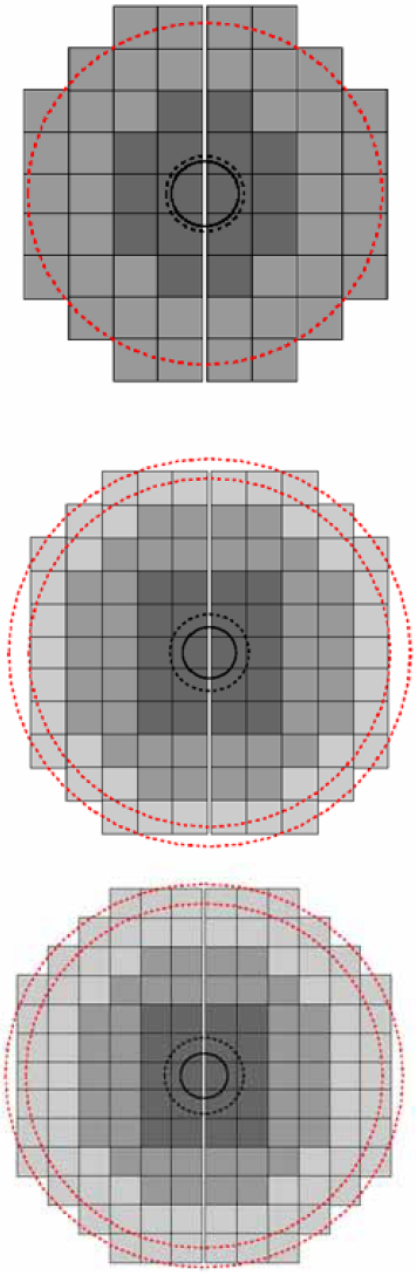

Figure 2.8: Schematic view of a chamber in stations 3, 4 and 5 respectively, with the different strip densities.

the zero suppression. The Concentrator ReadOut Cluster (CROCUS) dispatches the trigger signal from the central trigger processor (CTP) to each half plane, it performs

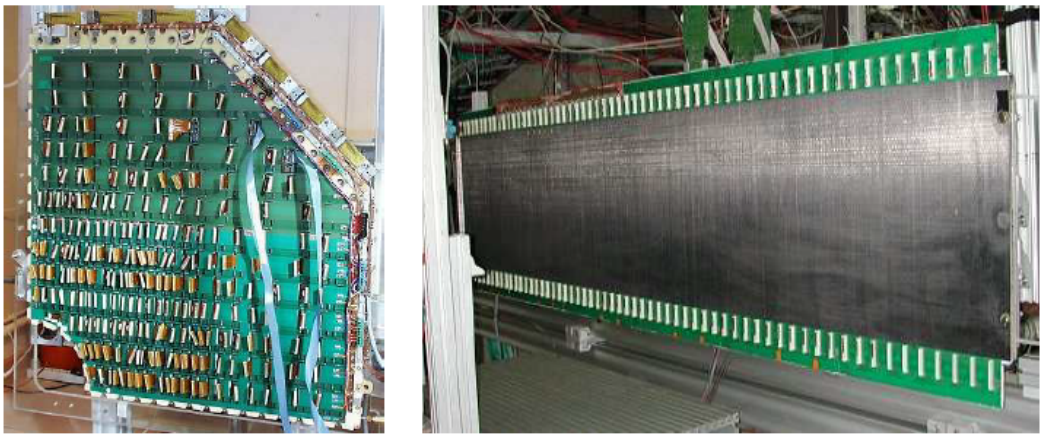

Figure 2.9: Left side: quadrant geometry of tracking chambers in stations 1 and 3; left side: slat geometry of tracking chambers in stations 3, 4 and 5.

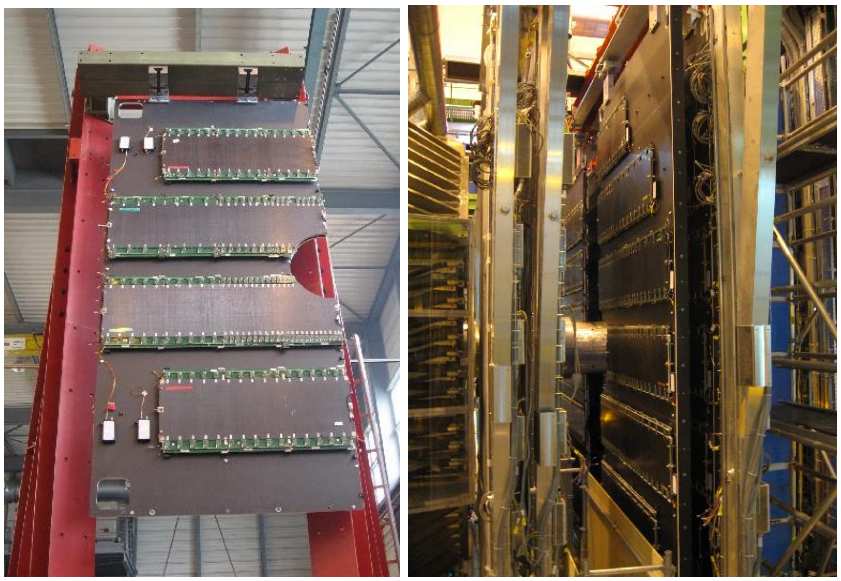

Figure 2.10: One of the tracking stations.

the calibration of the MANU, and gathers data through specific buses (Protocol for the ALICE Tracking CHamber, PATCH) sending them to the DAQ within 240 μs after the trigger signal.

2.2.2.4 Trigger stations

The trigger task is to select the events of interest (i.e., the muon pairs produced by the decay of the resonances) with respect to the particles from the background, most of which are low-momentum muons coming from the decay of pions and kaons. In order to do this, the trigger applies a cut on the transverse momentum, asking for it to be greater than a certain value.

There are two trigger stations (MT1 and MT2), each one of them made up of two chambers, 1 m far from each other, located behind the muon filter, at 16.1 m from the interaction point (see fig. 2.11).

Each station is constituted by two planes of 18 Resistive Plate Chambers (RPC), made up of high resistivity bakelite electrodes separated by 2 mm wide gas gap and with a time resolution of $\sim$ 2 ns. The planes are segmented in strips and provide the coordinates of the muon: the horizontal strips (aligned with the x axis in the ALICE reference system) measure the bending deviation due to the dipole magnetic field, while the vertical strips (aligned with the y axis) measure the non-bending direction.

The system is totally composed of 234 detection areas, each one of them associated with a local trigger board. The local board density reflects the strip segmentation. The strips width is 1, 2 or 4 cm in the bending plane, going from the center of the chamber outwards, and it is 2 or 4 cm in the non-bending plane.

The signals are discriminated and sent to the read-out electronics to be processed. The muon trigger is fired when at least three of the four RPC planes give a signal compatible to a tracklet in the muon trigger system.

The trigger threshold can be varied according to the collision system.

The trigger information is also used to identify the tracks in the offline analysis, since muons are not absorbed by the iron wall, differently from the residual hadrons.

The decision time of the trigger is about 300 ns.

2.2.3 The Forward Detectors

Many processes typical of the Quark-Gluon Plasma, like charmonia and bottomonia production, are function of the energy density and are evaluated through the centrality of the collisions.

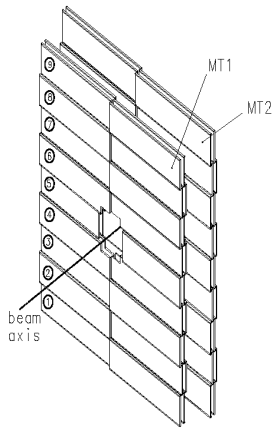

Figure 2.11: The trigger stations.

The **Forward Multiplicity Detector (FMD)** is a silicon strip detector divided in seven disks perpendicular to the beam pipe and placed at distances between 42 and 225 cm from the interaction point. It provides a charged particle multiplicity information complementary to the SPD, covering the pseudorapidity ranges -3.4 $< \eta <$ -1.7 and 1.7 $< \eta <$ 5.1.

The **Photon Multiplicity Detector (PMD)** determines the plane of the reaction and the anisotropy of the azimutal angle; it is a preshower detector that measures the multiplicity and spatial distribution of photons in the forward pseudorapidity region 2.3 $< \eta <$ 3.7 and provides an estimation of the transverse electromagnetic energy and of the reaction plane on an event-by-event basis.

It is located at 5.8 m from the interaction point and covers a pseudorapidity region 1.8 $\leq \eta \leq$ 2.6. The PMD consists of two identical planes of detectors, each one composed of 3×3 modules containing 24×24 gas proportional counters with honeycomb structure (Honeycomb Proportional Chambers) and wire readout, with a $3X_0$ thick lead converter in between.

The **TZERO** is made of two arrays of Cherenkov counters, with a time resolution lower than 50 ps, asymmetrically placed at 72.7 cm (muon spectrometer side) and 375 cm (PMD side) from the interaction vertex, covering the pseudorapidity ranges -3.28 $< \eta <$ -2.97 and 4.61 $< \eta <$ 4.92. It is designed to provide a T0 signal for the TOF detector, to measure the particle multiplicity and the vertex position with a precision

of ±1.5 cm.

The **VZERO** consists of two arrays of scintillator material, located 90 cm (Muon Spectrometer side) and 340 cm (PMD side) from the interaction point. The detectors are segmented into 72 elementary counters distributed in 5 rings, covering the pseudorapidity ranges -3.8 < η < -1.7 and 2.8 < η < 5.1. The measurement of the time-of-flight difference between the two parts of the detector allows to identify and reject the beam-gas events, providing a minimum bias trigger for the central barrel detectors and a validation signal for the muon trigger. Moreover, the VZERO measures the charged particle multiplicity, indicating the centrality in Pb-Pb collisions.

The **Zero Degree Calorimeters (ZDC)** are two pairs of calorimeters located in opposite positions at about 115 m from the interaction point. Each one of them consists of a proton detector and a neutron one, composed of quartz fiber calorimeters based on the Cherenkov effect, built-in inside a high density material (brass in the case of the proton detector and a tungsten alloy in the case of the neutron one), oriented at zero degrees with respect to the beam axis. The Cherenkov light produced in the optical fibers is guided to the photomultipliers.

The ZDC are dedicated to the study of the centrality of the collision through the measurement of the energy of the nucleons not directly involved in the reaction.

The number of the *spectating nucleons* decreases as the centrality of the collision increases; an estimate of the number of *participating nucleons* is given by the relation:

$$N_p = A - \frac{E_{ZDC}}{E_A}$$

where A is the ion mass number, E_{ZDC} is the energy measured in the ZDC and E_A is the energy of the beam per nucleon.

2.2.4 ALICE trigger and data acquisition

The trigger signals from the detectors are collected and processed by the ALICE Central Trigger Processor (CTP). The CTP is designed to select events with a variety of different features and rates, and to scale down these rates in order to fit the bandwidth requirements of the acquisition system.

The first trigger signal, called Level-0 (L0), at 1.2 μs after the collision, are sent by the fastest detectors (SPD, VZERO, TZERO) and by the muon trigger system. These signals are combined in the CTP with AND and OR logic, to select a certain class of

events. The information provided by the slower detectors is used to create a Level-1 trigger signal (L1), that is dispatched after 6.5 μs. The ALICE trigger system has a past-future protection circuit that searches for other events of the requested type, in certain time windows before and after the collision under investigation: this helps the rejection of pile-up events and the read-out of the detectors. The Level-2 (L2) trigger waits for this past-future protection and arrives after 88 μs.

The ALICE Data AcQuisition system (DAQ) has been designed taking into account the fact that pp collisions occur at high rates and have relatively small event sizes, while on the other hand Pb-Pb collisions are characterized by lower rates and larger amount of data, up to 1.25 GB/s sent to the storage elements.

Once the CTP decides to acquire a specific event, the trigger signal is sent to the Front-End Read-Out electronics (FERO) of the involved detectors. Data are thus dispatched to farms of computers (Local Data Concentrators), which build the event fragments coming from the front-end electronics into sub-events. The sub-events are then sent to the Global Data Collectors (GDC), that take all the sub-events from the various LDC, build the whole event and, eventually, send it to the storage facilities.

3

Monte Carlo simulation of the dimuon sources

Contents

Monte Carlo generators are used in high energy physics for various tasks, such as the estimation of the frequency or the topology of the events, the simulation of the background, the development of methods for data analysis.
The presence of the apparatus introduces distortions in the measurement: in this case, a simulation of the apparatus (performed with the use of the transport code GEANT3), together with a Monte Carlo generation of the sources, is needed in order to calculate the acceptance correction.

3.1 Parametrization of the low mass resonances distributions

The main sources of the signal mass spectrum in the low mass region are the electromagnetic decays of the light resonances (already described in 1.2) and the semi-leptonic decays of Open Charm and Open Beauty:

$$\eta \to \mu^+\mu^-$$
$$\eta \to \mu^+\mu^-\gamma$$
$$\rho \to \mu^+\mu^-$$

$$\omega \rightarrow \mu^+\mu^-$$
$$\omega \rightarrow \mu^+\mu^-\pi^0$$
$$\eta' \rightarrow \mu^+\mu^-\gamma$$
$$\phi \rightarrow \mu^+\mu^-$$
$$D \rightarrow \mu\nu_\mu$$
$$B \rightarrow \mu\nu_\mu$$

The continuum due to the semi-leptonic decays of open charm and beauty was simulated using a parametrization of PYTHIA, AliGenCorrHF [63].
The light resonances were simulated using the hadronic cocktail generator (AliGenMUONLMR), that was at first developed for the analysis in pp collisions at 7 TeV [3][64] and derives from the old GENESIS generator developed for CERES.
The kinematic distributions depending on energy that were parametrized are:

- transverse momentum;
- rapidity;
- multiplicity.

The distributions independent on energy being parametrized are instead:

- mass line shape;
- form factors of Dalitz decays;
- polar angle.

3.1.1 Parametrization of p_T, rapidity and multiplicity distributions

In the 7 TeV pp analysis, the input rapidity and multiplicity distributions for all particles were based on a parametrization of PYTHIA 6.4 [65] with the Perugia-0 tune [66] at 7 TeV; similarly, in the case of pp and Pb-Pb collisions at 2.76 TeV, the rapidity and multiplicity distributions for each process have been parametrized on the basis of PYTHIA events at that energy.
In fig. 3.1 the rapidity distributions obtained at 2.76 TeV for η, η', ρ, ω and ϕ mesons are shown.
The multiplicity distributions of the light resonances at 2.76 TeV are shown in fig. 3.2.

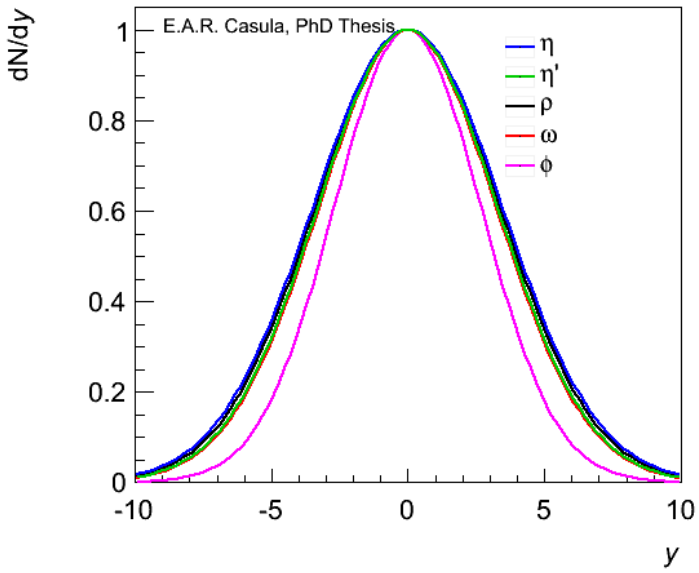

Figure 3.1: Rapidity distributions of light resonances obtained with a PYTHIA Perugia-0 parametrization at 2.76 TeV.

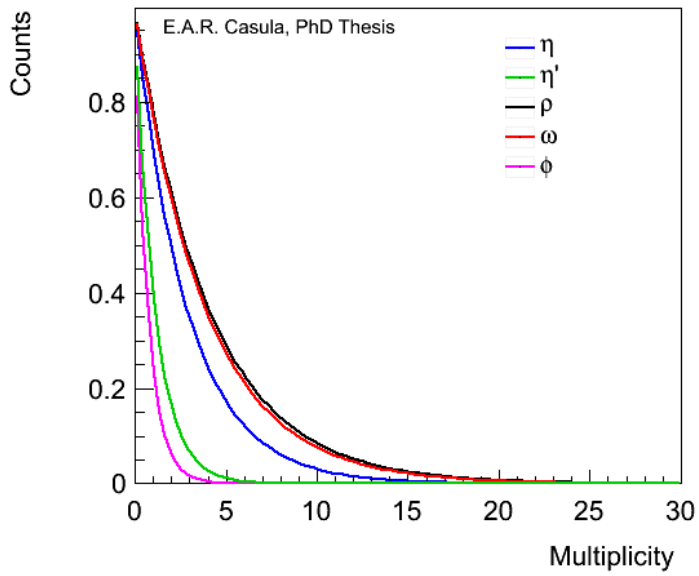

Figure 3.2: Multiplicity distributions of the light resonances at 2.76 TeV.

In the 7 TeV analysis the transverse momentum distribution was based on the same PYTHIA parametrization at that energy in the case of η', while for the η meson it was

based on the preliminary results from η production yields measured in the two-photon decay channel by ALICE [67].

The transverse momentum distribution for ρ, ω and ϕ was instead described with a power law function, used also by HERA-B experiment to fit the ϕ p_T^2 spectrum [68]:

$$\frac{dN}{dp_T} = C\frac{p_T}{[(1+p_T/p_0)^2]^n} \tag{3.1}$$

where the parameters n and p_0 were tuned iteratively to the results of the analysis in pp at 7 TeV itself.

At 2.76 TeV also the η and η' p_T distributions have been described with the power law function, parametrized on the basis of the ALICE measurement at 7 TeV, while for ρ, ω and ϕ the average p_T value has been scaled as the value at 7 TeV based on PYTHIA, according to the formula:

$$\langle p_t \rangle^{ALICE}_{2.76\ TeV} = \langle p_t \rangle^{ALICE}_{7\ TeV} \cdot \frac{\langle p_t \rangle^{PYTHIA}_{2.76\ TeV}}{\langle p_t \rangle^{PYTHIA}_{7\ TeV}} \tag{3.2}$$

where $\langle p_t \rangle^{ALICE}_{7\ TeV}$ was obtained from the low mass region analysis at 7 TeV.

Fig. 3.3 shows the p_T distributions of the light resonances at 2.76 TeV.

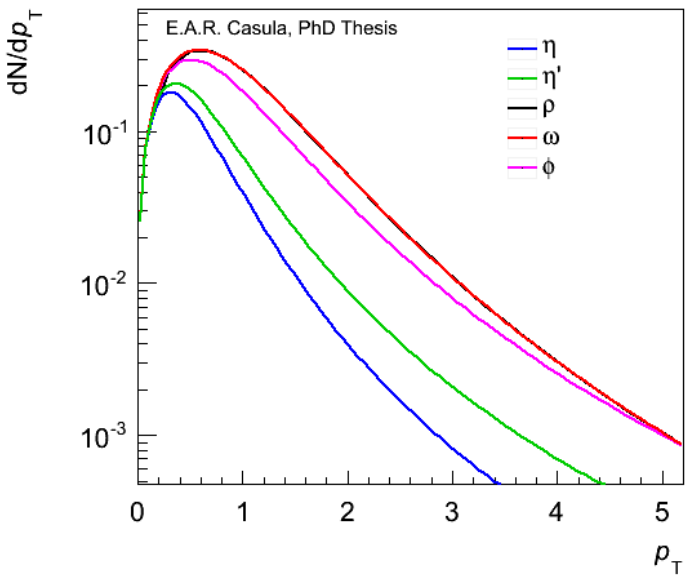

Figure 3.3: p_T distributions of the light resonances at 2.76 TeV.

The comparison between the p_T distribution of ϕ and ω mesons at 2.76 and 7 TeV is shown in fig.3.4.

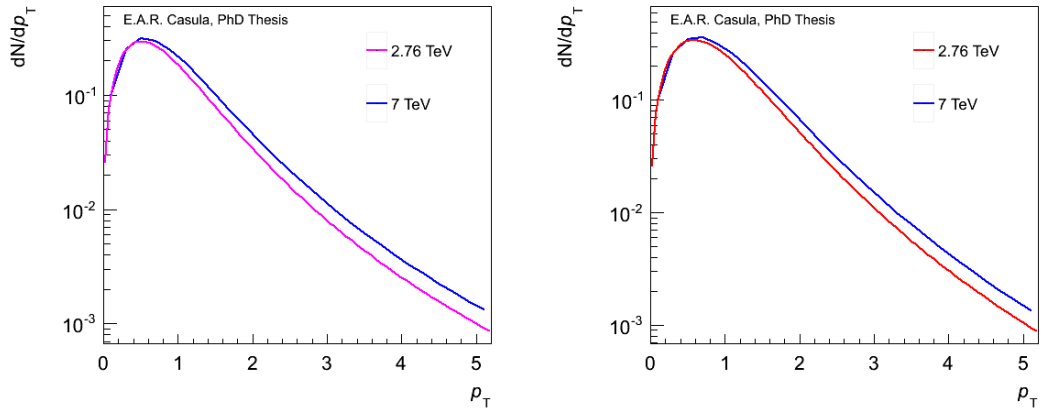

Figure 3.4: Comparison of ϕ (left) and ω (right) p_T distributions at 2.76 and 7 TeV.

3.1.2 Parametrization of line shape, form factors and polar angle distributions

The linewidths of η, η', ω and ϕ ($\Gamma_\eta = 1.31 \pm 0.05$ keV, $\Gamma_{\eta'} = 0.198 \pm 0.009$ MeV, $\Gamma_\omega = 8.49 \pm 0.08$ MeV, $\Gamma_\phi = 4.26 \pm 0.04$ MeV) are negligible with respect to the ALICE apparatus resolution (55 MeV): for this reason, their line shape has been generated as a Dirac δ function. The linewidth of ρ meson ($\Gamma_\rho = 149.1 \pm 0.8$) is larger than the apparatus resolution, so the ρ line shape has been parametrized on the basis of NA60 measurements [69]:

$$\frac{dR_{\rho\to\mu^+\mu^-}}{dM} = \frac{\alpha^2 m_\rho^4}{3(2\pi)^4} \frac{\left(1-\frac{4m_\pi^2}{M^2}\right)^{3/2}\left(1-\frac{4m_\mu^2}{M^2}\right)^{1/2}\left(1+\frac{2m_\mu^2}{M^2}\right)}{(M^2-m_\rho^2)^2+M^2\Gamma^2}(2\pi MT)^{3/2}e^{-M/T} \quad (3.3)$$

where T = 170 MeV.

The ρ line shape is shown in fig. 3.5.

The form factors of the Dalitz decays have been parametrized with the pole approximation [70], on the basis of the NA60 measurement as well:

$$F(q^2) \equiv F(M^2) = \left(1-\frac{M^2}{\Lambda^2}\right)^{-1} \quad (3.4)$$

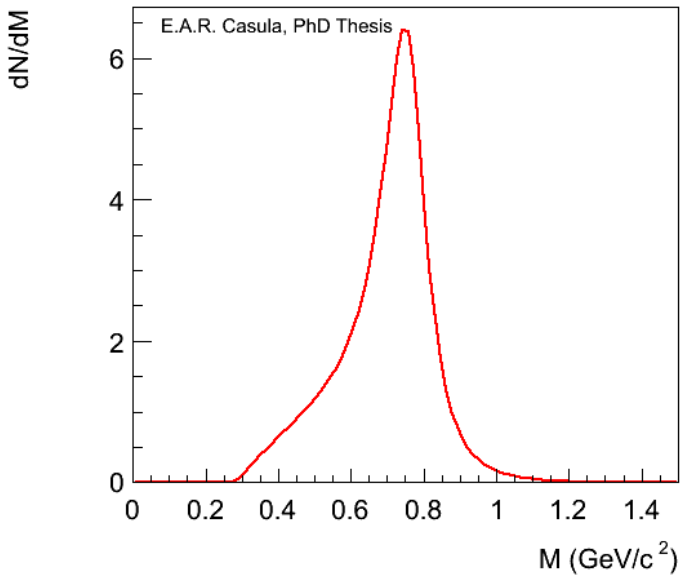

Figure 3.5: ρ meson line shape

The ϑ polar angle distributions of the decay products of the light resonances have been assumed to be flat between 0 and π in the case of the 2-body decays. In the case of the Dalitz decays, similarly to what has been done at CERES and NA60 experiments, a polarized distribution has been assumed:

$$W(\vartheta) \propto 1 + cos^2\vartheta$$

4

Low mass dimuon analysis in pp collisions at $\sqrt{s} = 2.76$ TeV

Contents

The pp analysis at 2.76 TeV is necessary to provide a baseline for the Pb-Pb analysis at the same energy. LHC has run twice in pp collisions at $\sqrt{s} = 2.76$ TeV: the first run in 2011 (already presented in [64]), and the second run in 2013, with a statistics about 4 times greater with respect to 2011.

4.1 Data sample and applied selections

The data collected in 2013 are the ones corresponding to LHC13g period (see 6.8), with an integrated luminosity of 81.094 ± 0.015 nb^{-1}.

Data were collected with a dimuon trigger, that consists in the coincidence of two single-muon all-p_T trigger signals, with the all-p_T trigger threshold set at $p_T \sim 0.5$ GeV/c.

The selections applied to the data were:

- *Physics Selection* to remove beam-gas background: this is done before any analysis, by computing the timing of a signal that passes the triggers, to ensure that the event had occurred at the ALICE interaction point;
- $2.5 < \eta_\mu < 4$ (to cut the tracks at the borders of the detector acceptance);
- both muon tracks reconstructed in the muon tracking chambers have to match a tracklet reconstructed in the muon trigger;
- $2.5 < y_{\mu\mu} < 4$.

The number of opposite sign dimuon triggers in our sample satisfying these requirements amounts to $N_{OS} \sim 5.02 \cdot 10^6$.

4.1.1 Estimation of the integrated luminosity

The integrated luminosity $L_{int} = 81.094 \pm 0.015$ nb^{-1}has been calculated run by run as $L_{int} = \Sigma_{run} N_{OS}^{run} / (f_{norm}^{run} \cdot \sigma_{MB})$.
Here $\sigma_{MB} = 55.4 \pm 1.0$ mb is the minimum bias cross section, estimated in 2011 through a Van Der Meer scan [71]; N_{OS}^{run} is the number of opposite-sign dimuon triggers per run and f_{norm}^{run} is the normalization factor that allows to rescale the number of opposite-sign dimuon triggers to the number of minimum bias triggers through the relation $N_{MB} = f_{norm} * N_{OS}$. f_{norm} is defined as $f_{norm} = \frac{N_{MB}^{trig}}{N_{OS\&MB}^{trig}}$, where N_{MB}^{trig} is the number of events flagged with the minimum bias trigger and $N_{OS\&MB}^{trig}$ is the number of events triggered by both minimum bias and dimuon triggers.

4.2 Background subtraction

The opposite sign mass spectrum of the muon pairs satisfying the above mentioned selections is shown in fig. 4.1.
Here the background is mostly due to uncorrelated muon pairs coming from the decay of pions and kaons.
The background has been subtracted with the use of the *event mixing* technique, where two muons coming from two different, independent events are randomly paired, so to build an invariant mass spectrum that consists of muon pairs uncorrelated by construction.

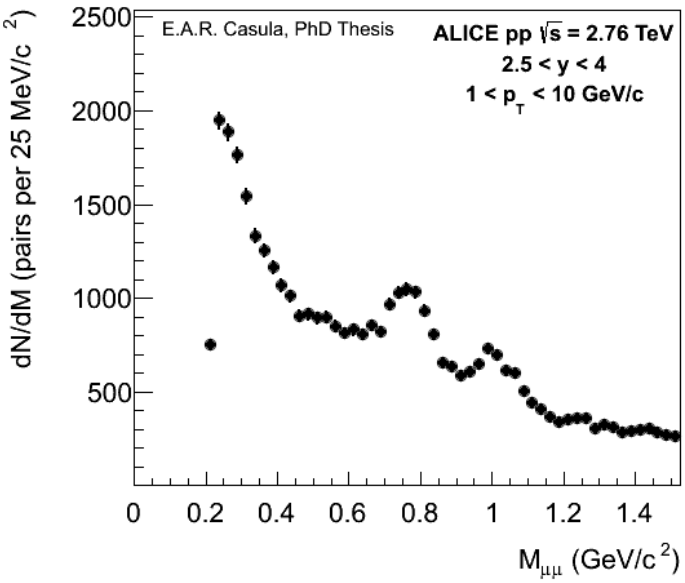

Figure 4.1: Opposite sign dimuon mass spectrum in pp collisions at 2.76 TeV.

The distribution obtained from the event mixing has been normalized to $2R\sqrt{N^{real}_{\mu^+\mu^+}N^{real}_{\mu^-\mu^-}}$, where $N^{real}_{\mu^+\mu^+}$ and $N^{mixed}_{\mu^+\mu^+}$ are the oppisite-sign pairs of muons from data and from event mixing respectively.

The R factor is defined as $A_{\mu^+\mu^-}/\sqrt{A_{\mu^+\mu^+}A_{\mu^-\mu^-}}$, where $A_{\mu^+\mu^+}$ ($A_{\mu^-\mu^-}$) is the acceptance for a ++ (- -) pairs and takes into account the possible correlations introduced by the detector. It was estimated as $R = N^{mixed}_{\mu^+\mu^-}/2\sqrt{N^{mixed}_{\mu^+\mu^+}N^{mixed}_{\mu^-\mu^-}}$, where $N^{mixed}_{\mu^+\mu^+}$ ($N^{mixed}_{\mu^-\mu^-}$) is the number of mixed pairs for a given charge combination.

In fig. 4.2 the opposite sign dimuon mass spectrum together with the background evaluated through the event mixing are shown.

The signal/background ratio (see fig. 4.3) is about 2 at the ϕ peak.

To estimate the quality of the background subtraction, we can look at the ratio between the invariant mass spectra of the like-sign real and mixed pairs (see fig. 4.4). This ratio is reasonably flat, meaning that the event mixing reproduces with enough accuracy the mass spectrum of the real like-sign pairs. The difference in the ratio by 2.2% from unity has been taken as an estimate of the systematic uncertainty on the background normalization.

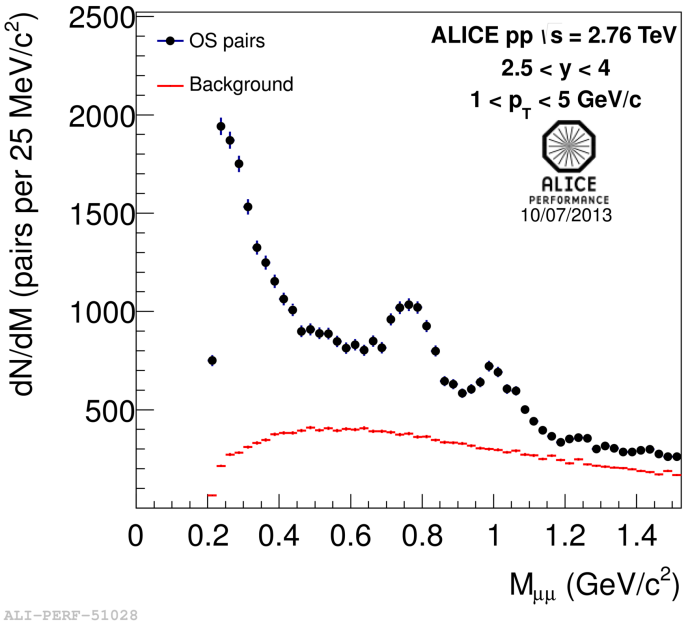

Figure 4.2: Opposite sign dimuon mass spectrum and background evaluated through the event mixing in pp collisions at $\sqrt{s} = 2.76$ TeV.

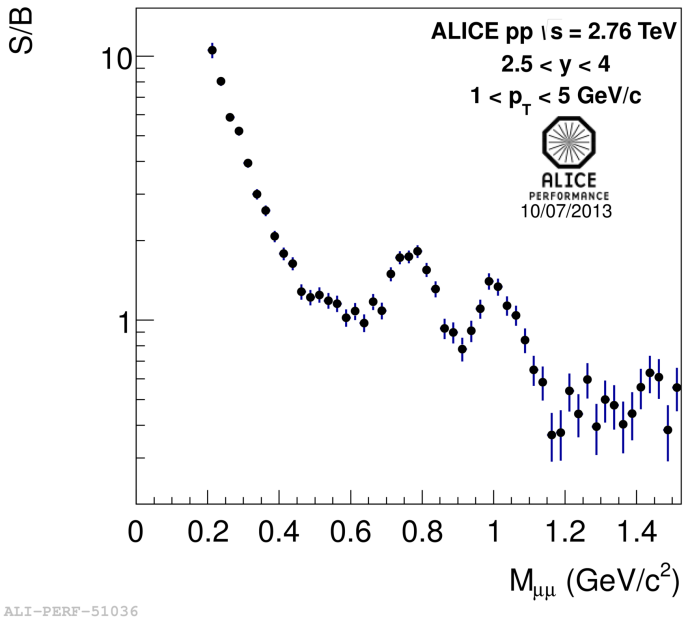

Figure 4.3: Signal/background ratio in pp collisions at $\sqrt{s} = 2.76$ TeV.

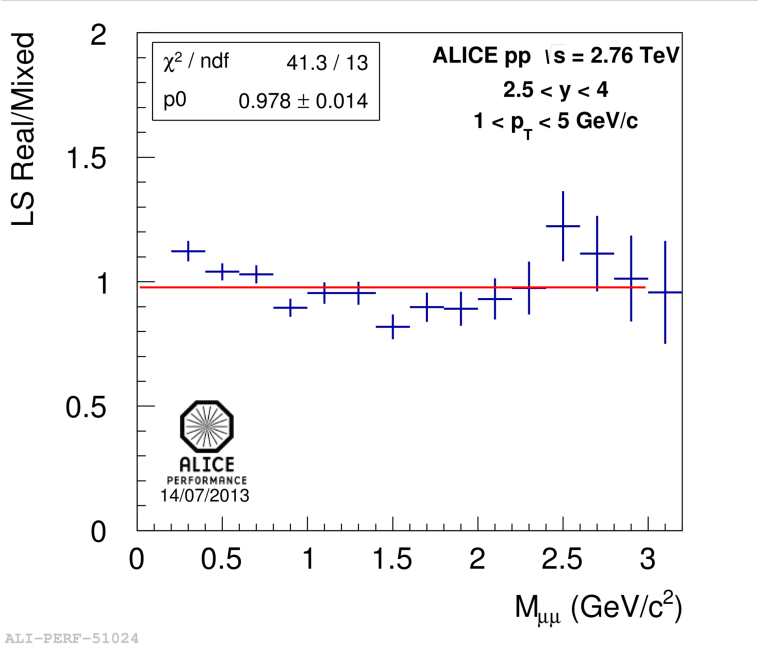

Figure 4.4: Ratio between the like-sign real and mixed pairs mass spectra in pp collisions at $\sqrt{s} = 2.76$ TeV.

4.3 Acceptance × efficiency correction

The acceptance × efficiency (A×ε) correction is needed because of the distortions introduced in the measurement by the presence of the apparatus.

To estimate A×ε, a Monte Carlo simulation of the dimuon sources in the low mass region, together with the simulation of the apparatus, is mandatory.

The Monte Carlo generation was done using the parametric generator already described in cap. 3; the simulation of the ALICE apparatus was performed with the transport code GEANT 3.

A×ε as a function of p_T is calculated as the ratio between the reconstructed and generated dimuon p_T distributions in certain p_T intervals in the same rapidity window. The selections applied to the reconstructed dimuons are the same as the ones applied to the data.

For ϕ meson, A×$\varepsilon = 11.78\%$ for $1 < p_T < 5$ GeV/c and $2.5 < y < 4$.

4.4 Signal extraction

The fit to the mass spectrum is show in fig. 4.5, for $1 < p_T < 5$ GeV/c. The invariant mass spectrum has been fitted with the contributions given by the decays into muons of the light resonances and of Open Charm and Open Beauty (see also chapter 3).
The free parameters of the fit are the normalizations of the following processes:

- $\eta \to \mu^+\mu^-\gamma$
- $\omega \to \mu^+\mu^-$
- $\phi \to \mu^+\mu^-$
- Open Charm

The other processes were fixed according to the relative branching ratios or cross sections: $\eta \to \mu^+\mu^-$ and $\eta' \to \mu^+\mu^-\gamma$ are fixed to $\eta \to \mu^+\mu^-\gamma$, $\rho \to \mu^+\mu^-$ and $\omega \to \mu^+\mu^-\gamma$ are fixed to $\omega \to \mu^+\mu^-$, the Open Beauty normalization is fixed to the one of Open Charm.
The red band represents the uncertainty in the relative normalization of the sources and it is mainly due to the error on the branching ratios of the ω and η' Dalitz decays. The blue band represents instead the systematic error due to the background subtraction.
The raw numbers of ϕ and $\rho + \omega$ resonances extracted through the fit are $N_{\phi}^{raw} = 1410$ ± 102 and $N_{\rho+\omega}^{raw} = 3370$ ± 145, for dimuon p_T between 1 and 5 GeV/c: this value is about one half of the statistics collected in pp analysis at 7 TeV [3] and about 4 times the statistics collected in the previous pp run at 2.76 TeV [64].
A small excess of about 7% is observed in the region $0.4 < M < 0.7$ GeV/c^2. The statistics of our data sample does not allow a reliable study of the nature of this excess as a function of p_T and rapidity, that will be instead carried out in the p-Pb analysis. The fact that the hadronic cocktail does not reproduce well all the expected sources will be in any case taken into account in the evaluation of the systematic uncertainty.
In order to measure the ϕ differential cross section, the raw number of ϕ has been extracted in seven p_T bins between 1 and 5 GeV/c: the dimuon invariant mass spectrum after combinatorial background subtraction in these p_T bins is shown in figure 4.6.

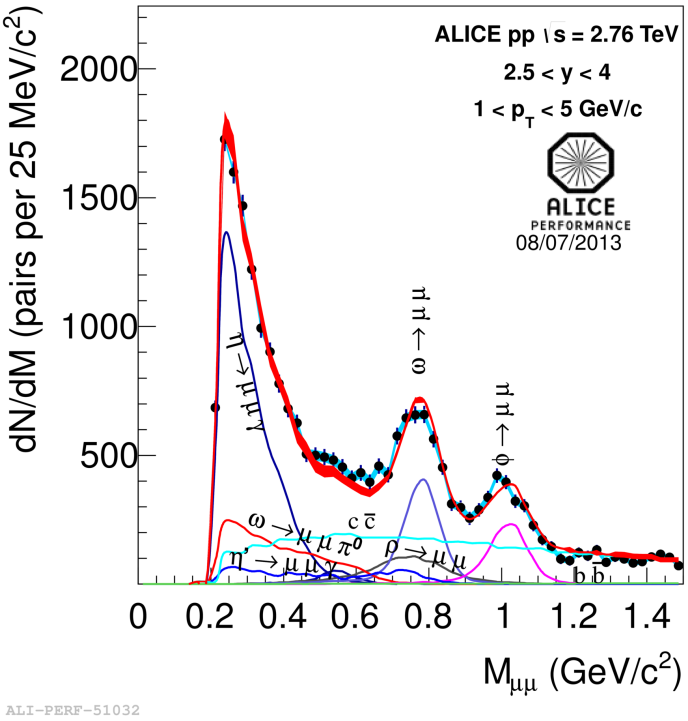

Figure 4.5: Dimuon invariant mass spectrum in pp at $\sqrt{s} = 2.76$ TeV after combinatorial background subtraction for $1 < p_T < 5$ GeV/c (full circles). Light blue band: systematic uncertainty from background subtraction. Red band: sum of all simulated contributions. The width of the red band represents the uncertainty on the relative normalization of the sources.

4.4.1 Systematic uncertainties on the signal extraction

To determine the systematic uncertainties on the raw number of ϕ and $\rho+\omega$, the fit with the hadronic cocktail has been replaced with a fit with two empirical functions, due to the fact that the hadronic cocktail does not reproduce well all the expected sources in the mass spectrum. In both functions, the resonance peaks have been described by Crystal Ball functions[1], fixing the ratio between ρ and ω such that $\sigma_\rho/\sigma_\omega = 1$. In the

[1]The Crystal Ball function consists of a Gaussian core portion and a power-law tail at low mass defined by the parameters a and n. The power-law part reproduces non-Gaussian fluctuations due to energy loss processes:

$$f(x, \bar{x}, \sigma, \alpha, n) = N \cdot \begin{cases} e^{-\frac{(x-\bar{x})^2}{2\sigma^2}} & \text{for } \frac{(x-\bar{x})^2}{\sigma} > -\alpha \\ A \cdot \left(B - \frac{x-\bar{x}}{\sigma}\right)^{-n} & \text{for } \frac{(x-\bar{x})^2}{\sigma} \leq -\alpha \end{cases}$$

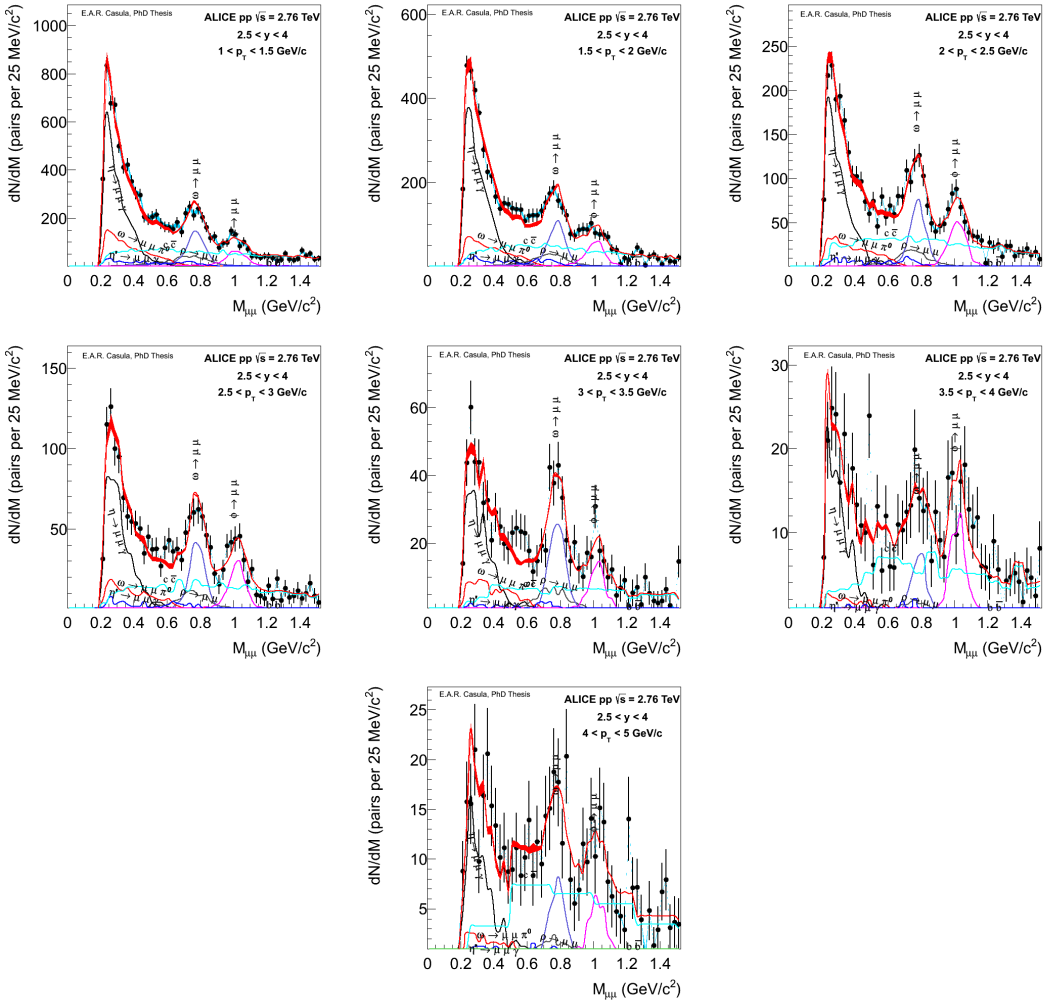

Figure 4.6: Dimuon invariant mass spectrum in pp at $\sqrt{s} = 2.76$ TeV after combinatorial background subtraction in several p_T bins between 1 and 7 GeV/c.

case of the first function (f_1), the continuum has been parametrized as the superposition of an exponential (that dominates the region $2m_\mu < M < 0.4$ GeV/c^2) and a straight line.

In the case of the second function (f_2), the continuum has been parametrized as a variable width Gaussian, that is, a Gaussian whose width varies as a function of the mass values.

In figures 4.7 and 4.8 the fits with f_1 and f_2 for the different p_T bins are shown.

The systematic uncertainty has been estimated as half of the maximum difference on the raw number of ϕ calculated with the three fitting methods (hadronic cocktail, f_1, f_2), taking as reference value the one obtained with the hadronic cocktail.

The raw number of ϕ as a function of p_T, obtained with these fitting methods, is reported in fig. 4.9.

The raw number of ϕ obtained with the different fit functions and the corresponding systematic uncertainties and A$\times\varepsilon$ factors for the different p_T bins are reported in table 4.1.

Table 4.1: Raw number of ϕ and corresponding systematic uncertainty in different p_T bins, obtained with different fit functions

p_T	N_ϕ^{raw} (hadronic cocktail)	N_ϕ^{raw} (f_1)	N_ϕ^{raw} (f_2)	syst.	A$\times\varepsilon$
1-1.5 GeV/c	448 ± 70	445 ± 55	403 ± 54	5.06%	6.11%
1.5-2 GeV/c	401 ± 53	385 ± 45	365 ± 44	4.48%	12.35%
2-2.5 GeV/c	300 ± 38	357 ± 31	347 ± 30	9.55%	19.66%
2.5-3 GeV/c	167 ± 26	188 ± 23	182 ± 22	6.43%	27.74%
3-3.5 GeV/c	83 ± 19	87 ± 17	83 ± 15	2.14%	34.67%
3.5-4 GeV/c	59 ± 15	67 ± 13	64 ± 12	6.49%	38.91%
4-5 GeV/c	41 ± 16	49 ± 13	54 ± 15	15.60%	39.15%
1-5 GeV/c	1487 ± 100	1590 ± 85	1494 ± 88	7.9%	11.78%

4.5 ϕ differential cross section

The ϕ differential cross section has been extracted for p_T between 1 and 5 GeV/c, calculating for each p_T bin the quantity:

$$\frac{d\sigma_\phi}{dydp_T} = \frac{N_\phi^{\rm raw}(\Delta p_T)}{A \cdot \epsilon(\Delta p_T) BR_{\phi\to e^+e^-} L_{\rm INT}} \tag{4.1}$$

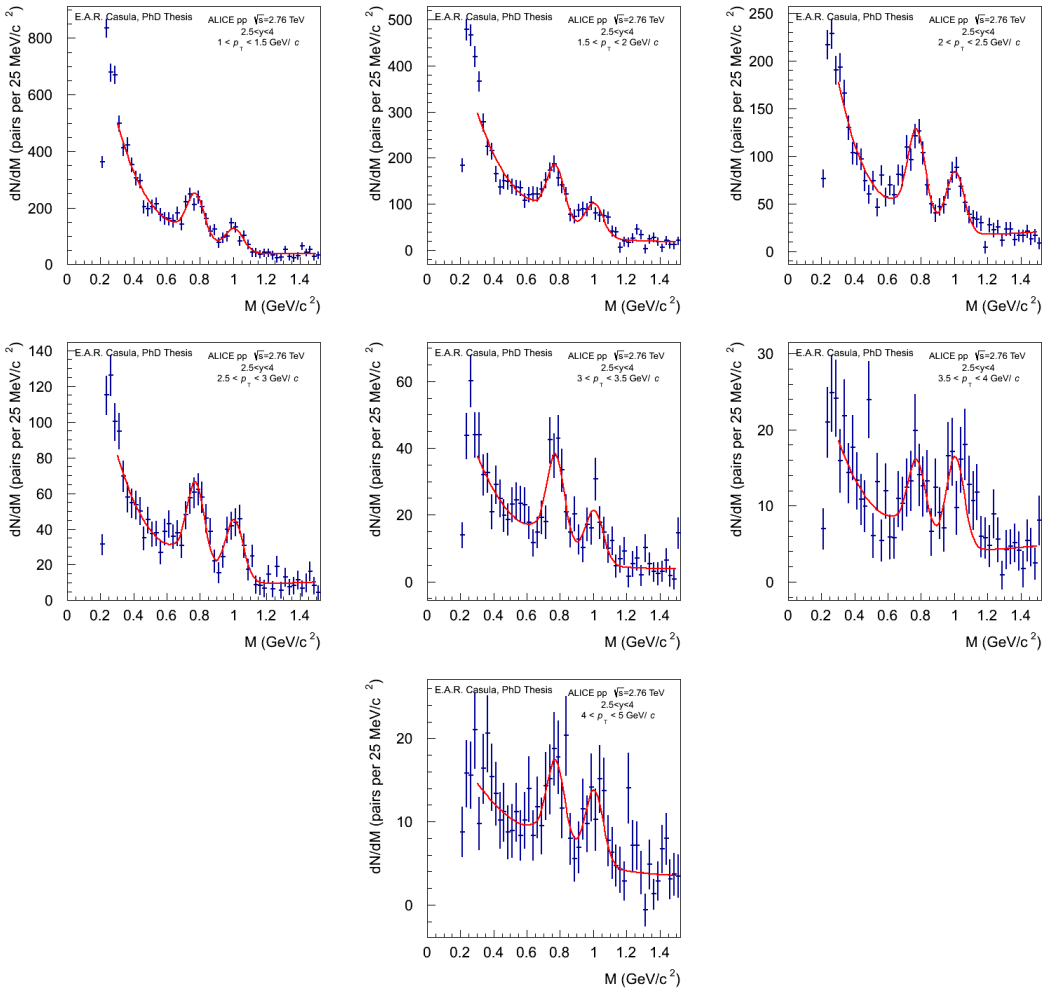

Figure 4.7: Dimuon invariant mass spectrum in pp at $\sqrt{s} = 2.76$ TeV after combinatorial background subtraction fitted with the function f_1 in the different p_T bins.

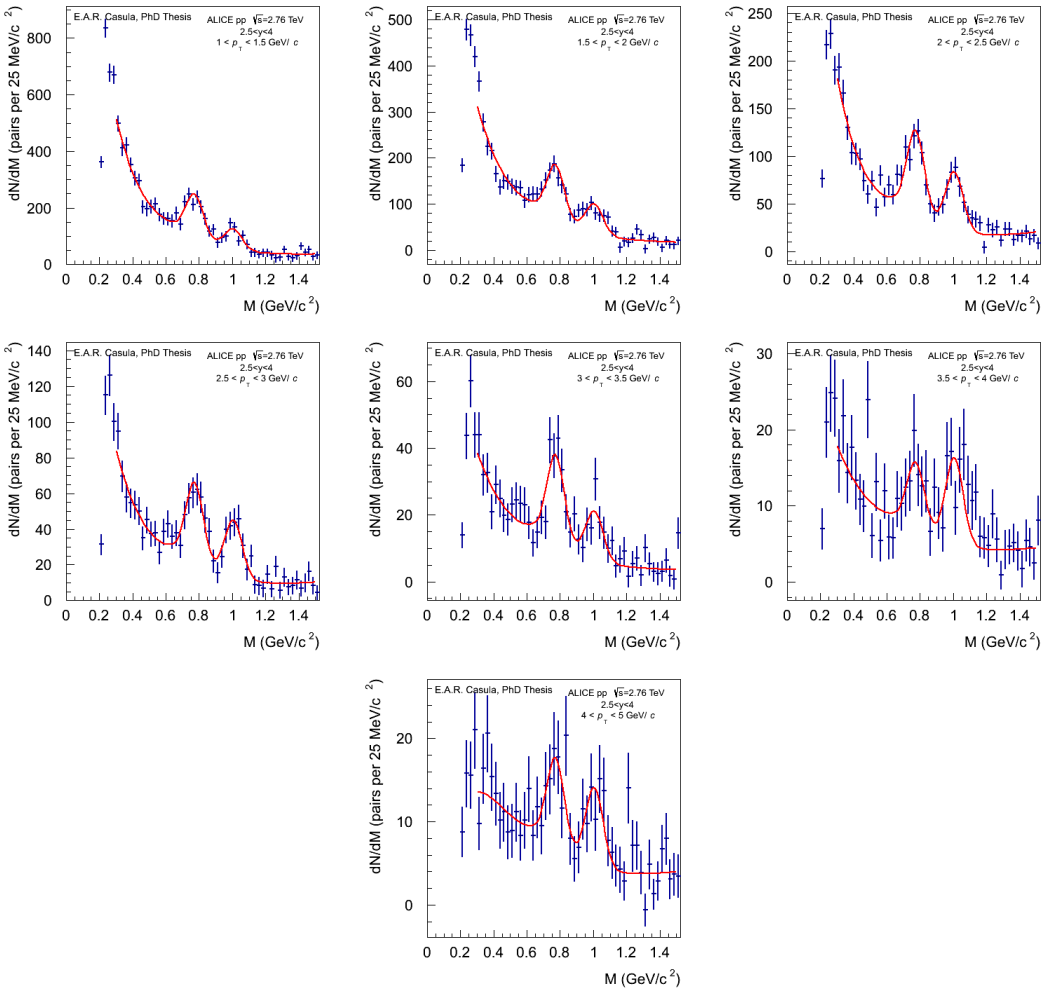

Figure 4.8: Dimuon invariant mass spectrum in pp at $\sqrt{s} = 2.76$ TeV after combinatorial background subtraction fitted with the function f_2 in the different p_T bins.

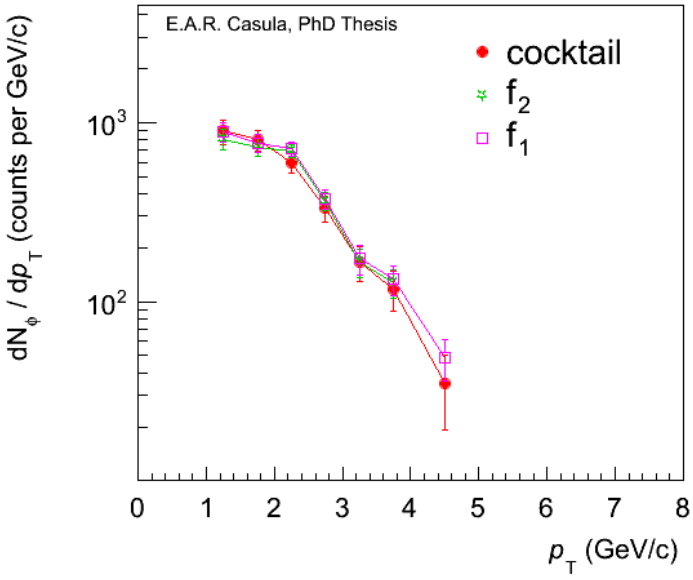

Figure 4.9: Raw number of ϕ vs p_T in pp at $\sqrt{s} = 2.76$ TeV obtained fitting the mass spectra with the hadronic cocktail (full circles), f_1 (open squares) and f_2 (open stars).

where $N_{\phi}^{\rm raw}(\Delta p_T)$ is the raw number of ϕ for a given p_T bin, $A \cdot \epsilon$ is the corresponding acceptance $\times$ efficiency, $BR_{\phi \to e^+e^-} = (2.954 \pm 0.030) \times 10^{-4}$ is the branching ratio for the ϕ decay into electrons, and $L_{\rm INT} = 81.094 \pm 0.015$ nb^{-1} is the integrated luminosity. The reason why the branching ratio for ϕ decay into electrons has been used instead of the one into muon pairs, is due to the fact that, according to the lepton universality, the coupling of the leptons to gauge bosons are flavour-independent, but the uncertainty of the measurement for the muon decay is about 6 times greater than the one in the electron channel ($BR_{\phi \to \mu^+\mu^-} = (2.87 \pm 0.19) \times 10^{-4}$).

The ϕ differential cross section as a function of p_T is shown on the left side of fig. 4.10, while on the right side the same measurement is compared with the previous one obtained with the data collected in 2011. Due to the low statistics collected in 2011, the corresponding measurement of ϕ differential cross section was extracted for $1 < p_T < 4$ GeV/c and not for $1 < p_T < 5$ GeV/c. The two measurements are in good agreement. Fig 4.11 shows the fit of the ϕ differential cross section with both a power-law $f_{pow} = \frac{A \cdot p_T}{[1+(p_T/p_0)^2]^n}$ and a Levy-Tsallis[1] function f_{Levy}. The two fits are indistinguishable. The

[1]The Levy-Tsallis function is defined as $f_{Levy} = p_T \frac{A(n-1)(n-2)}{nT[nT+M(n-2)]} \left[1 + \frac{m_T - M}{nT}\right]^{-n}$. Here M is the

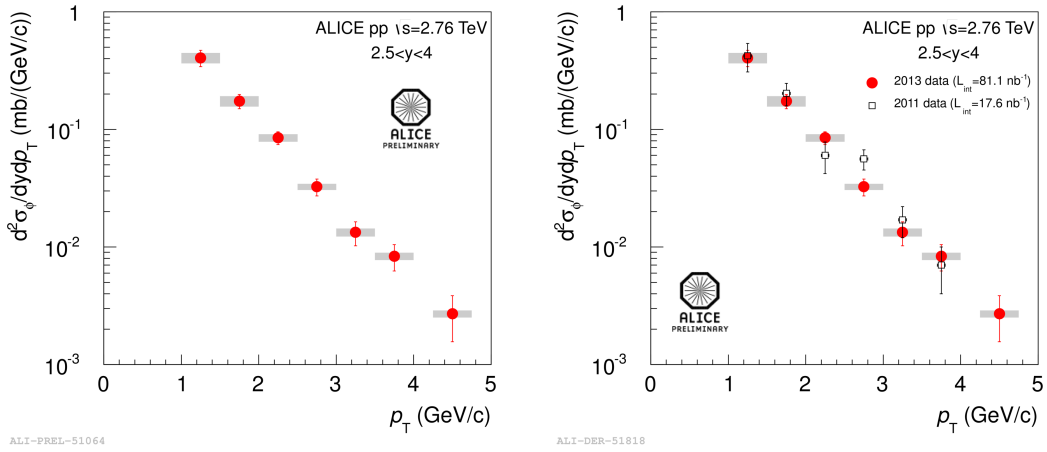

Figure 4.10: Left: ϕ differential cross section as a function of p_T in pp collisions at $\sqrt{s} = 2.76$ TeV. Right: comparison between the measurement in 2011 (open squares) and in 2013 (full circles).

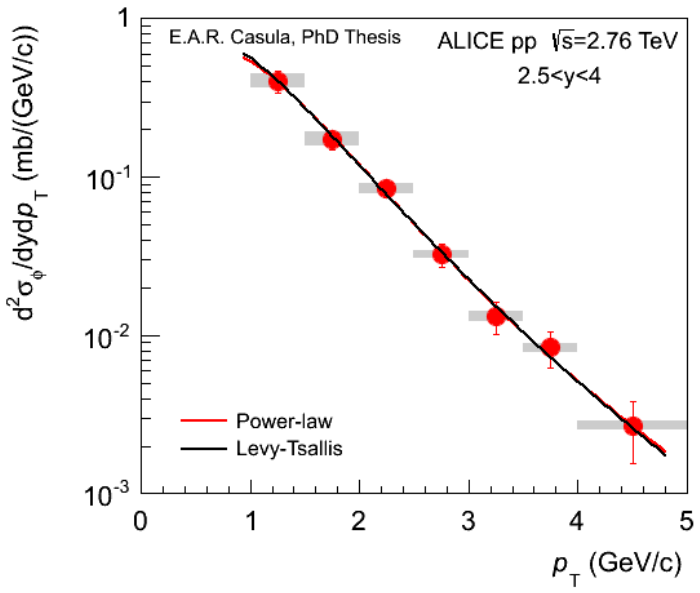

Figure 4.11: ϕ differential cross section as a function of p_T in pp collisions at $\sqrt{s} = 2.76$ TeV. fitted with power-law (red line) and Levy-Tsallis function (black line).

resulting fit parameters are:

$$\left.\begin{array}{l} A = 1.70 \pm 0.91 \\ p_0 = 1.68 \pm 0.45 \\ n = 3.78 \pm 0.72 \end{array}\right\} \text{for} f_{pow}$$

$$\left.\begin{array}{l} A = 2.16 \pm 1.03 \\ n = 10.2 \pm 4.81 \\ T = 0.284 \pm 0.072 \end{array}\right\} \text{for} f_{Levy}$$

Besides the differential cross section, the p_T integrated cross section has been calculated as well, for two different p_T intervals:

$$\sigma_\phi(1 < p_T < 5\text{GeV}/c) = 0.542 \pm 0.052(\text{stat}) \pm 0.043(\text{syst})\text{mb}$$

$$\sigma_\phi(2 < p_T < 5\text{GeV}/c) = 0.1082 \pm 0.0095(\text{stat}) \pm 0.0071(\text{syst})\text{mb}$$

The different contributions to the systematic uncertainty are discussed in the next section.

These values are the ones that will be used in the calculation of the nuclear modification factors in p-Pb and Pb-Pb collisions respectively.

4.5.1 Systematic uncertainty on ϕ differential cross section

In the calculation of the ϕ differential cross section, several sources of systematic uncertainty have been taken into account:

- uncertainty on the evaluation of the branching ratio $BR_{\phi\to e^+e^-}$ = (2.954 ± 0.030)×10^{-4} (1%);
- uncertainty on the integrated luminosity, coming from the uncertainty on σ_{MB} (1.8% - see 4.1.1);
- uncertainty on the raw number of ϕ determined by the fit, varying from about 2% to about 15% and already described in section 4.4.1);

ϕ meson mass, m_T is the transverse mass, A, n and T are the free parameters.

- uncertainty on the evaluation of the tracking efficiency. The value used is the one obtained in peripheral Pb-Pb collisions in 2011 (4.5% - see 6.4.1.5), since at present, the tracking efficiency has not been estimated for the pp data collected in 2013. This uncertainty was previously evaluated in pp collisions at 2.76 TeV in the 2011 data, and it amounted to 4%;

- uncertainty on the evaluation of the trigger efficiency. The systematic uncertainty arising from the intrinsic trigger efficiency was estimated by varying by 2% the efficiency of each local board in the simulation and amounts to 2%. This value was obtained by varying the cuts on the trigger tracks used to determine the intrinsic efficiency. This uncertainty is uncorrelated as a function of p_T and y. Another contribution comes from the uncertainty on the p_T trigger threshold. This contribution, amounting to 2%, has been evaluated in the Pb-Pb analysis (see 6.4.1.6), replacing the trigger response in the Monte Carlo with a function that fits the ratio between the p_T distributions of the muons that match two different trigger thresholds ($p_T \gtrsim 0.5$ GeV/c and $p_T \gtrsim 1$ GeV/c). The same approach could not be used in the pp analysis, since the data in this case were collected with the $p_T \gtrsim 0.5$ GeV/c threshold only. In order to be conservative, we decided to consider also this contribution on the systematic uncertainty. It has to be noticed that if a sharp p_T cut on the single muon is applied ($p_T > 0.5$ GeV/c and $p_T > 1$ GeV/c), the difference in the number of ϕ corrected for the A$\times\varepsilon$ is lower than the square root of the difference between the variances. This indicates that the A$\times\varepsilon$ correction does not introduce p_T dependent biases. The total value of the uncertainty related to the trigger efficiency amounts to 3%.

A possible additional source of systematic uncertainty is the contribution related to the background subtraction: in fact, due to the high signal/background ratio, the 2.2% uncertainty in the background normalization (see 4.2) translates into an uncertainty in the number of ϕ of only 0.5% for $1 < p_T < 1.5$ GeV/c, and lower values for higher p_T. This contribution was therefore neglected.

The values of ϕ differential cross section in the different p_T bins, together with the statistical and the systematic uncertainties, are summarized in table 4.2.

Table 4.2: Values of ϕ differential cross section as a function of p_T in pp collisions at $\sqrt{s} = 2.76$ TeV

p_T	$d^2\sigma/dydp_T$ (mb)	stat.	syst.
1-1.5 GeV/c	0.4045	0.064	4.1%
1.5-2 GeV/c	0.1739	0.024	1.8%
2-2.5 GeV/c	0.0848	0.011	0.6%
2.5-3 GeV/c	0.0325	0.005	0.2%
3-3.5 GeV/c	0.0133	0.003	0.1%
3.5-4 GeV/c	0.0083	0.002	0.1%
4-5 GeV/c	0.0027	0.001	0.1%
2-5 GeV/c	0.1082	0.010	0.7%
1-5 GeV/c	0.5420	0.052	4.3%

4.5.2 ϕ differential cross section: comparison with models

In fig. 4.12 the comparison of the ϕ differential cross section as a function of p_T with PHOJET[72][73] and several tunes of PYTHIA[65] (Perugia-0[66], Perugia-11[74], ATLAS-CSC[75] and D6T[76]): the PYTHIA tunes Perugia-0 and Perugia-11 strongly underestimate the measured cross section; PYTHIA ATLAS-CSC also underestimates the data (even if to a lesser degree than Perugia-0 and Perugia-11), while PYTHIA D6T slightly overestimates them. PHOJET is instead in good agreement with the measured values. The ratio between data and models is shown in fig. 4.13. Table 4.3 reports the measured integrated cross section, together with the integrated cross sections obtained with the models in the p_T intervals $1 < p_T < 5$ GeV/c and $2 < p_T < 5$GeV/c.

Table 4.3: ϕ cross section in pp at 2.76 TeV: measurement from ALICE compared with values from PHOJET and PYTHIA tunes Perugia-0, Perugia-11, D6T and ATLAS-CSC, for $1 < p_T < 5$GeV/c and for $2 < p_T < 5$GeV/c, in the rapidity interval $2.5 < y < 4$

	σ_ϕ [mb] ($1 < p_T < 5$ GeV/c)	σ_ϕ [mb] ($2 < p_T < 5$ GeV/c)
ALICE $\mu\mu$ measurement	0.542 ± 0.052 ± 0.043	0.108 ± 0.010 ± 0.007
PYTHIA Perugia-0	0.276	0.066
PYTHIA Perugia-11	0.297	0.063
PYTHIA D6T	0.634	0.119
PYTHIA ATLAS-CSC	0.469	0.075
PHOJET	0.494	0.108

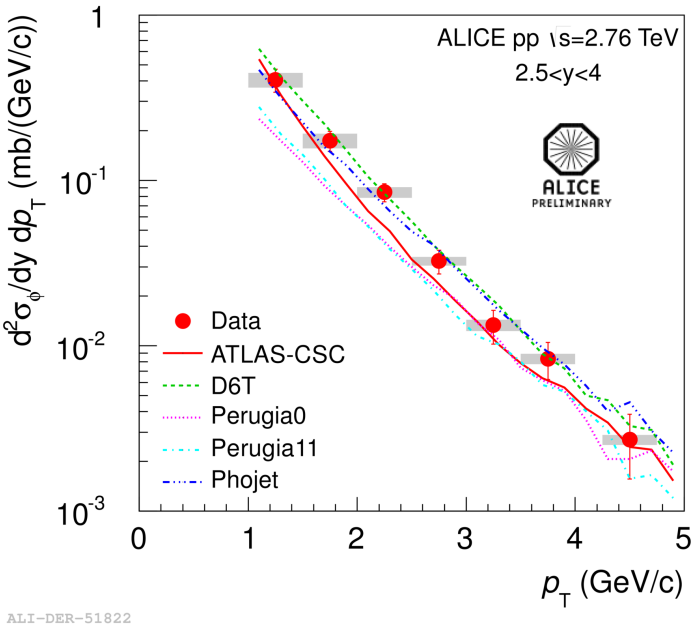

Figure 4.12: ϕ differential cross section as a function of p_T in pp collisions at $\sqrt{s}$ = 2.76 TeV compared with the predictions based on the PYTHIA tunes ATLAS-CSC, D6T, Perugia-0 and Perugia-11 and on PHOJET.

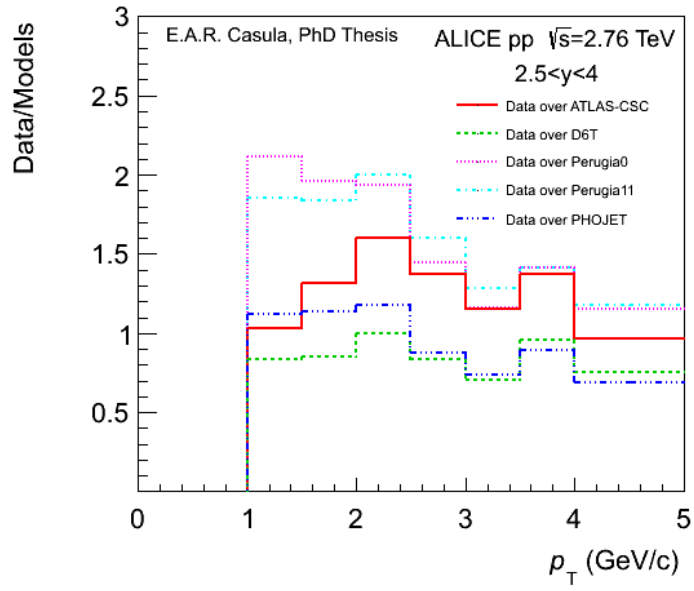

Figure 4.13: Ratio between data and models (PYTHIA tunes ATLAS-CSC, D6T, Perugia-0 and Perugia-11 and PHOJET) of ϕ differential cross section as a function of p_T in pp collisions at $\sqrt{s} = 2.76$ TeV.

5

Low mass dimuon analysis in p-Pb collisions at $\sqrt{s_{NN}} = 5.02$ TeV

Contents

The p-A collisions provide an example of a system where no hot, dense medium is formed in the final state, while its initial state is similar to that in A-A collisions. Since it is believed that the Quark Gluon Plasma is formed only in A-A collisions, the results from p-A analysis are important to provide a reference for A-A collisions and to give an insight on soft particle production in cold nuclear matter.

5.1 Data sample and applied selections

The data for p-Pb analysis were collected during January 2013 at $\sqrt{s_{NN}} = 5.02$ TeV.

The data were collected at forward rapidity, with the proton beam directed towards the Muon Arm (p-Pb) and at backward rapidity, with the lead beam directed towards the Muon Arm (Pb-p).
Due to the different energy of the proton (4 TeV) and the lead nucleus (1.58 A×TeV), the center of mass moves with a rapidity $y_0 = 0.465$ in the laboratory frame, where the Muon Arm covers the pseudorapidity region $2.5 < \eta_{lab} < 4.0$. As a consequence, the rapidity of the center of mass and the one of the laboratory do not coincide anymore: in p-Pb collisions, the rapidity of the center of mass is shifted of +0.465, and therefore is $2.03 < y_{cm} < 3.53$. In Pb-p collisions the rapidity of the center of mass is shifted of -0.465 and results to be $-4.46 < y_{cm} < -2.96$. A direct comparison between forward and backward is possible only in the rapidity window $2.96 < |y_{cm}| < 3.53$.
The data used for this analysis are the ones corresponding to the LHC13d and LHC13e periods (p-Pb analysis), and to LHC13f period (Pb-p analysis - see 6.8 for the complete list of runs).
As in the pp run, dimuons were collected using the unlike-sign and like-sign dimuon triggers, both with a threshold on the single muon p_T of about 0.5 GeV/c. The like-sign trigger sample was downscaled by a factor that varied from run to run, ranging from 10% to 29%.
The total integrated luminosity amounts to 5.03 ± 0.18 nb^{-1} in p-Pb and to 5.81 ± 0.19 nb^{-1} in Pb-p.
The same selections applied for the pp analysis (see cap4) were applied to these data too.
The number of opposite sign dimuon triggers satisfying the selections applied in our sample amounts to $N_{OS} \sim 9.27 \cdot 10^6$ in p-Pb and to $N_{OS} \sim 2.11 \cdot 10^7$ in Pb-p.

5.2 Background subtraction

The background was evaluated through the same event mixing technique used in pp analysis (see 4.2), with the only difference that the like-sign pairs collected with the like-sign trigger were upscaled, run by run, by the corresponding factor.
Fig. 5.1 shows the opposite-sign dimuon mass spectrum, together with the correlated background evaluated through the event mixing technique for p-Pb (left) and Pb-p collisions (right).

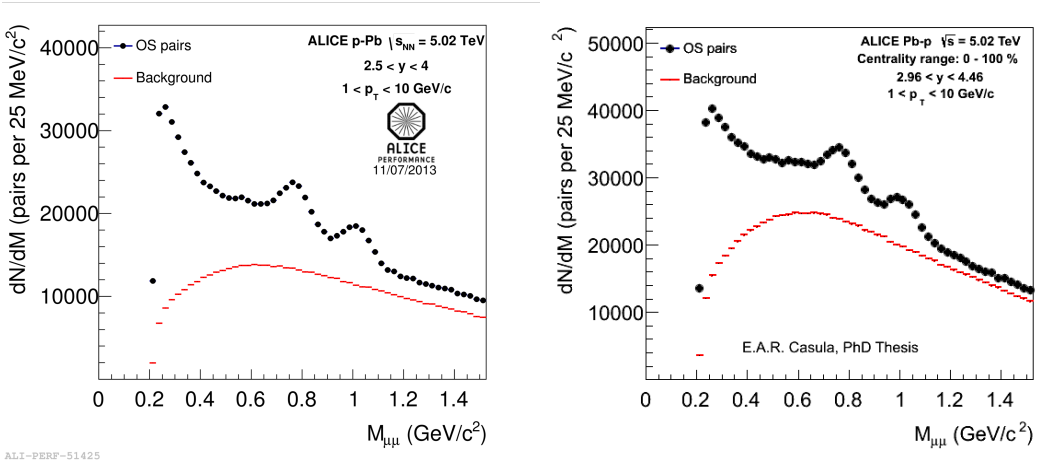

Figure 5.1: Opposite-sign dimuon mass spectrum and combinatorial background in p-Pb collisions (left) and in Pb-p collisions (right).

The ratio between signal and background is shown in fig. 5.2 for p-Pb (left) and Pb-p (right). Its value is ∼0.7 in p-Pb and ∼0.4 in Pb-p at the ϕ peak.

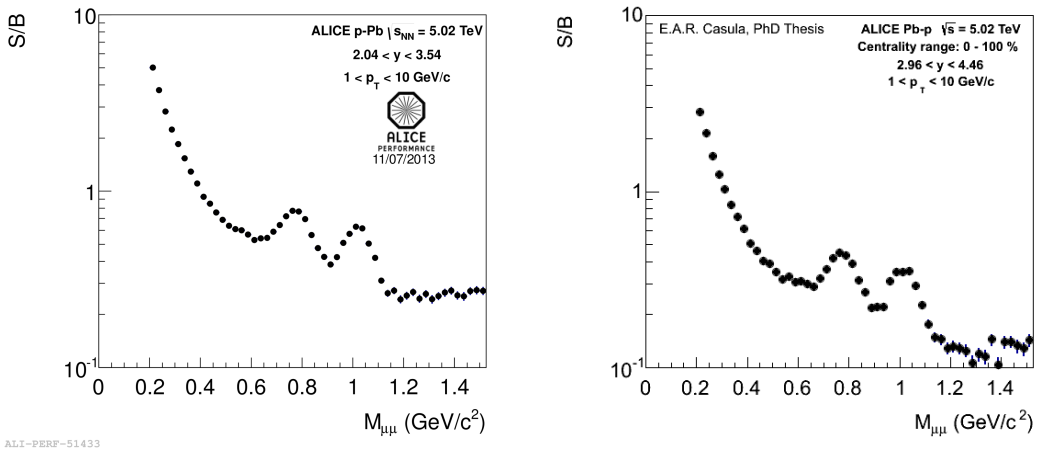

Figure 5.2: Signal/background ratio in p-Pb collisions (left) and in Pb-p collisions (right).

The quality of the background subtraction has been evaluated as in pp, looking at the ratio between the like-sign real and mixed pairs (see fig. 5.3). As in pp, the ratio is flat and its difference from unity, 1.5% in p-Pb and 1.1% in Pb-p, has been taken as the estimate of the systematic uncertainty on the background subtraction.

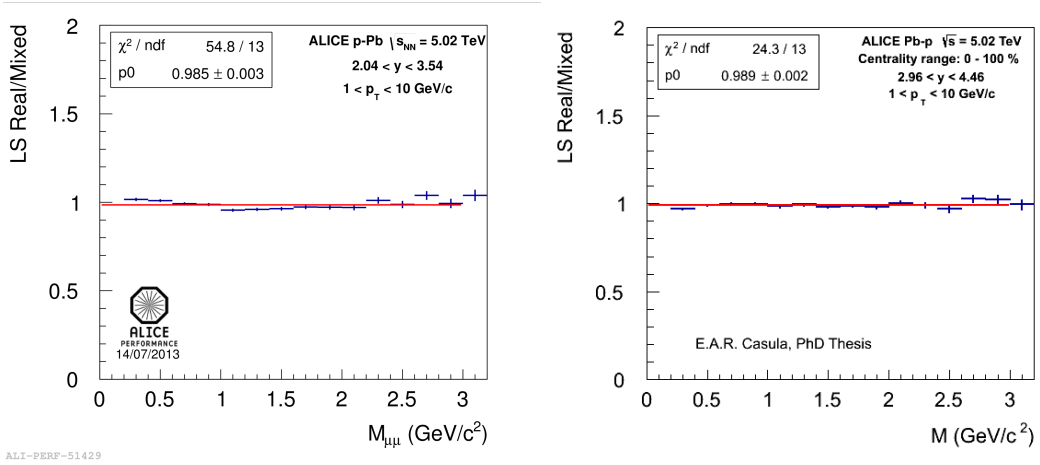

Figure 5.3: Ratio between the like-sign real and mixed pairs mass spectra in p-Pb (left) and Pb-p collisions (right) at 5.02 TeV.

5.3 Acceptance × efficiency correction

The acceptance × efficiency (A×ε) correction for ϕ and ω mesons was calculated as a function of the transverse momentum via a Monte Carlo simulations similar to that of pp analysis, as the ratio between the reconstructed and generated dimuons in a certain p_T interval, applying to the Monte Carlo reconstructed dimuons the same selections that were applied to the data.

The transverse momentum distribution for ϕ, ρ and ω mesons was tuned on the data, while the p_T parametrization of the other processes is based on a PYHTIA generation at 5.02 TeV. The parametrization of the other distributions is instead the same as the one of pp analysis at 7 TeV.

For the ϕ meson, in the p_T interval $1 < p_T < 7$ GeV/c, A×ε = 12.84% in p-Pb for 3.03 $< y <$ 3.53 and A×ε = 9.17% in Pb-p for -4.46 $< y <$ -2.96.

5.4 Signal extraction

Fig. 5.4 shows the signal after background subtraction fitted with the sources described in 3. The fit was performed fixing the same parameters as the ones in pp analysis (see 4.4).

The Open Beauty in p-Pb was fixed to the Open Charm via a preliminary fit of the full-p_T data sample in which both processes are left free: the resulting ratio is then kept

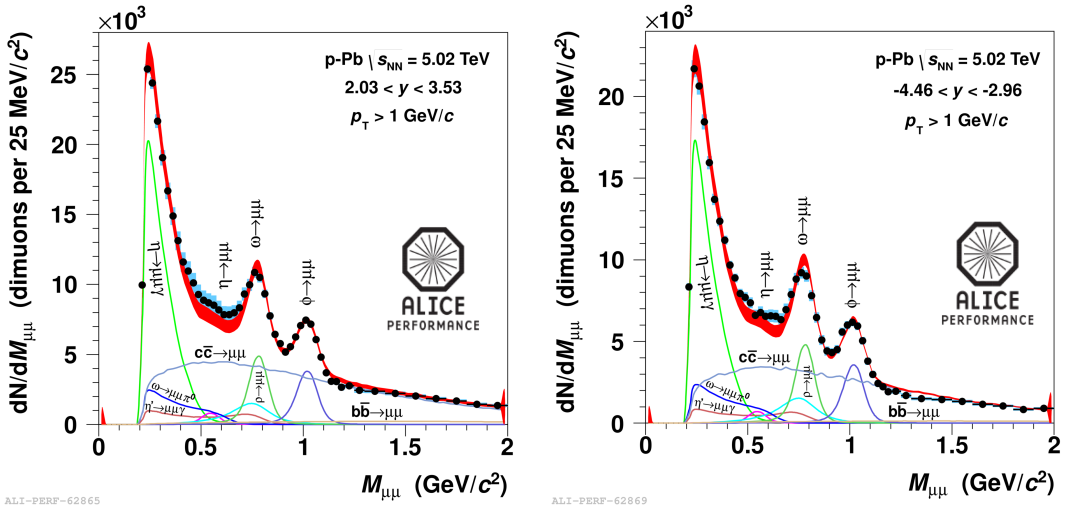

Figure 5.4: Dimuon invariant mass spectrum in p-Pb (left) and Pb-p (right) at $\sqrt{s} = 5.02$ TeV after combinatorial background subtraction for $1 < p_t < 10$ GeV/c (full circles). Light blue band: systematic uncertainty from background subtraction. Red band: sum of all simulated contributions. The width of the red band represents the uncertainty on the relative normalization of the sources.

fixed when fitting the mass spectra projected into the various p_T intervals considered, scaled via the p_T distributions of the two processes given by the MC simulations.

The raw number of ϕ extracted for $1 < p_T < 7$ GeV/c is 21062 $\pm$ 642 in p-Pb and 23358 $\pm$ 683 in Pb-p.

As in pp, an excess of about 10% is observed in the region $0.4 < M < 0.7$ GeV/c^2 in both p-Pb and Pb-p. This excess is more important at lower p_T and grows going toward midrapidites; it is sensible to the cut on the single muon p_T, since it decreases applying a cut at 1 GeV/c, suggesting a possible correlation with the trigger threshold. The excess is also sensible to the shape and normalization of the sources of the continuum, in particular to the relative normalization of Open Charm and Open Beauty.

The origin of the excess is still not completely clear: it seems however to not be a physical origin, since it depends on the rapidity of the laboratory frame and not on the rapidity of the centre-of-mass frame (see fig. 5.5).

The presence of the excess does not influence our analysis, since our work is focused mainly on ϕ and ω mesons. The fact that the excess is sensible to the cut on the single muon p_T and on the description of the continuum in the hadronic cocktail will

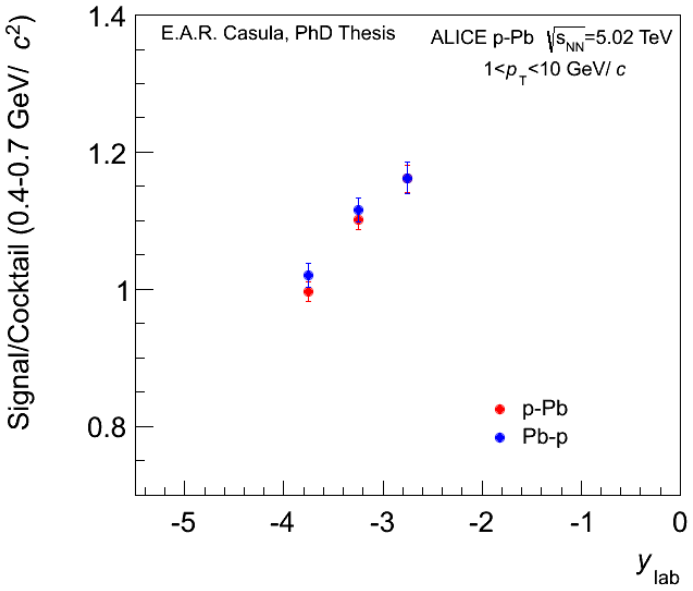

Figure 5.5: Integral of the signal/cocktail ratio in the region $0.4 < M_{\mu\mu} < 0.7$ GeV/c^2 as a function of the rapidity of the laboratory frame, for both p-Pb and Pb-p.

be anyway taken into account in the evaluation of the systematic uncertainty.

5.4.1 Systematic uncertainty on N_ϕ^{raw}

The systematic uncertainty on N_ϕ^{raw} was calculated in a similar way as in pp analysis at 2.76 TeV (see 4.4.1), fitting the signal with the same empirical functions f_1 (Crystal Ball + exponential + straight line) and f_2 (Crystal Ball + variable width Gaussian), and evaluating the systematics as the half of the maximum difference of the raw number of ϕ calculated with the three fitting methods (hadronic cocktail, f_1, f_2), taking the hadronic cocktail as reference. Fig. 5.6 shows the fits to the mass spectrum for $1 < p_T < 7$ GeV/c with f_1 and f_2 for both p-Pb and Pb-p.
The raw number of ϕ as a function of p_T, obtained with these fitting methods, is reported in fig. 5.7 for both p-Pb and Pb-p.
Besides this, other tests were also considered:

- varying the ratio between Open Beauty and Open Charm by a factor up to 50%, in order to take a reasonably wide range of variation for the shape of the total continuum;

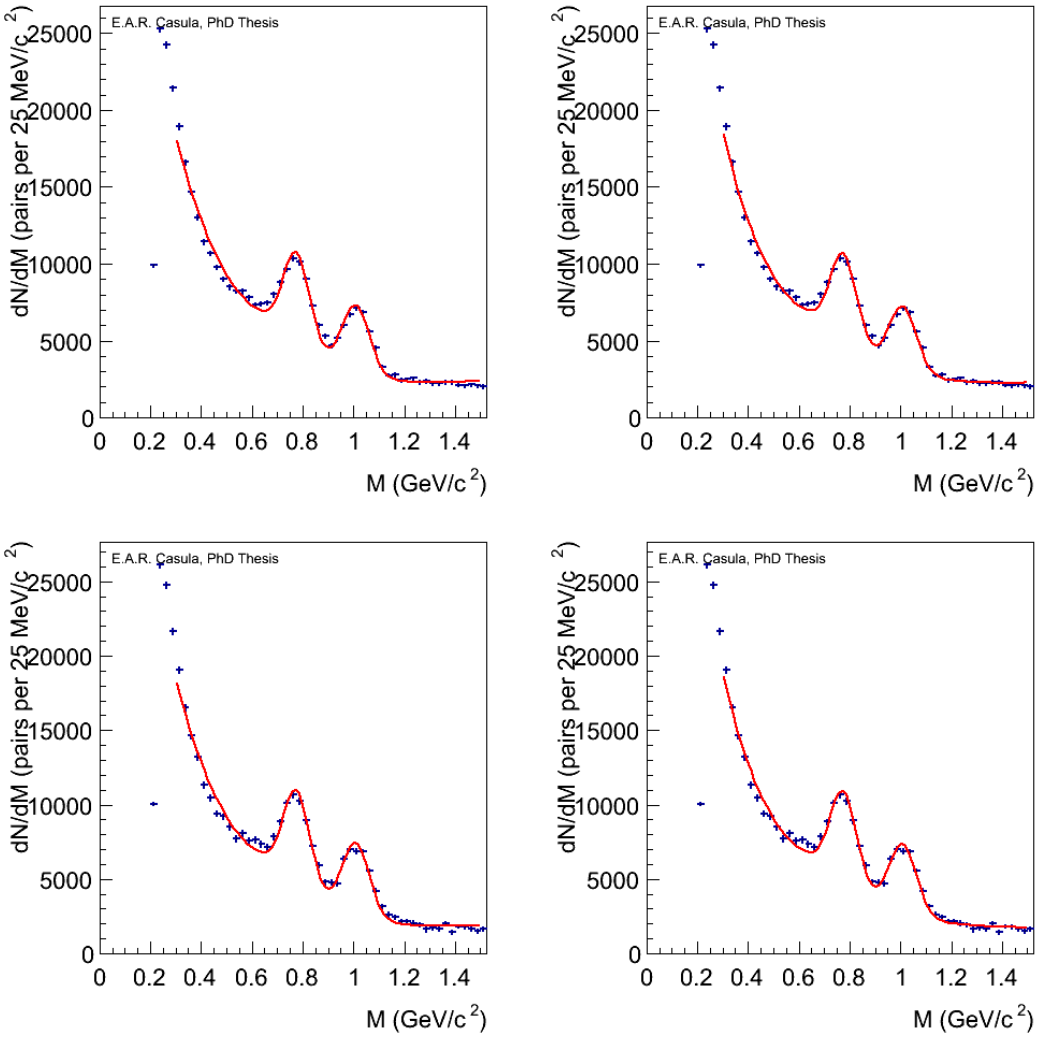

Figure 5.6: Fits to the mass spectrum for $1 < p_T < 7$ GeV/c with f_1 (left column) and f_2 (right column) in p-Pb (top) and Pb-p (bottom).

- excluding invariant masses from 0.4 to 0.65 GeV/c^2 from the fit, to test our sensitivity to the observed disagreement between data and MC in that region;
- varying the $\sigma_{\eta'}/\sigma_{\eta}$ ratio down to 0.2 and up to 0.4, in order to reproduce the uncertainty coming from a selection of various PYTHIA tunes;
- varying the $\sigma_{\rho}/\sigma_{\omega}$ ratio down to 0.8 and up to 1.2, corresponding to the uncertainty of the measured ratio in the analysis of pp data;

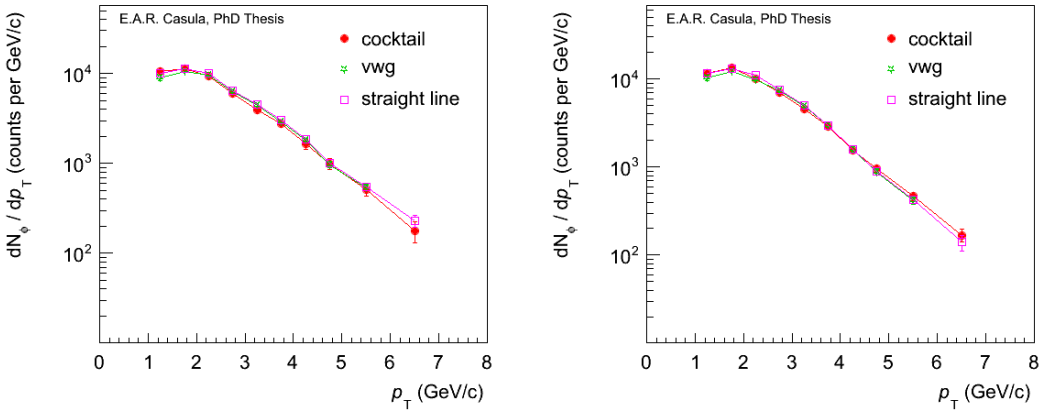

Figure 5.7: Raw number of ϕ vs p_T in p-Pb (left) and Pb-p (right) at $\sqrt{s}$ = 5.02 TeV obtained fitting the mass spectra with the hadronic cocktail (full circles), f_1 (open squares) and f_2 (open stars).

- varying the hypothesis on the BR of the Dalitz decay of the ω meson, down to $0.9 \cdot 10^{-4}$ and up to $1.7 \cdot 10^{-4}$, corresponding to ± 1 σ of the value cited in the PDG.

The raw number of ϕ extracted for different intervals of p_T between 1 and 7 GeV/c, with the corresponding systematic uncertainties and A$\times\varepsilon$ factors, are reported in tables 5.1 (p-Pb) and 5.2 (Pb-p).

Table 5.1: N_ϕ^{raw} with corresponding systematic uncertainty and A$\times\varepsilon$ factor in different p_T bins in p-Pb collisions at $\sqrt{s_{NN}}$ = 5.02 TeV

p_T	N_ϕ^{raw}	syst.	A$\times\varepsilon$
1-1.5 GeV/c	5216 ± 401	9.73%	6.45%
1.5-2 GeV/c	5598 ± 359	8.64%	12.32%
2-2.5 GeV/c	4710 ± 258	6.08%	19.71%
2.5-3 GeV/c	3017 ± 215	5.70%	25.93%
3-3.5 GeV/c	1978 ± 161	10.66%	31.70%
3.5-4 GeV/c	1367 ± 117	8.37%	34.49%
4-4.5 GeV/c	824 ± 99	6.99%	41.24%
4.5-5 GeV/c	494 ± 71	5.00%	41.34%
5-6 GeV/c	512 ± 79	6.24%	44.71%
6-7 GeV/c	178 ± 47	15.13%	47.07%

Table 5.2: N_{ϕ}^{raw} with corresponding systematic uncertainty and A×ε factor in different p_T bins in Pb-p collisions at $\sqrt{s_{NN}} = 5.02$ TeV

p_T	N_{ϕ}^{raw}	syst.	A×ε
1-1.5 GeV/c	5841 ± 516	7.53%	4.69%
1.5-2 GeV/c	6774 ± 392	6.52%	8.97%
2-2.5 GeV/c	5072 ± 260	7.25%	14.28%
2.5-3 GeV/c	3551 ± 171	4.51%	18.96%
3-3.5 GeV/c	2277 ± 122	5.28%	23.29%
3.5-4 GeV/c	1461 ± 87	2.48%	25.86%
4-4.5 GeV/c	776 ± 63	2.77%	29.87%
4.5-5 GeV/c	477 ± 45	5.00%	30.81%
5-6 GeV/c	464 ± 46	6.04%	33.45%
6-7 GeV/c	169 ± 27	9.35%	35.63%

5.5 ϕ yield

The ϕ yield has been evaluated as a function of p_T, calculating for each p_T bin the quantity:

$$Y(\Delta p_T) = \frac{N_{\phi}^{raw}(\Delta p_T)}{A\varepsilon(\Delta p_T) BR_{\phi \to e^+e^-} N_{MB}} \tag{5.1}$$

where N_{MB} is the number of minimum bias events, obtained scaling the number of opposite sign dimuon triggers N_{OS} by the normalization factor f_{norm}, according to the relation:

$$N_{MB} = f_{norm} * N_{OS} \tag{5.2}$$

The normalization factor f_{norm} has been evaluated as:

$$f_{norm} = \frac{N_{MB}^{trig}}{N_{OS\&MB}^{trig}} = \begin{cases} 1135.0 \pm 20.0 \text{ (stat.)} & \text{for p} - \text{Pb} \\ 585.5 \pm 6.0 \text{ (stat.)} & \text{for Pb} - \text{p} \end{cases} \tag{5.3}$$

where N_{MB}^{trig} is the number of events flagged with the minimum bias trigger and $N_{OS\&MB}^{trig}$ is the number of events triggered by both minimum bias and dimuon triggers.

The ϕ yield as a function of p_T is shown in fig. 5.8 for both p-Pb (left) and Pb-p (right). Confronting the two cases, it can be noticed that the yield is larger when the Pb beam is directed towards the Muon Arm.

The ϕ yield has been extracted also as a function of rapidity. Fig. 5.9, left side, shows it for $1 < p_T < 7$ GeV/c.

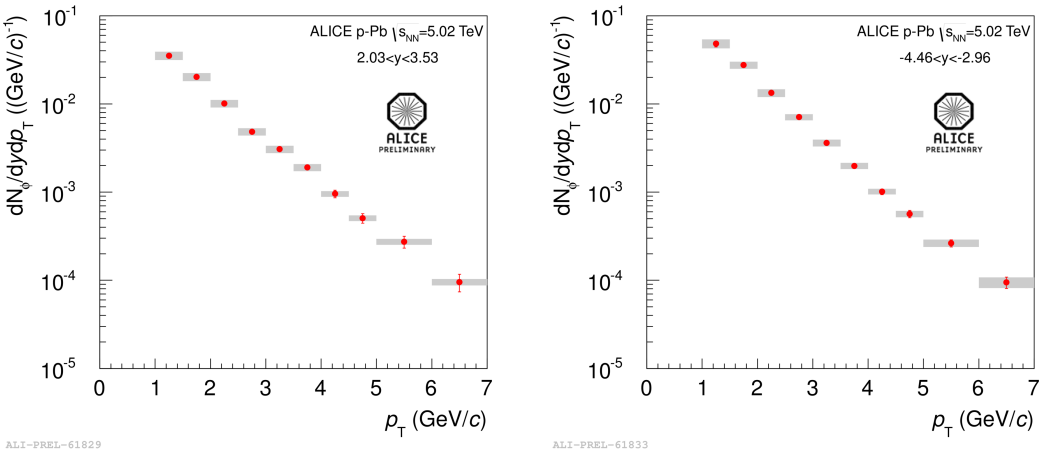

Figure 5.8: ϕ yield as a function of p_T in p-Pb (left) and Pb-p (right).

The asymmetry of the rapidity distribution is expected in p-A collisions; fig. 5.9, right side, shows for comparison the pseudorapidity distribution of charged particles measured by PHOBOS in Au-Au and d-Au collisions at $\sqrt{s_{NN}} = 200$ GeV [77], together with the measurement done by UA5 collaboration in p$\bar{\text{p}}$ collisions at 540 GeV [78]: here the asymmetry between pp(AA) and p-A collisions can be noticed at once.

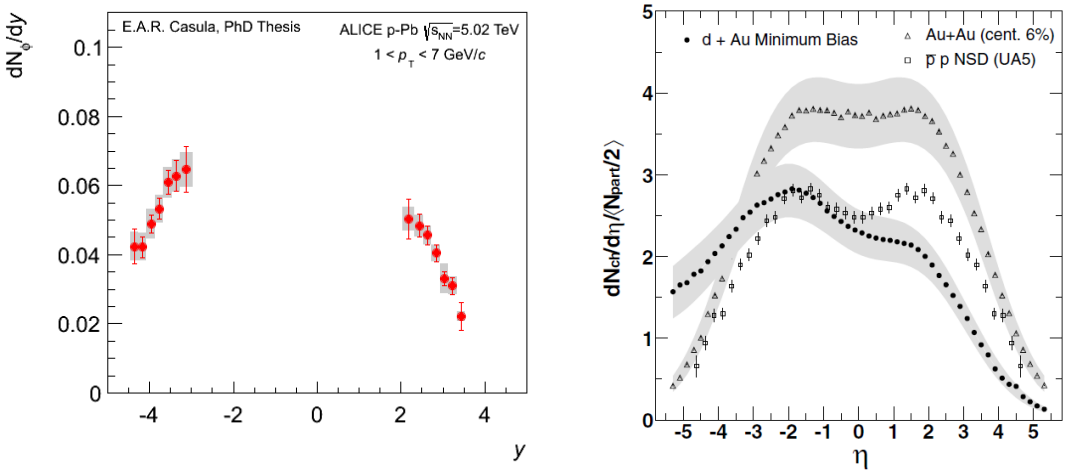

Figure 5.9: Left side: ϕ yield as a function of rapidity, for $1 < p_T < 7$ GeV/c. Right side: pseudorapidity distribution of charged particles measured by PHOBOS in Au-Au and d-Au collisions at $\sqrt{s_{NN}} = 200$ GeV and by UA5 in p$\bar{\text{p}}$ collisions.

5.5.1 Systematic uncertainty on the ϕ yield

In the evaluation of ϕ yield, several sources of systematic uncertainty have been taken into account:

- uncertainty on N_{ϕ}^{raw}, already described in 5.4.1;
- uncertainty on the evaluation of the branching ratio $BR_{\phi\to e^+e^-} = (2.954 \pm 0.030)\times10^{-4}$ (1%);
- uncertainty on the evaluation of the tracking efficiency. The value of this uncertainty has been obtained using an algorithm based on reconstructed tracks [79] and has been evaluated as the difference in the tracking efficiency between the data and the Monte Carlo. It amounts to 4% for p-Pb and to 6% to Pb-p collisions;
- uncertainty on the evaluation of the trigger efficiency. The systematic uncertainty arising from the intrinsic trigger efficiency was estimated by varying by 2% the efficiency of each local board in the simulation and amounts to 2%. This value was obtained by varying the cuts on the trigger tracks used to determine the intrinsic efficiency. This uncertainty is uncorrelated as a function of p_T and y. Another contribution comes from the uncertainty on the p_T trigger threshold. This contribution, amounting to 2%, has been evaluated in the Pb-Pb analysis (see 6.4.1.6), replacing the trigger response in the Monte Carlo with a function that fits the ratio between the p_T distributions of the muons that match two different trigger thresholds ($p_T \gtrsim 0.5$ GeV/c and $p_T \gtrsim 1$ GeV/c). The same approach could not be used in the p-Pb analysis, since the data in this case were collected with the $p_T \gtrsim 0.5$ GeV/c threshold only. In order to be conservative, we decided to consider also this contribution on the systematic uncertainty. It has to be noticed that if a sharp p_T cut on the single muon is applied ($p_T > 0.5$ GeV/c and $p_T > 1$ GeV/c), the difference in the number of ϕ corrected for A$\times\varepsilon$ is lower than the square root of the difference between the variances. This indicates that the A$\times\varepsilon$ correction does not introduce p_T dependent biases. The total value of the uncertainty related to the trigger efficiency amounts to 3%.

The values of ϕ yield in the different p_T bins, together with the statistical and the systematic uncertainties, are summarized in tables 5.3 and 5.4 for p-Pb and Pb-p respectively.

Table 5.3: ϕ yield as a function of p_T in different p_T in p-Pb collisions

p_T	yield	stat.	syst.
1-1.5 GeV/c	$355.8 \cdot 10^{-4}$	$27.4 \cdot 10^{-4}$	10.92%
1.5-2 GeV/c	$198.2 \cdot 10^{-4}$	$12.7 \cdot 10^{-4}$	10.34%
2-2.5 GeV/c	$106.5 \cdot 10^{-4}$	$5.8 \cdot 10^{-4}$	9.69%
2.5-3 GeV/c	$51.2 \cdot 10^{-4}$	$3.6 \cdot 10^{-4}$	9.63%
3-3.5 GeV/c	$27.6 \cdot 10^{-4}$	$2.2 \cdot 10^{-4}$	9.52%
3.5-4 GeV/c	$16.7 \cdot 10^{-4}$	$1.4 \cdot 10^{-4}$	9.19%
4.5-5 GeV/c	$5.0 \cdot 10^{-4}$	$0.7 \cdot 10^{-4}$	7.42%
5-6 GeV/c	$2.53 \cdot 10^{-4}$	$0.39 \cdot 10^{-4}$	7.47%
6-7 GeV/c	$0.79 \cdot 10^{-4}$	$0.21 \cdot 10^{-4}$	8.14%

Table 5.4: ϕ yield as a function of p_T in different p_T in Pb-p collisions

p_T	yield	stat.	syst.
1-1.5 GeV/c	$457.0 \cdot 10^{-4}$	$40.4 \cdot 10^{-4}$	11.90%
1.5-2 GeV/c	$279.1 \cdot 10^{-4}$	$16.1 \cdot 10^{-4}$	9.39%
2-2.5 GeV/c	$135.3 \cdot 10^{-4}$	$6.9 \cdot 10^{-4}$	10.18%
2.5-3 GeV/c	$69.4 \cdot 10^{-4}$	$3.3 \cdot 10^{-4}$	8.03%
3-3.5 GeV/c	$36.5 \cdot 10^{-4}$	$2.0 \cdot 10^{-4}$	9.09%
3.5-4 GeV/c	$20.7 \cdot 10^{-4}$	$1.2 \cdot 10^{-4}$	8.08%
4-4.5 GeV/c	$9.9 \cdot 10^{-4}$	$0.8 \cdot 10^{-4}$	7.50%
4.5-5 GeV/c	$5.7 \cdot 10^{-4}$	$0.5 \cdot 10^{-4}$	8.47%
5-6 GeV/c	$2.6 \cdot 10^{-4}$	$0.3 \cdot 10^{-4}$	9.66%
6-7 GeV/c	$0.9 \cdot 10^{-4}$	$0.1 \cdot 10^{-4}$	13.84%

5.5.2 ϕ yield as a function of p_T: comparison with models

The ϕ yield as a function of p_T, compared with HIJING[80] and DPMJET[81], is shown in fig. 5.10 for p-Pb (left) and Pb-p (right).

The integrated yield obtained from the data at forward rapidity is $(5.83 \pm 0.27) \cdot 10^{-2}$. The corresponding value obtained with HIJING is $(4.99 \pm 0.01) \cdot 10^{-2}$, while DPMJET gives $(4.75 \pm 0.01) \cdot 10^{-2}$.

At backward rapidity, the integrated yield from the data is $(7.66 \pm 0.38) \cdot 10^{-2}$. The value given by HIJING is $(6.50 \pm 0.01) \cdot 10^{-2}$ and the one obtained with DPMJET is $(3.08 \pm 0.01) \cdot 10^{-2}$.

Both models slightly underestimate the data in p-Pb, while in Pb-p they underestimate the data more severely; in particular, DPMJET underestimates the data in greater measure with respect to HIJING.

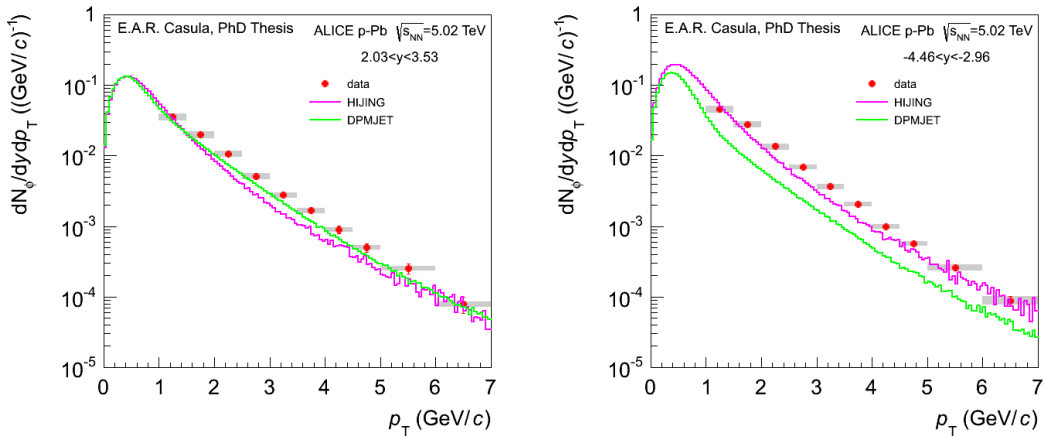

Figure 5.10: ϕ yield as a function of p_T compared with HIJING and DPMJET in p-Pb (left) and Pb-p (right).

5.6 σ_{pp} interpolation at 5.02 TeV

In order to calculate the ϕ nuclear modification factor, the reference cross section σ_{pp} at 5.02 TeV is needed. Since there was no direct measurement at 5.02 TeV, $\sigma_{pp}^{5.02TeV}$ has been obtained interpolating the differential cross sections measured in pp collisions at $\sqrt{s} = 2.76$ and at 7 TeV with three different functions: a straight line, a power-law and an exponential (see fig. 5.11).

The uncertainty on the interpolation has been calculated as the RMS of the $\sigma_{pp}^{5.02TeV}$ distribution obtained fluctuating 1000 times the experimental points.

The interpolated cross sections, relative to the $4.0 < y_{cms} < 2.5$ rapidity range of the reference pp measurements, were then scaled to the forward and backward rapidity windows $2.03 < y_{cms} < 3.53$ and $4.46 < y_{cms} < 2.96$. The relative scaling factors $f_{pPb} = 1.135 \pm 0.031$ and $f_{Pbp} = 0.850 \pm 0.028$ were evaluated as an average from simulations

with PHOJET and various tunes of PYTHIA; the uncertainties (amounting to about 3%) correspond here to the differences between the considered predictions and have been included in the systematic uncertainty.

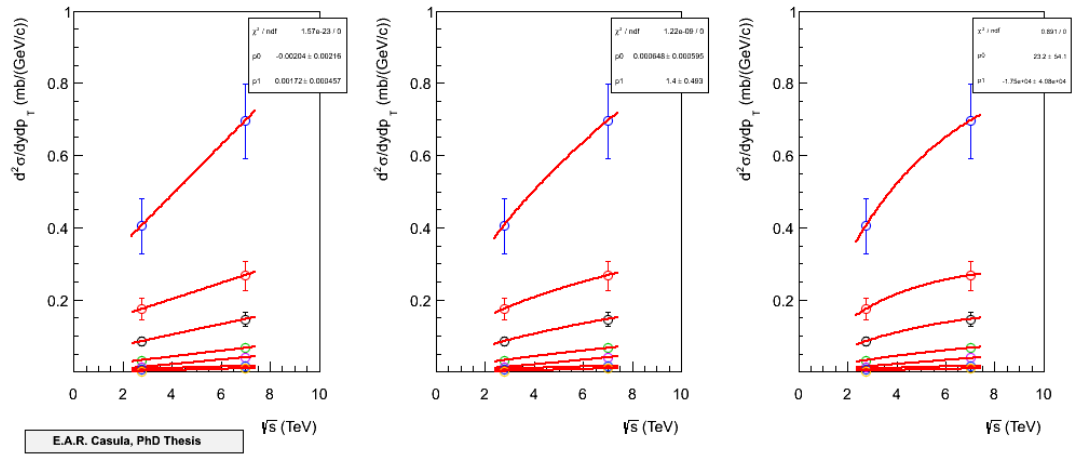

Figure 5.11: $d^2\sigma_{pp}/dydp_T$ values measured at 2.76 and at 7 TeV, interpolated with a straight line (left), a power-law (center) and an exponential (right).

The p_T-differential cross section at 5.02 TeV obtained through the interpolation, is shown in fig. 5.12, left side, where it is compared with the values at 2.76 and 7 TeV.

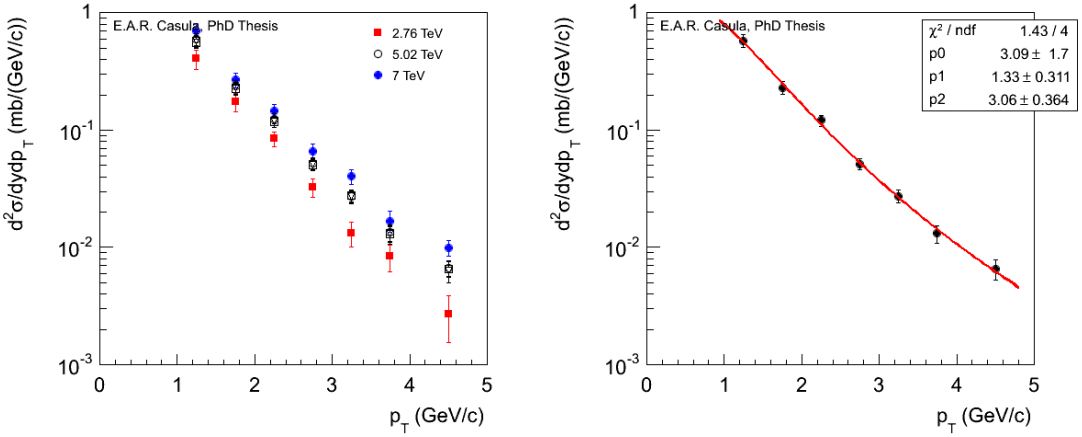

Figure 5.12: Left side: $d^2\sigma_{pp}/dydp_T$ (5.02 TeV) obtained through the interpolation, compared with $d^2\sigma_{pp}/dydp_T$ (2.76 TeV) and $d^2\sigma_{pp}/dydp_T$ (7 TeV). Right side: $d^2\sigma_{pp}/dydp_T$ (5.02 TeV) fitted with a power-law function

The systematic uncertainty due to the interpolation is taken as the half of the maximum

difference between the values given by the three functions.
Fig. 5.12, right side, shows the $d^2\sigma_{pp}/dydp_T$ (5.02 TeV) fitted with a power-law function. The replacement of the power-law with a Levy-Tsallis gives indistinguishable results in this p_T region. The values corresponding to $p_T > 5$ GeV/c are obtained extrapolating the mean value of the power-law and Levy-Tsallis functions at those values of p_T.
Values for $d^2\sigma_{pp}/dydp_T$ (5.02 TeV) in the various p_T bins, together with their systematic uncertainty, are summarized in table 5.5.

Table 5.5: $d^2\sigma_{pp}/dydp_T$ (5.02 TeV) obtained with the interpolation procedure in the various p_T bins and corresponding systematic uncertainty

p_T	$\frac{d^2\sigma_{pp}}{dydp_T}$ (5.02 TeV/c) [μb/GeV/c]	syst.
1-1.5 GeV/c	568.8	13.49%
1.5-2 GeV/c	257.3	6.84%
2-2.5 GeV/c	114.9	7.13%
2.5-3 GeV/c	54.0	6.93%
3-3.5 GeV/c	27.1	6.57%
3.5-4 GeV/c	14.5	8.74%
4-4.5 GeV/c	8.2	13.48%
4.5-5 GeV/c	4.9	19.43%
5-6 GeV/c	2.5	28.47%
6-7 GeV/c	1.1	41.76%

5.7 ϕ nuclear modification factor R_{pPb}

ϕ nuclear modification factor R_{pPb} has been calculated as:

$$R_{pPb} = \frac{Y(\Delta p_T)}{\sigma_{pp} T_{pPb}} \tag{5.4}$$

where σ_{pp} is the ϕ cross section at $\sqrt{s_{NN}} = 5.02$ TeV and T_{pPb} is the nuclear overlap function in p-Pb collisions, calculated with a fit based on the Glauber model of the VZERO amplitude distribution [82]: $T_{pPb} = 0.0983 \pm 0.0034$ mb^{-1}.
As already shown in 5.6, σ_{pp} was calculated through an interpolation between the measurements at $\sqrt{s} = 2.76$ and 7 TeV.
ϕ R_{pPb} at forward and backward rapidities as a function of p_T are shown in fig. 5.13. The nuclear modification factor is compatible with unity for $p_T > 3$ GeV/c at forward

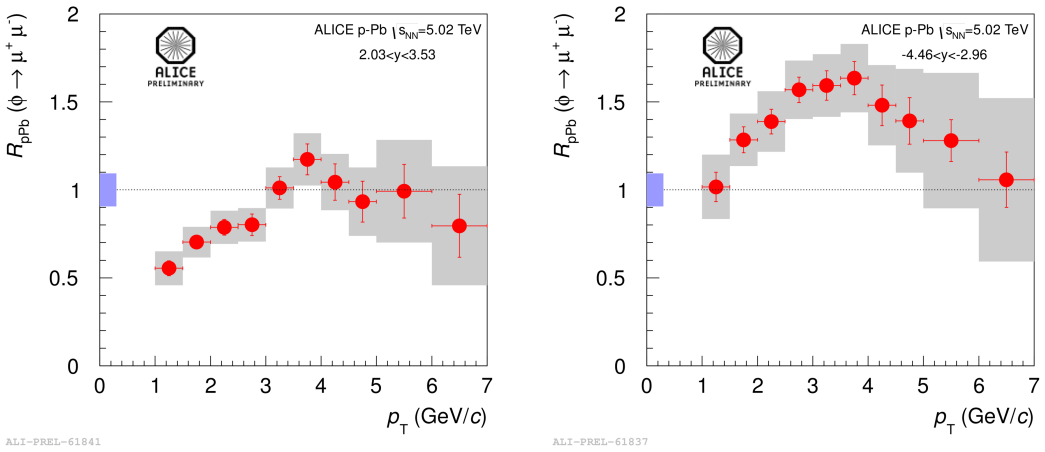

Figure 5.13: ϕ R_{pPb} at forward (left) and backward rapidity (right) as a function of p_T. The grey boxes represent the uncorrelated systematic uncertainties, while the lilac box represents the correlated ones.

rapidity and is larger at backward rapidity. This effect is due to the asymmetry in the particle production present between forward and backward rapidities.

5.7.1 Systematic uncertainty on ϕ R_{pPb}

Several sources of systematic uncertainty in the evaluation of ϕ R_{pPb} have been taken into account:

- systematic uncertainty on the ϕ yield, uncorrelated as a function of p_T, already calculated in 5.5.1;
- systematic uncertainty on σ_{pp}, correlated as a function of p_T, calculated in 5.6;
- systematic uncertainty on T_{pA}, correlated as a function of p_T (3.66%).

The values of the ϕ R_{pPb} at forward and backward rapidities in the different p_T bins, together with the systematic uncertainties bin to bin, are summarized in tables 5.6 and 5.7 respectively.

5.7.2 ϕ R_{pPb}: comparison with charged particles

The comparison between the ϕ R_{pPb}, obtained in the muon channel at both forward and backward rapidities, and the R_{pPb} of the charged particles measured with the Central

Table 5.6: ϕ R_{pPb} at forward rapidity as a function of p_T in different p_T bins (p-Pb collisions)

p_T	R_{pPb}	stat.	syst.
1-1.5 GeV/c	0.5595	0.0430	17.36%
1.5-2 GeV/c	0.6889	0.0442	12.40%
2-2.5 GeV/c	0.8292	0.4551	12.03%
2.5-3 GeV/c	0.8446	0.0603	11.86%
3-3.5 GeV/c	0.9090	0.0740	11.56%
3.5-4 GeV/c	1.0267	0.0878	12.68%
4-4.5 GeV/c	0.9879	0.1187	15.34%
4.5-5 GeV/c	0.9243	0.1333	20.80%
5-6 GeV/c	0.9155	0.1408	29.44%
6-7 GeV/c	0.6572	0.1745	42.50%

Table 5.7: ϕ R_{pPb} at backward rapidity as a function of p_T in different p_T bins (Pb-p collisions)

p_T	R_{Pbp}	stat.	syst.
1-1.5 GeV/c	0.9612	0.0849	17.99%
1.5-2 GeV/c	1.2979	0.0751	11.62%
2-2.5 GeV/c	1.4090	0.07226	12.43%
2.5-3 GeV/c	1.5373	0.0741	10.60%
3-3.5 GeV/c	1.6078	0.0860	11.22%
3.5-4 GeV/c	1.7073	0.1015	11.90%
4-4.5 GeV/c	1.4517	0.1183	15.43%
4.5-5 GeV/c	1.4048	0.1314	21.20%
5-6 GeV/c	1.2623	0.1264	30.07%
6-7 GeV/c	0.9877	0.1595	43.95%

Barrel in the kaon channel at midrapidity, for $|\eta| < 0.3$ [83], is shown in fig. 5.14. The ϕ R_{pPb} shape is similar to the one of the charged particles, even if its values are smaller in the entire p_T range in the case of forward rapidity. The R_{pPb} of the charged particles sits between the ϕ R_{pPb} at forward and backward rapidities.

A similar trend, where the nuclear modification factor grows as a function of p_T, tending to saturate at $p_T > 3$ GeV/c, was observed also at RHIC by PHOBOS and BRAHMS experiments.

Fig. 5.15 shows R_{dAu} of charged particles as a function of p_T measured by PHOBOS at midrapidity in d-Au collisions at $\sqrt{s_{NN}} = 200$ GeV, for three different pseudorapidity

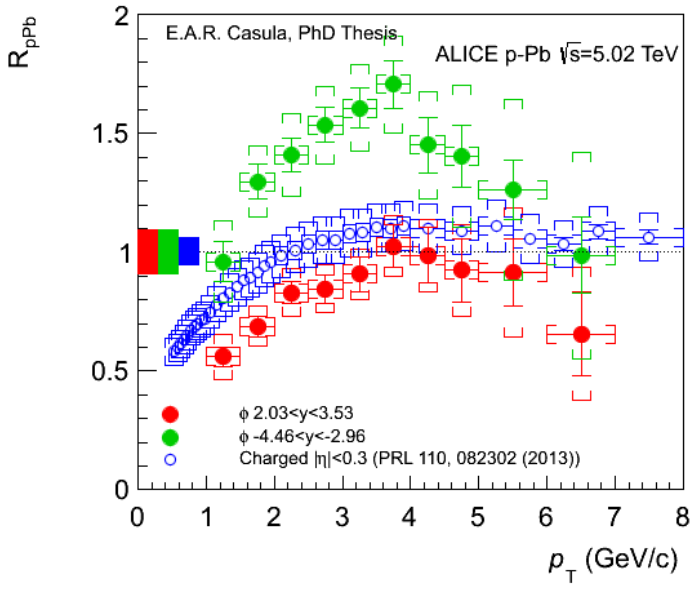

Figure 5.14: ϕ R_{pPb} as a function of p_T in the muon channel at forward rapidity compared with charged particles R_{pPb} in the kaon channel ad midrapidity. Statistics uncertainties are represented by the bars; square brackets represent the uncorrelated systematic uncertainties and the boxes are the correlated systematic uncertainties.

ranges ($0.2 < \eta < 0.6$, $0.6 < \eta < 1.0$, $1.0 < \eta < 1.4$) [84].

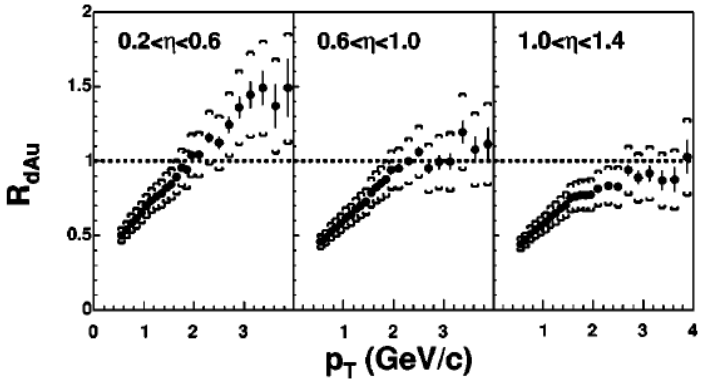

Figure 5.15: R_{dAu} of charged particles as a function of p_T in three different pseudorapidity ranges measured by PHOBOS in d-Au collisions at $\sqrt{s_{NN}}$ = 200 GeV. Brackets show the systematic uncertainty.

R_{dAu} of charged particles as a function of p_T at different pseudorapidities (η = 0, 1,

2.2, 3.2), measured by BRAHMS in d-Au collisions at $\sqrt{s_{NN}} = 200$ GeV [85] is instead shown in fig. 5.16.

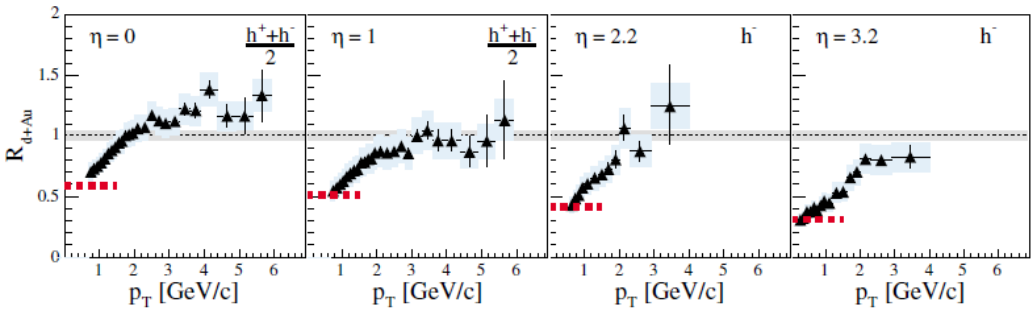

Figure 5.16: R_{dAu} of charged particles as a function of p_T at different pseudorapidities measured by BRAHMS in d-Au collisions at $\sqrt{s_{NN}} = 200$ GeV. One standard deviation statistical errors are shown with error bars. Systematic errors are shown with shaded boxes with widths set by the bin sizes. The shaded band around unity indicates the estimated error on the normalization to $\langle N_{coll} \rangle$. Dashed lines at $p_T < 1.5$ GeV/c show the normalized charged-particle density ratio $\frac{1}{\langle N_{coll} \rangle} \frac{dN/d\eta(\mathrm{Au})}{dN/d\eta(\mathrm{pp})}$.

5.8 Yield ratio of forward to backward rapidity R_{FB}

The R_{FB} is defined as the yield ratio of forward to backward region. The advantage in using R_{FB} consists in the fact that it does not depend on the interpolation used to calculate σ_{pp}, nor on the Glauber model used to calculate the nuclear overlap function. On the other hand, the analysis must be restricted to the common $|y_{cm}|$ region, of about half a rapidity unit, thus leading to a reduction of the usable statistics.
The R_{FB} of ϕ meson as a function of p_T was evaluated in the common rapidity window $2.96 < |y_{cm}| < 3.53$ as

$$R_{FB} = \frac{Y_{\phi}^{pPb}}{Y_{\phi}^{Pbp}}$$

It is shown in fig. 5.17. The first bin between 1 and 1.5 GeV/c has been excluded because of the very poor statistics in that bin in the rapidity window $2.96 < |y_{cm}| < 3.53$. The trend as a function of p_T is constant within uncertainties; R_{FB} integrated value in the range $1.5 < p_T < 7$ GeV/c is 0.53 ± 0.03, differing from unity by 47%: this is a consequence of the asymmetry in the particle production present between forward and backward rapidities.

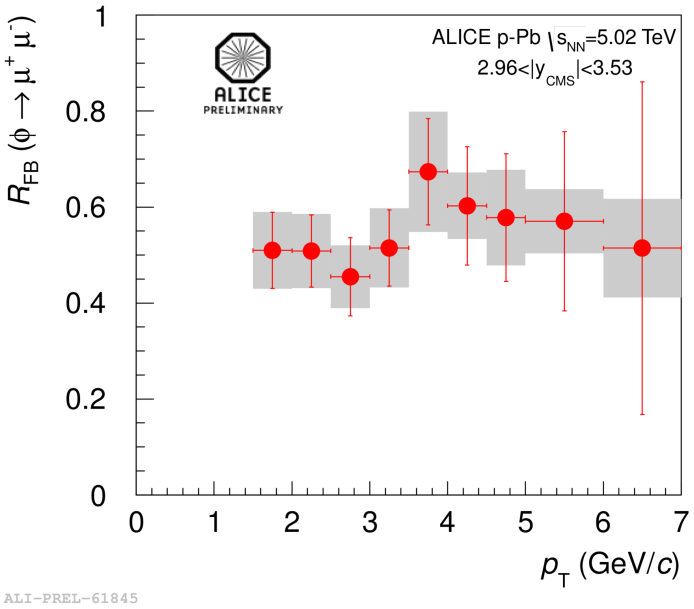

Figure 5.17: ϕ R_{FB} as a function of p_T for 2.96< $|y_{cm}|$ < 3.53.

The sources of systematic uncertainty in R_{FB} evaluation come only from the systematic uncertainty on the yields (see 5.5.1).

R_{FB} values bin to bin, together with their systematic uncertainty, are summarized in table 5.8.

Table 5.8: ϕ R_{FB} as a function of p_T in different p_T bins

p_T	R_{FB}	stat.	syst.
1.5-2 GeV/c	0.5096	0.0796	15.71%
2-2.5 GeV/c	0.5085	0.0754	15.20%
2.5-3 GeV/c	0.4547	0.0817	14.33%
3-3.5 GeV/c	0.5147	0.0797	16.04%
3.5-4 GeV/c	0.6737	0.1109	18.63%
4-4.5 GeV/c	0.6025	0.1234	11.52%
4.5-5 GeV/c	0.5781	0.1330	17.24%
5-6 GeV/c	0.5704	0.1870	11.76%
6-7 GeV/c	0.5144	0.3468	19.97%

6

Low mass dimuon analysis in Pb-Pb collisions at $\sqrt{s_{NN}} = 2.76$ TeV

Contents

6.1 Data sample and applied selections

The Pb-Pb run at LHC was performed in 2011 at $\sqrt{s_{NN}} = 2.76$ TeV.
The statistics consists of 134 runs (the complete run list is reported in 6.8), where the data were collected with the unlike and like-sign dimuon triggers (called *CPBI1MUL* and *CPBI1MLL*), with the hardware trigger threshold set at the low-p_T level ($p_T^{\mu} \gtrsim 1$ GeV/c). The collected opposite-sign dimuon triggers were $1.715 \cdot 10^7$.

6. LOW MASS DIMUON ANALYSIS IN PB-PB COLLISIONS AT $\sqrt{S_{NN}}$ = 2.76 TEV

We have performed our analysis taking into account four different centrality classes: 0-20%, 20-40%, 40-60% and 60-90%.
The centrality of the events was determined with a fit based on the Glauber model of the V0 amplitude distribution [82]; this fit allows also to extract variables such as the number of participants and the nuclear overlap function T_{AA} per slice of centrality.
The corresponding values of participating nucleons and T_{AA} for each centrality class are given in table 6.1

Table 6.1: Number of participating nucleons N_{part} and values of the nuclear overlap function T_{AA} for each centrality class.

Centrality	N_{part}	T_{AA} (mb^{-1})
0-20%	308.20 ± 3.40	18.93 ± 0.74
20-40%	157.30 ± 3.40	6.86 ± 0.28
40-60%	68.76 ± 2.40	2.00 ± 0.11
60-90%	17.55 ± 0.72	0.31 ± 0.03
0-90%	124.29 ± 2.29	6.26 ± 0.24

The selections applied to the data are:

- *physics selection* to remove the beam-gas background;
- both muon tracks reconstructed in the muon tracker match a tracklet reconstructed in the muon trigger at the low-p_T level ($p_T^\mu \gtrsim 1$ GeV/c);
- $2.5 < \eta_\mu < 4$ (to cut the tracks at the borders of the detector acceptance);
- $p_T^\mu > 0.85$ GeV/c: this cut elminates the residual muons that survive the trigger selection at low p_T. It has to be reminded that the trigger does not introduce a sharp p_T cut, but it is rather characterized by an efficiency that grows as a function of p_T, as shown in fig. 6.6;
- $\chi^2_\mu < 5$;
- $2.5 < y_{\mu\mu} < 4$;
- $p_T^{\mu\mu} > 2$ GeV/c (also consequence of the hardware trigger threshold set at ~ 1 GeV/c, thus causing a negligible ϕ acceptance $\times$ efficiency for $p_T < 2$ GeV/c).

In the mass region $0 < M < 10$ GeV/c^2, the numbers of muon pairs satisfying the applied selections are:

- $N_{\mu^+\mu^-} \sim 1.99 \cdot 10^6$
- $N_{\mu^+\mu^+} \sim 9.74 \cdot 10^5$
- $N_{\mu^-\mu^-} \sim 9.16 \cdot 10^5$

6.2 Background subtraction

To evaluate the combinatorial background, the event mixing technique already described for the pp analysis at 2.76 TeV has been used in Pb-Pb analysis too.
The event mixing was performed in this case requiring that the events to be mixed had similar event plane and centrality. We used 10 equally spaced bins in the event plane of the reaction between -$\pi/2$ and $\pi/2$, and 13 centrality bins that were not equally spaced, but that had the following boundaries: 0, 5, 10, 15, 20, 25, 30, 35, 40, 45, 50, 60, 70, 90%. These values were chosen on the basis of the centrality distribution of the events triggered by the dimuon triggers, as shown in fig. 6.1.

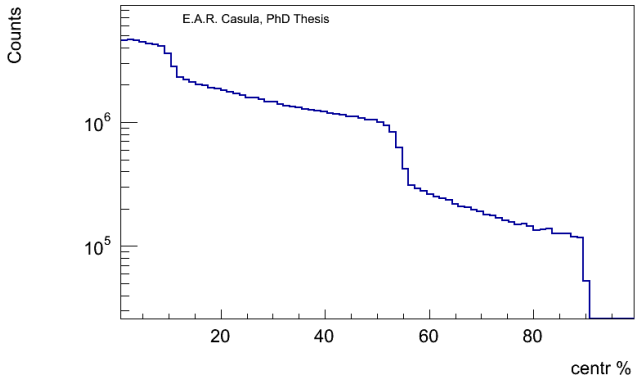

Figure 6.1: Centrality disdtribution of the events with dimuon triggers in Pb-Pb analysis.

The distribution obtained from the event mixing has been normalized to $2R\sqrt{N^{real}_{\mu^+\mu^+} N^{real}_{\mu^-\mu^-}}$. The R factor (already defined in 4.2) is equal to unity for $M_{\mu\mu} > 1$ GeV/c^2 and ranges between 0.9 and 1.03 for $M_{\mu\mu} < 1$ GeV/c^2. It is independent of centrality (see fig. 6.2). The opposite-sign mass spectra before the background subtraction, together with the background evaluated through the event mixing, are shown in fig. 6.3, for dimuon

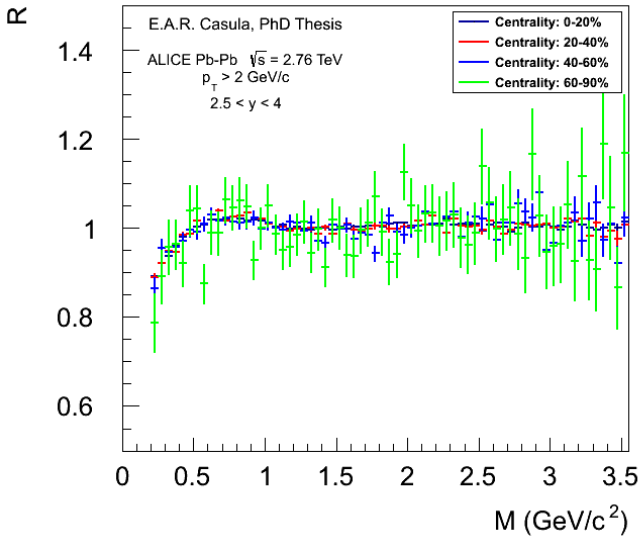

Figure 6.2: R factor as a function of the mass for different centrality bins for dimuon $p_T > 2$ GeV/c

$p_T > 2$ GeV/c, in the four centrality classes we have analyzed: looking at these plots, it can be noticed that ϕ and ω peaks are more defined and neater going from central to peripheral collisions. Fig. 6.4 shows the signal/background ratio in the same centrality classes: the S/B ratio for the ϕ grows from $\sim$ 0.07 in central collisions to $\sim$ 2 in peripheral collisions.

As it will be discussed later, the analysis has been restricted to $p_T > 2$ GeV/c, because for $p_T < 2$ GeV/c the hardware p_T trigger set at $p_T \gtrsim 1$ GeV/c does not allow to extract any signal.

In order to verify the quality of our background subtraction, the like-sign mass spectra obtained from the data have been compared with the ones obtained from the event mixing. Fig. 6.5 shows the ratio between the like-sign real and mixed spectra as a function of the mass, for dimuon $p_T > 2$ GeV/c.

The ratios are flat for $M_{\mu\mu} > 0.6$ GeV/c^2 and slightly greater than 1, differing from unity by about 2% for most central collisions.

This value has been taken as a conservative estimate of the systematic uncertainty on the background normalization.

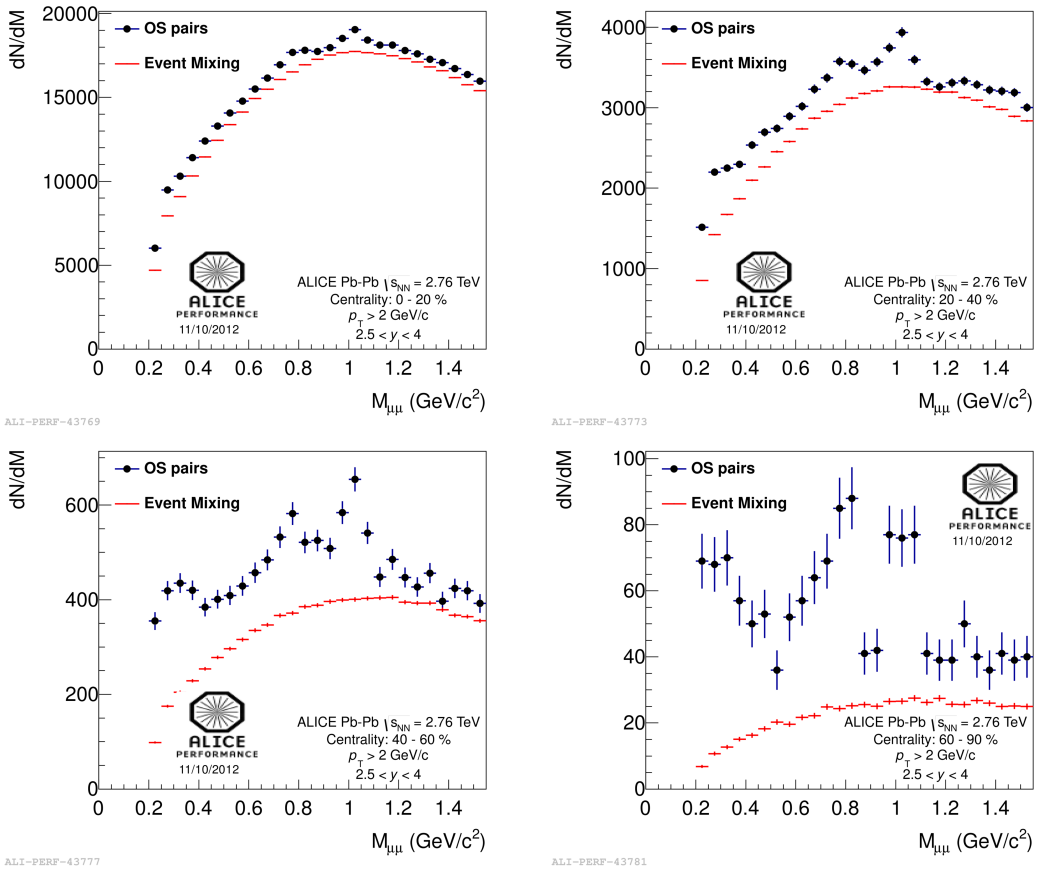

Figure 6.3: Raw mass spectra compared to event mixing in different centrality bins for dimuon $p_T > 2$ GeV/c.

6.3 Acceptance × efficiency correction

The use of the pure signal simulations to calculate A×ε, as done in pp and p-Pb analysis, does not allow the extraction of the reconstruction efficiency for the different sources as a function of the centrality, mandatory in the case of Pb-Pb analysis.

In order to do that, we had to perform simulations of the ϕ meson using the *embedding* technique.

The embedding Monte Carlo technique consists in simulating a signal particle and embedding the detector response into the raw data of a real event. The embedded event is then reconstructed as if it were a normal real event. The embedding technique has the advantage of providing the most realistic background conditions. Such realistic description is necessary if the environment (high particle multiplicity) could alter the

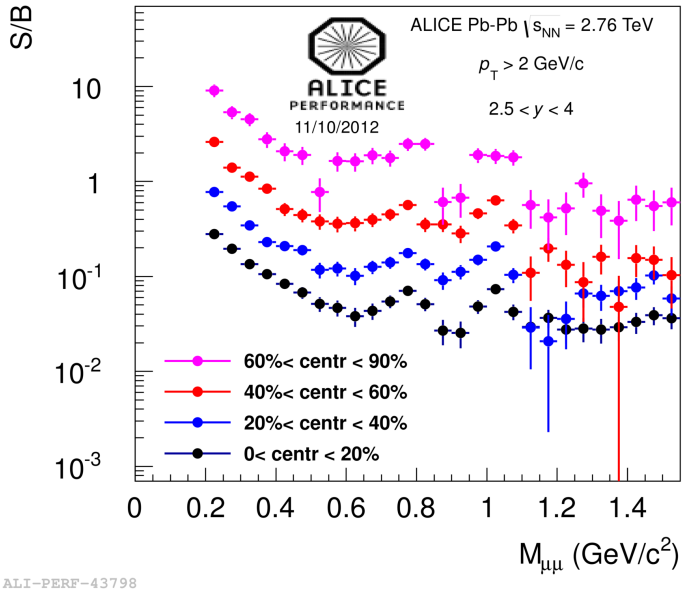

Figure 6.4: Signal/background ratio in different centrality bins for dimuon $p_T > 2$ GeV/c

track reconstruction efficiency, as it is the case in central Pb-Pb collisions.

Fig. 6.6 shows $A \times \varepsilon$ for ϕ meson as a function of p_T, integrated in centrality, obtained with the simulations performed with the embedding. It can be observed that $A \times \varepsilon$ is negligible for $p_T < 2$ GeV/c.

Simulations were performed using as input p_T distribution the one extracted from the pp analysis at 2.76 TeV [64]. In order to extract the ϕ acceptance $\times$ efficiency integrated for $2 < p_T < 5$ GeV/c, the input p_T distribution was replaced with the function that describes the data measured in central Pb-Pb collisions through the kaon channel at midrapidity. Fig. 6.7 shows the fit to the experimental points from KK channel with a Levy-Tsallis functionf_{Levy} (already defined in 4.5). For comparison the function that fits the pp data is also reported as a dashed line.

In order to extract the acceptance $\times$ efficiency with the correct function, we replaced the generated p_T distribution with $f_{Levy}(p_T)$, obtaining the corresponding reconstructed p_T distribution as $f_{Rec}(p_T) = f_{Levy}(p_T) \cdot A \times \varepsilon(p_T)$.

A$\times\varepsilon$ for $2 < p_T < 5$ GeV/c is calculated as:

$$A \times \varepsilon_{2-5} = \frac{\int_2^5 f_{rec}(p_T)dp_T}{\int_2^5 f_{gen}(p_T)dp_T}. \tag{6.1}$$

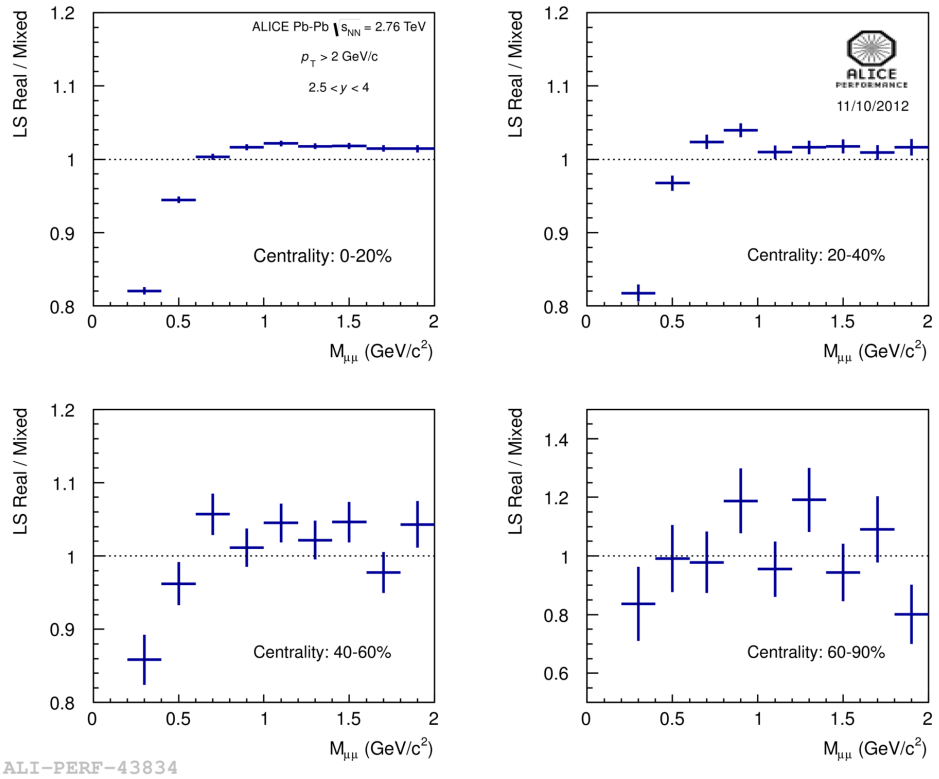

Figure 6.5: Like-sign pairs real/mixed ratio as a function of the mass in different centrality bins for dimuon $p_T > 2$ GeV/c (different range in y axis for centrality bins between 60 and 90%)

To evaluate the systematic uncertainty on the $A \times \varepsilon$ in the p_T range $2 < p_T < 5$ GeV/c, we have considered two different functions (the Levy-Tsallis f_{Levy} and an exponential, $f_{pow} = A \cdot p_T \cdot e^{-m_T/T}$) that fit the central barrel p_T distribution, and we have varied the content of each p_T bin according to its statistical error, refitting every time and recalculating $A \times \varepsilon$. The uncertainties so calculated are about 4% (see fig. 6.8).
The same method applied to ϕ was used to calculate ω acceptance × efficiency too, using the same function used for ϕ mesons, with the same parameters. ϕ and ω mesons A×ε as a function of centrality with their systematic uncertainty is shown in fig. 6.9. The values of $A \times \varepsilon$ for ϕ and ω are summarized in table 6.2 for the different centrality classes.

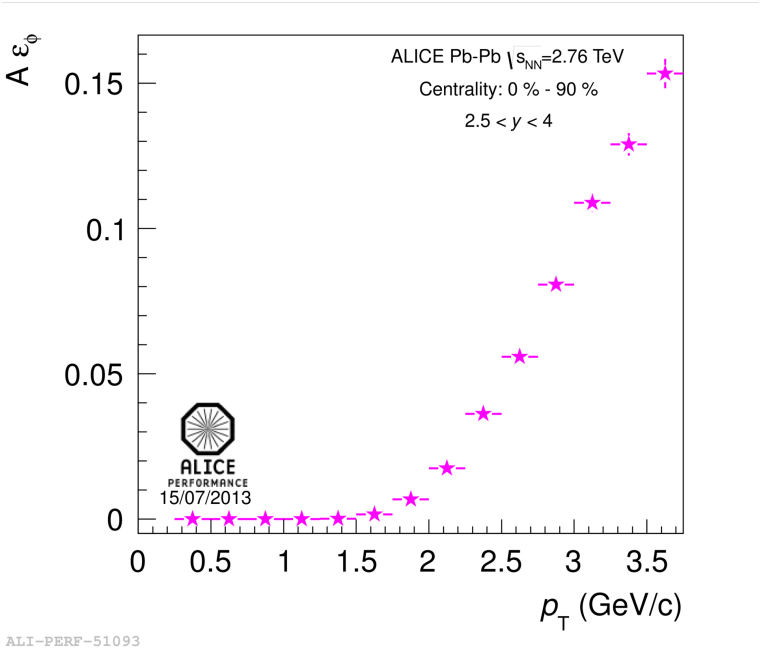

Figure 6.6: ϕ acceptance x efficiency as a function of p_T, integrated in centrality, from simulations with the embedding technique.

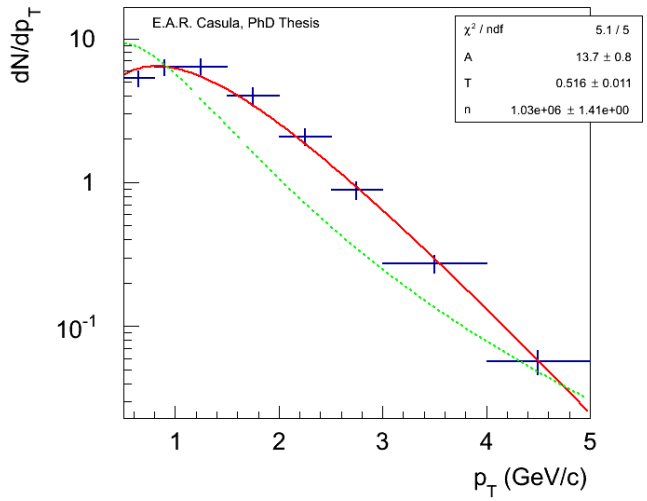

Figure 6.7: Fit to the experimental points from KK channel at midrapidity in Pb-Pb collisions at 2.76 TeV with f_{Levy} (red line). The green dashed line represents the function that fits the pp data in the muon channel at forward rapidity at 2.76 TeV.

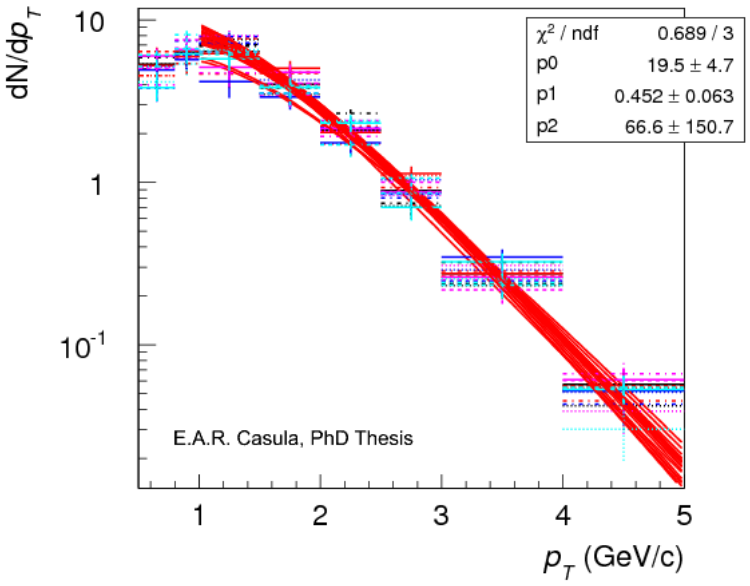

Figure 6.8: p_T distribution varied and fitted to calculate the systematic uncertainty on $A \times \varepsilon$.

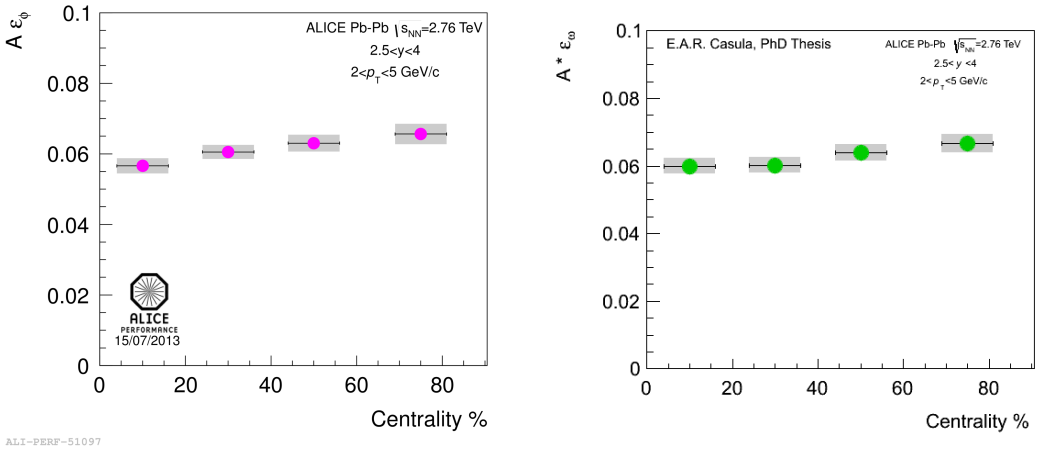

Figure 6.9: Acceptance x efficiency for ϕ and ω mesons as a function of centrality for embedding simulations ($2 < p_T < 5$ GeV/c).

6.4 Signal extraction

The fit to the dimuon invariant mass spectrum, for dimuon $p_T > 2$ GeV/c, is shown in figures 6.10 and 6.11, in the different centrality classes and integrated in centrality respectively.

Table 6.2: $A \times \varepsilon$ resampled values for ϕ and ω mesons in different centrality classes

Centrality	A×ε (ϕ)	syst.	A×ε (ω)	syst.
0-20%	5.66%	0.23	6.00%	0.23
20-40%	6.05%	0.22	6.03%	0.23
40-60%	6.30%	0.23	6.39%	0.25
60-90%	6.56%	0.31	6.67%	0.28
0-90%	5.55%	0.83	5.66%	0.89

The fit was performed with the contributions of the 2-body decays of $\rho + \omega$ and ϕ mesons, while the background processes have been described with an additional empirical function. This choice is due to the fact that there might be present other contributions than the ones coming from the hadronic cocktail, such as the in-medium modification of the ρ meson or the thermal dilepton continuum, to which, at this stage of the analysis, we are not interested, since our focus is on ϕ and ω mesons only. The normalization of the ρ relative to the ω was fixed requiring that $\sigma_\rho = \sigma_\omega$.
The raw number of ϕ and ω mesons, obtained for the four centrality classes and for dimuon $2 < p_T < 5$ GeV/c, is reported in table 6.3.

Table 6.3: N_ϕ^{raw} and N_ω^{raw} in different centrality bins for dimuon $2 < p_T < 5$ GeV/c

Centrality	N_ϕ^{raw}	N_ω^{raw}
0-20%	1506 ± 335	1675 ± 376
20-40%	1022 ± 148	1002 ± 165
40-60%	448 ± 58	467 ± 64
60-90%	111 ± 20	143 ± 22
0-90%	3073 ± 371	3271 ± 417

In fig. 6.12 the fit to the mass spectrum is shown for $1 < p_T < 2$ GeV/c, for $p_T^\mu > 0.85$ GeV/c: extracting a signal in this cases is not possible, because of the high p_T threshold ($\sim$1 GeV/c) of the low-p_T trigger.It was therefore decided to limit the analysis to dimuon $p_T > 2$ GeV/c.

6.4.1 Systematic uncertainties on signal extraction

In the evaluation of the systematic uncertainty in the raw number of ϕ extracted, several sources have been taken into account:

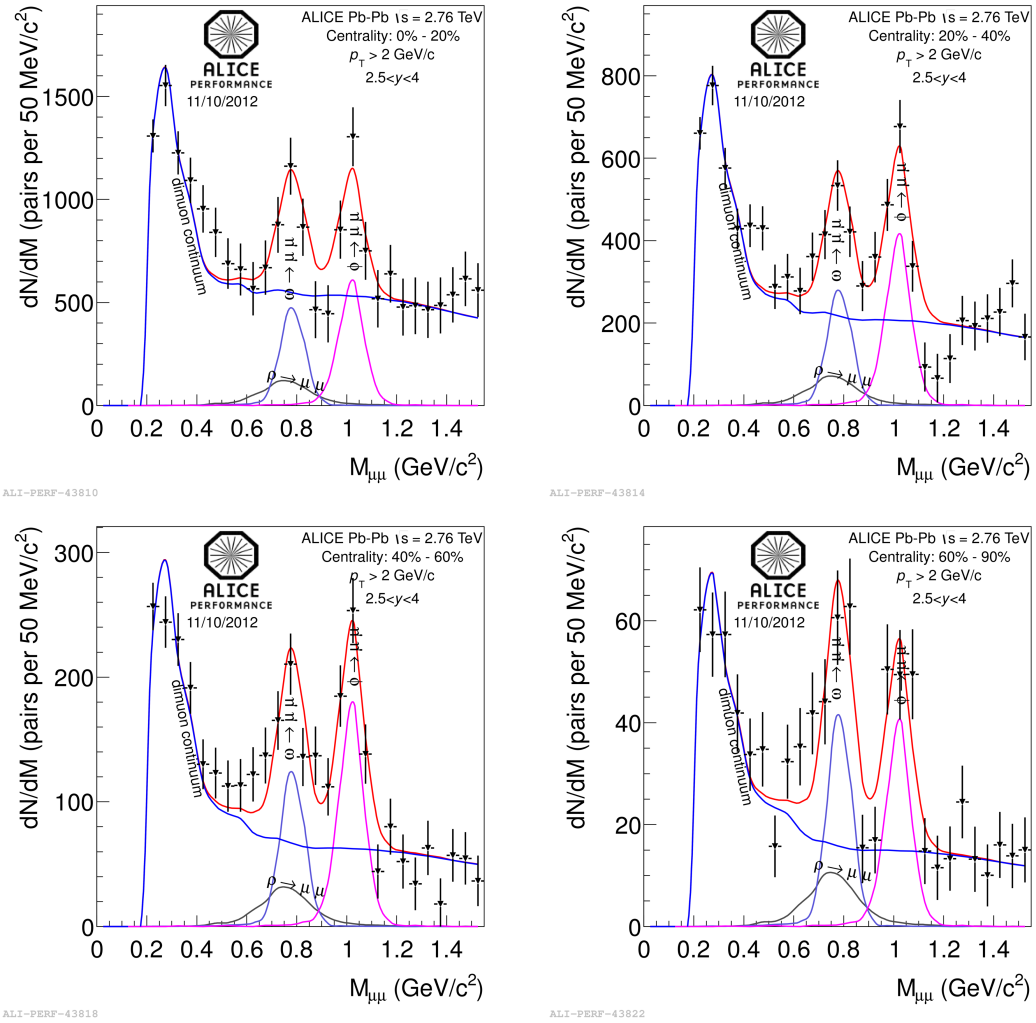

Figure 6.10: Fit to the mass spectrum in different centrality classes for dimuon $p_T > 2$ GeV/c in Pb-Pb collisions at 2.76 TeV

- background subtraction;
- cut on single muon p_T;
- description of the correlated background;
- mass fit range;
- tracking efficiency;
- trigger efficiency.

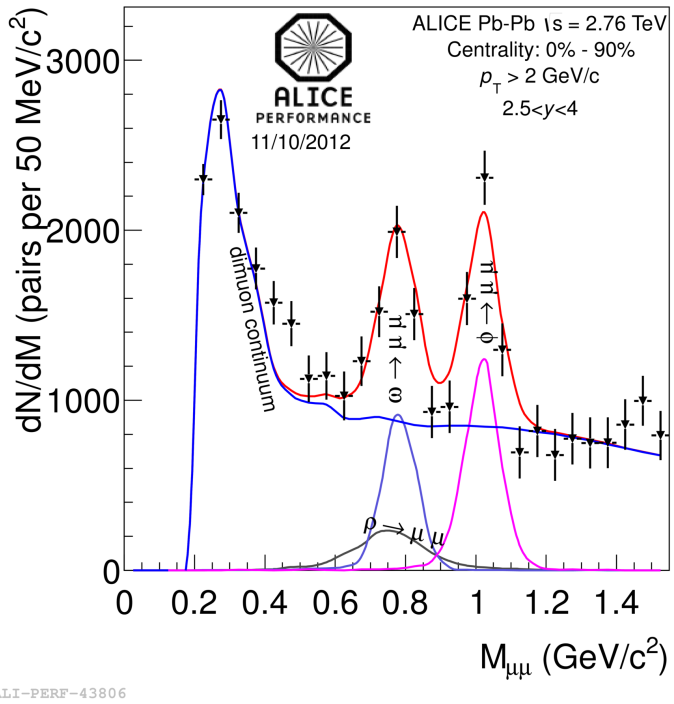

Figure 6.11: Fit to the mass spectrum integrated in centrality for dimuon $p_T > 2$ GeV/c in Pb-Pb collisions at 2.76 TeV

6.4.1.1 Uncertainty due to background subtraction

To evaluate the uncertainty related to the background subtraction, the background normalization has been varied by ± 2% (see figure 6.13), corresponding to the difference from unity in the ratio between like sign real and mixed pairs mass spectra, as discussed in 6.2. Applying this variation in both the directions, the level of the continuum is modified, but the raw number of ϕ for the most central bin varies only by 3.8% in central collisions, varying by a quantity lower than 1% for centralities higher than 20%: it has to be noticed that this is a much smaller value with respect to the statistical error.

6.4.1.2 Uncertainty due to the cut on single muon p_T

To evaluate the uncertainty related to the cut on single muon p_T, we have applied three different cuts (0.7, 0.85 and 1 GeV/c, see fig. 6.14); the variations on the number of N_ϕ corrected by the corresponding A×ε go from 2.6% to 9% depending on centrality.

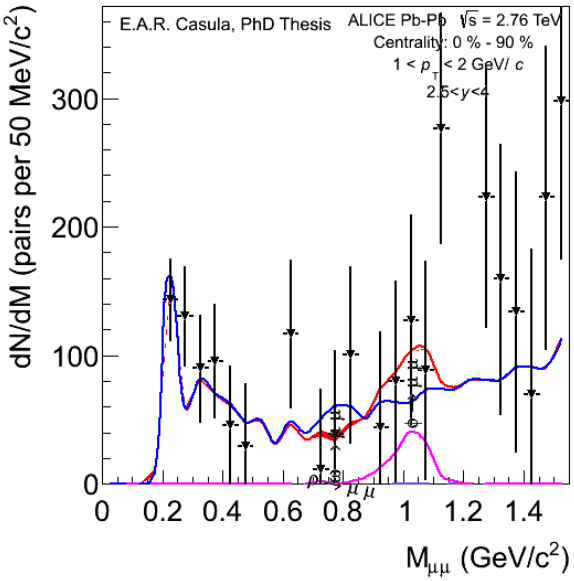

Figure 6.12: Fit to the mass spectrum integrated in centrality for $1 < p_T < 2$ GeV/c, for $p_T^{\mu} > 0.85$ GeV/c.

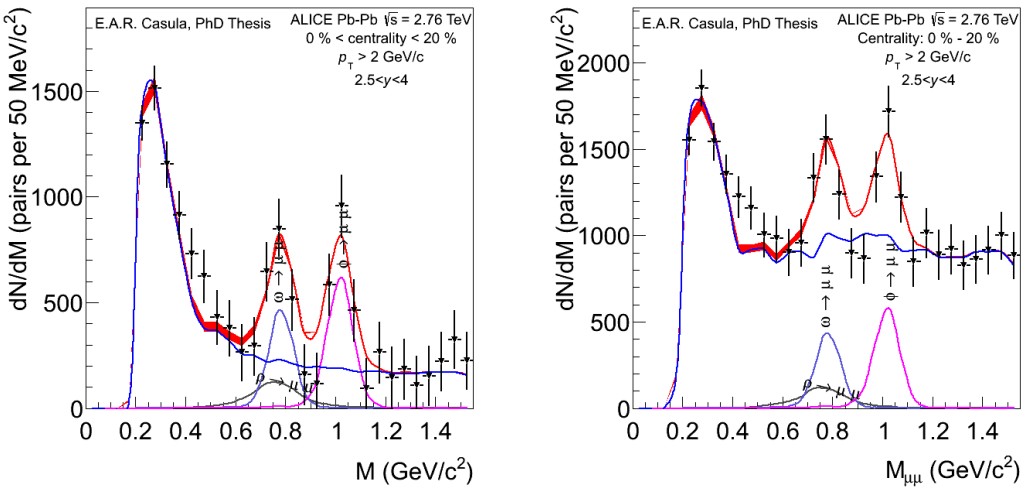

Figure 6.13: Fit to the mass spectrum for the 0-20% centrality class for dimuon $p_T > 2$ GeV/c, with a +2% variation (left side) and -2% variation (right side) on background normalization

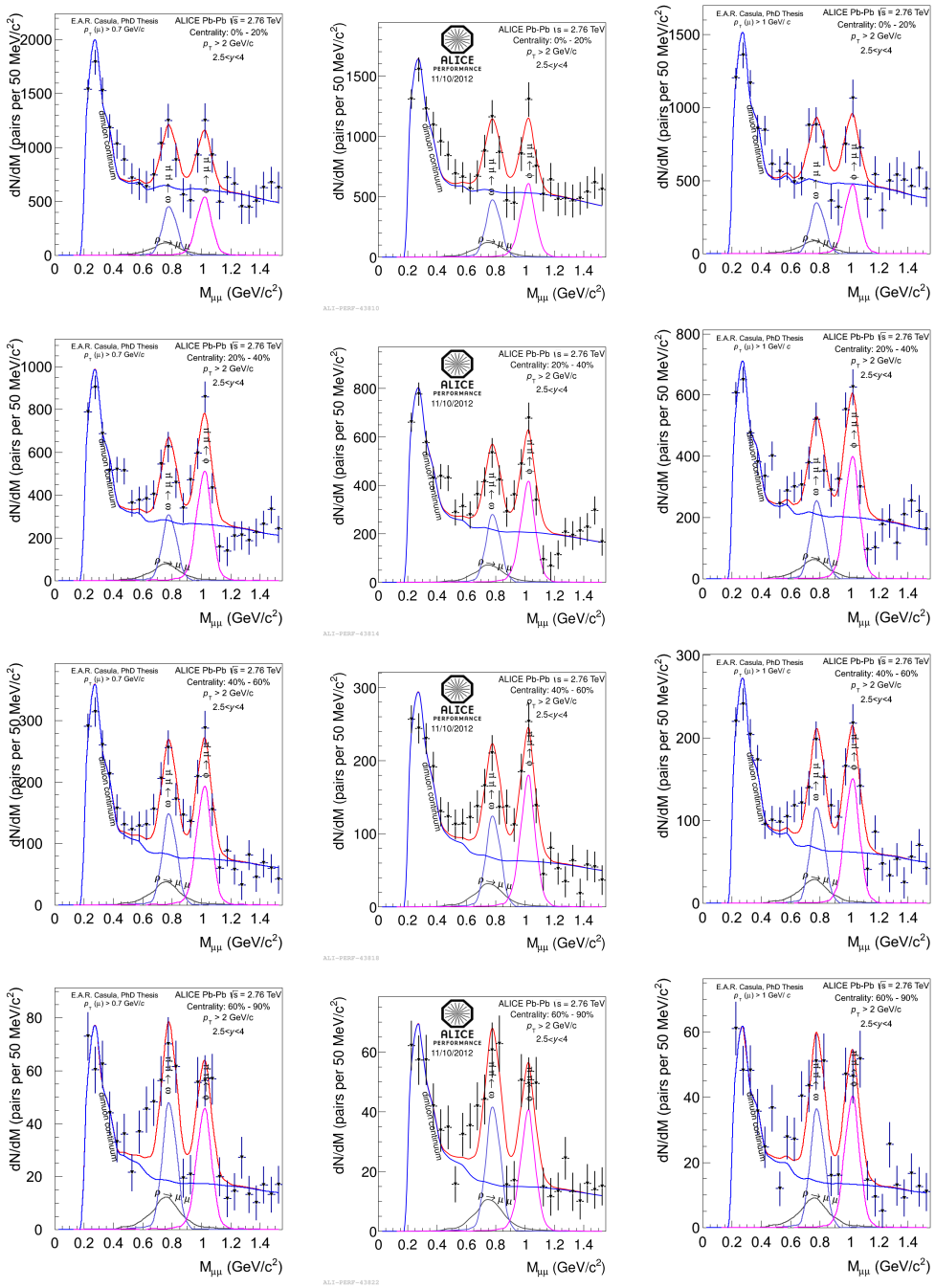

Figure 6.14: Fits to the mass spectrum for the different centrality classes for dimuon $p_T > 2$ GeV/c with different single muon p_T cuts: 0.7 GeV/c (left), 0.85 GeV/c (center), 1 GeV/c (right)

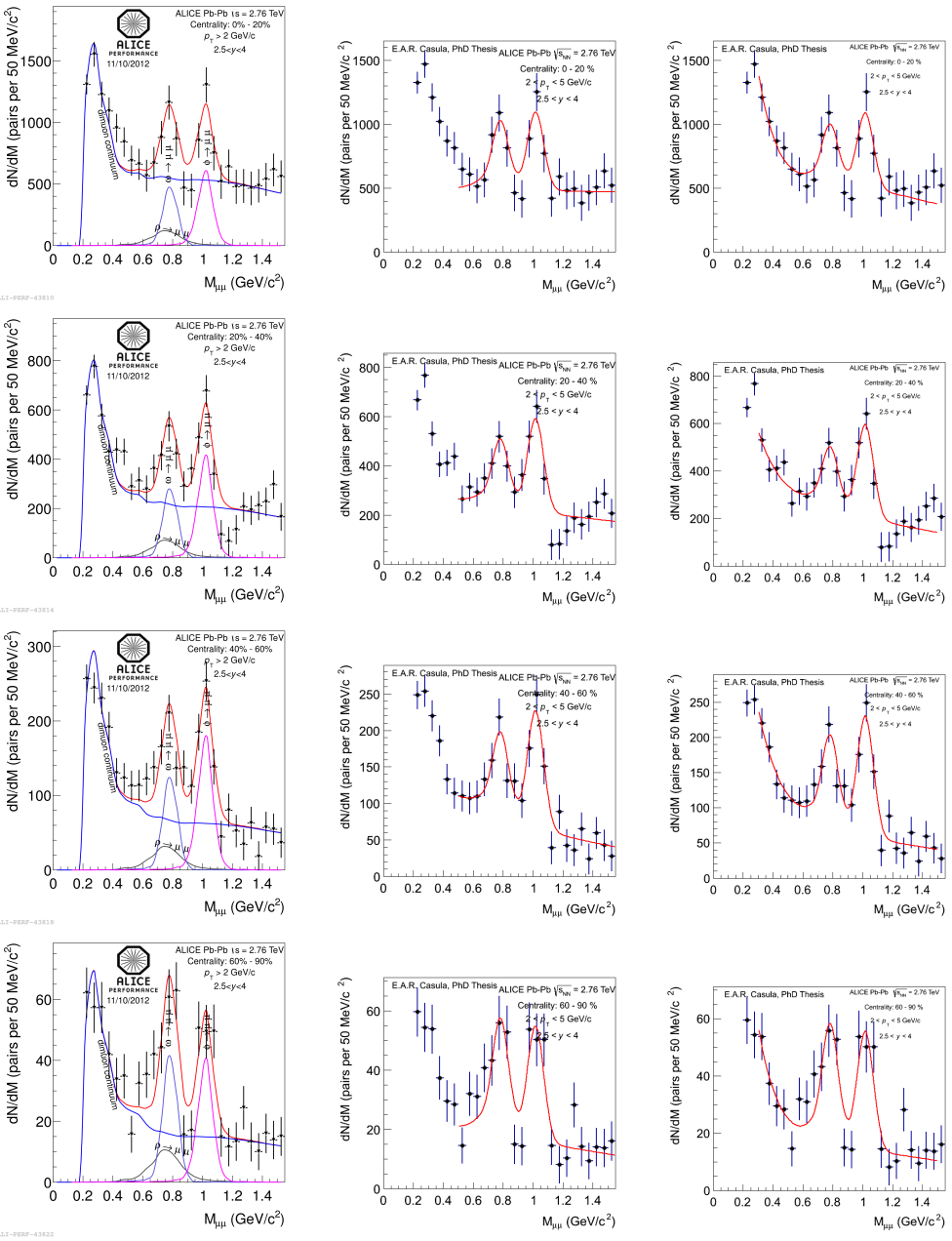

Figure 6.15: Fits to the mass spectra for the different centrality classes for dimuon $p_T > 2$ GeV/c with different functions: hadronic cocktail (left); Crystal Ball for ϕ and $\rho+\omega$ peaks and exponential + constant for the other processes (center); Crystal Ball for ϕ and $\rho+\omega$ peaks and exponential + Landau function for the other processes (right)

6.4.1.3 Uncertainty due to the description of the correlated background

To evaluate the uncertainty coming from the description of the correlated background, a fit with two empirical functions alternative to the hadronic cocktail, was performed. In these functions, ϕ and $\rho+\omega$ peaks were described by Crystall Ball functions (already defined in 4.4.1), while to describe the other processes, an exponential plus a constant, or an exponential plus a Landau function, were used (see fig. 6.15). The fit with the hadronic cocktail was taken as reference. In this case we have variations in N_{ϕ}^{raw} that go from 3.15% to 6.21%, depending on centrality.

6.4.1.4 Uncertainty due to the range in the fit to the mass spectrum

We have evaluated the systematic uncertainty coming from the range in the fit to the mass spectrum, considering three different fit ranges: $0.2 < M_{\mu\mu} < 1.5$ GeV/c^2 (taken as reference), $0.2 < M_{\mu\mu} < 1.8$ GeV/c^2 and $0.2 < M_{\mu\mu} < 2.0$ GeV/c^2 (see fig. 6.16). The differences in the raw number of ϕ vary from 1.5% to 3.3%, depending on centrality.

6.4.1.5 Uncertainty due to the tracking efficiency

The systematic uncertainty on the tracking efficiency has several components [86]: a first contribution of 4% is given by the measured differences on the tracking efficiencies in simulations and in peripheral events from real data. This uncertainty is correlated as a function of centrality.
An additional systematic uncertainty of 2% is due to the correlated dead areas, which are dead areas located in front of each other in the same tracking station and that lead to an overestimation of the efficiency. Also this uncertainty is correlated as a function of centrality.
Adding in quadrature these components, we have eventually a systematic uncertainty of 4.5% in all centrality classes.

6.4.1.6 Uncertainty due to the trigger efficiency

To evaluate the systematic uncertainty on the trigger efficiency, the first step has been to fit the ratio of the events with two different trigger thresholds (events with $p_T \gtrsim 1$ GeV/c, from now on called p_{T1} threshold, over events with $p_T \gtrsim 0.5$ GeV/c,

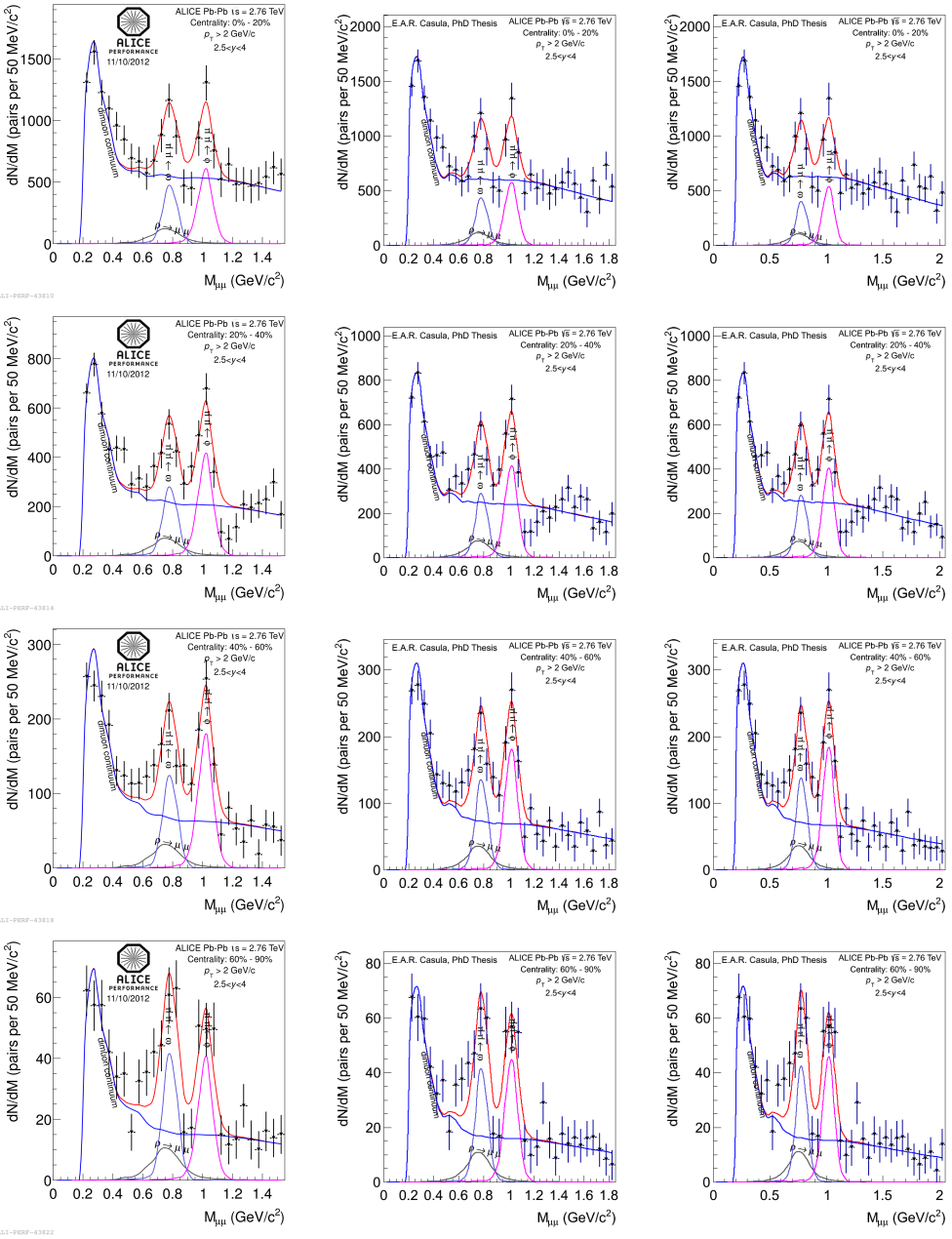

Figure 6.16: Fits to the mass spectra for the different centrality classes for dimuon $p_T > 2$ GeV/c with different mass fit range: $0.2 < M_{\mu\mu} < 1.5$ GeV/c^2 (left), $0.2 < M_{\mu\mu} < 1.8$ GeV/c^2 (center) and $0.2 < M_{\mu\mu} < 2.0$ GeV/c^2 (right).

from now on called p_{T2} threshold), as a function of p_T, in minimum bias events, with

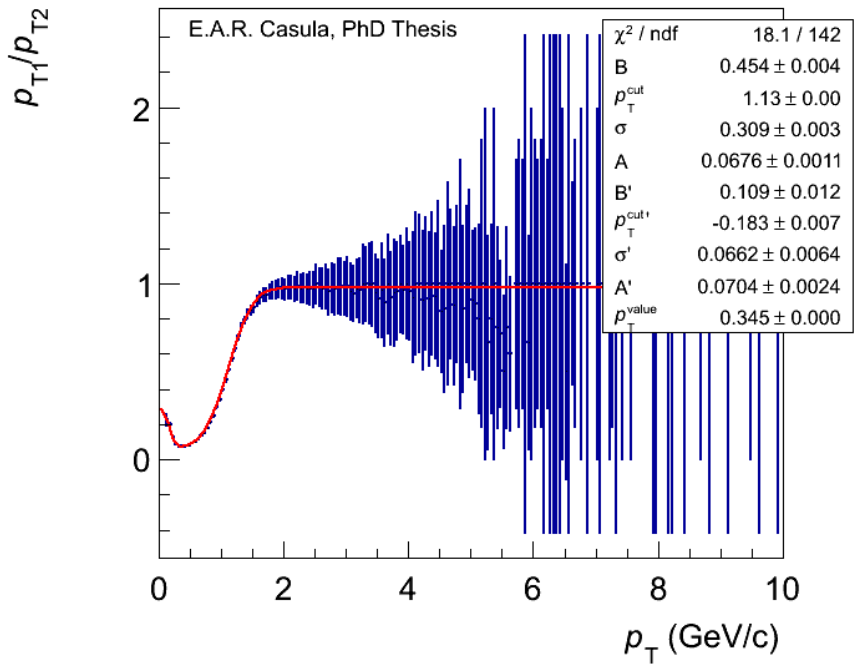

Figure 6.17: Ratio between events triggered with p_{T1} threshold over events triggered with p_{T2} threshold, as a function of p_T, fitted with the empirical function $f(p_T)$.

the empirical function:

$$f(p_T) = \begin{cases} A + B \cdot (1 + Erf(p_T - p_T^{cut})/\sqrt{2}\sigma) & \text{if } p_T < p_T^{value} \\ A' + B' \cdot (1 + Erf(p_T - p_T^{'cut})/\sqrt{2}\sigma') & \text{if } p_T > p_T^{value} \end{cases} \quad (6.2)$$

where A, A', B, B', σ, σ', p_T^{cut}, $p_T^{cut'}$ and p_T^{value} are free parameters and the function $Erf(x)$ is defined as $Erf(x) = \frac{2}{\sqrt{\pi}} \int_0^x e^{-x^2} dx$. This fit is shown in fig. 6.17.

The histograms of the embedded Monte Carlo simulations have therefore been filled requiring that the events matched the p_{T1} trigger threshold (instead of the standard p_{T2} threshold request), and at the same time weighting the dimuon histograms with f($p_T(\mu 1)$) * f($p_T(\mu 2)$), where the parameters of the functions f($p_T(\mu 1)$) and f($p_T(\mu 2)$) are the ones obtained from the above mentioned fit.

The acceptance × efficiency integrated for $2 < p_T < 5$ GeV/c has been then recalculated: the difference between this value and the one obtained in 6.3 gives the systematic uncertainty (from 0.1% to 1.9% depending on centrality).

Considering all these contributions, we can obtain the final systematic uncertainties for the four different centrality classes we have considered.
The systematic uncertainties on N_{ω}^{raw} have been calculated in the same way.
The values of systematics on N_{ϕ}^{raw} and N_{ω}^{raw} are summarized in table 6.4 and in table 6.5 respectively.

Table 6.4: Systematic uncertainties on N_{ϕ}^{raw} in different centrality bins, for dimuon $2 < p_T < 5$ GeV/c

Centrality	0-20%	20-40%	40-60%	60-90%
BKG subtraction	3.79%	$< 0.10\%$	$< 0.10\%$	$< 0.10\%$
Cut on $p_T(\mu)$	8.90%	6.67%	3.05%	3.71%
Fit function	3.41%	2.59%	3.50%	5.00%
Fit range	2.49%	1.45%	3.29%	2.08%
Tracking efficiency	4.50%	4.50%	4.50%	4.50%
Trigger efficiency	1.90%	0.10%	1.90%	0.60%
Total	11.63%	8.63%	7.51%	7.98%

Table 6.5: Systematic uncertainties on N_{ω}^{raw} in different centrality bins, for dimuon $2 < p_T < 5$ GeV/c

Centrality	0-20%	20-40%	40-60%	60-90%
BKG subtraction	2.61%	$< 0.10\%$	$< 0.10\%$	$< 0.10\%$
Cut on $p_T(\mu)$	6.44%	2.77%	1.40%	2.73%
Fit function	7.51%	12.40%	14.69%	11.11%
Fit range	5.44%	1.34%	2.33%	0.93%
Tracking efficiency	4.50%	4.50%	4.50%	4.50%
Trigger efficiency	1.90%	0.10%	1.90%	0.60%
Total	12.57%	13.57%	15.72%	12.34%

6.5 $\phi_{\mu\mu}/(\rho_{\mu\mu}+\omega_{\mu\mu})$ ratio

The $\frac{BR\sigma_{\phi}}{BR\sigma_{\rho}+BR\sigma_{\omega}}$ ratio (from now on indicated as $\phi_{\mu\mu}/(\rho_{\mu\mu}+\omega_{\mu\mu})$) has been calculated as the ratio between the raw number of ϕ and ω mesons, corrected for the acceptance×efficiency, in each centrality class. $\phi/(\rho+\omega)$ as a function of the number of participating nucleons N_{part} is shown in fig. 6.18, where the Pb-Pb values obtained in the different centrality classes with the dimuon triggers are compared to the value

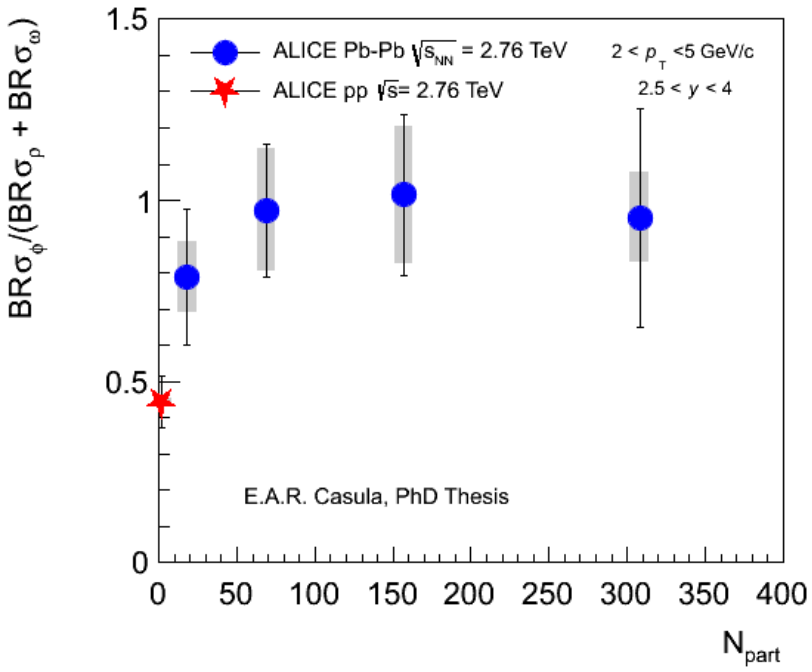

Figure 6.18: $\phi_{\mu\mu}/(\rho_{\mu\mu}+\omega_{\mu\mu})$, corrected for the acceptance×efficiency, as a function of N_{part}. Results from Pb-Pb analysis in different centrality classes are compared with pp result at 2.76 TeV.

obtained in pp analysis at 2.76 TeV with the data collected in 2011. $\phi_{\mu\mu}/(\rho_{\mu\mu}+\omega_{\mu\mu})$ in Pb-Pb increases with respect to the value in pp by a factor of about 2, and tends to saturate from peripheral towards central events, indicating an enhancement of ϕ meson with respect to ρ and ω mesons in central collisions.

6.5.1 Systematic uncertainty on $\phi_{\mu\mu}/(\rho_{\mu\mu}+\omega_{\mu\mu})$ ratio

The systematic uncertainty on $\phi_{\mu\mu}/(\rho_{\mu\mu}+\omega_{\mu\mu})$ ratio comes from the systematic uncertainties on N_ϕ^{raw} and N_ω^{raw} (see 6.4.1) and from the A×ε correction (see 6.3).
Among the contributions of N_ϕ^{raw} and N_ω^{raw} systematic uncertainty, the uncertainties on tracking and trigger efficiency (the same for both N_ϕ^{raw} and N_ω^{raw}) cancel out in the ratio, while the uncertainty related to the background subtraction is very small and has been neglected.
The uncertainty related to the A×ε correction cancel out in the ratio too.
The remaining sources are then:

- cut on single muon p_T (see 6.4.1.2);
- description of the correlated background (see 6.4.1.3);
- range of the fit to the mass spectrum (see 6.4.1.4).

The systematic uncertainties on $\phi_{\mu\mu}/(\rho_{\mu\mu}+\omega_{\mu\mu})$ are summarized in table 6.6.

Table 6.6: Systematic uncertainties on $\phi_{\mu\mu}/(\rho_{\mu\mu}+\omega_{\mu\mu})$ in different centrality classes, for dimuon $2 < p_T < 5$ GeV/c

Centrality	0-20%	20-40%	40-60%	60-90%
Background subtraction	1.25%	$< 1\%$	$< 1\%$	$< 1\%$
Cut on $p_T(\mu)$	3.37%	9.99%	1.72%	5.01%
Fit function	10.80%	16.07%	16.74%	7.86%
Mass fit range	6.71%	2.02%	1.49%	2.07%
Total	13.21%	19.03%	16.89%	9.54%

6.6 ϕ yield

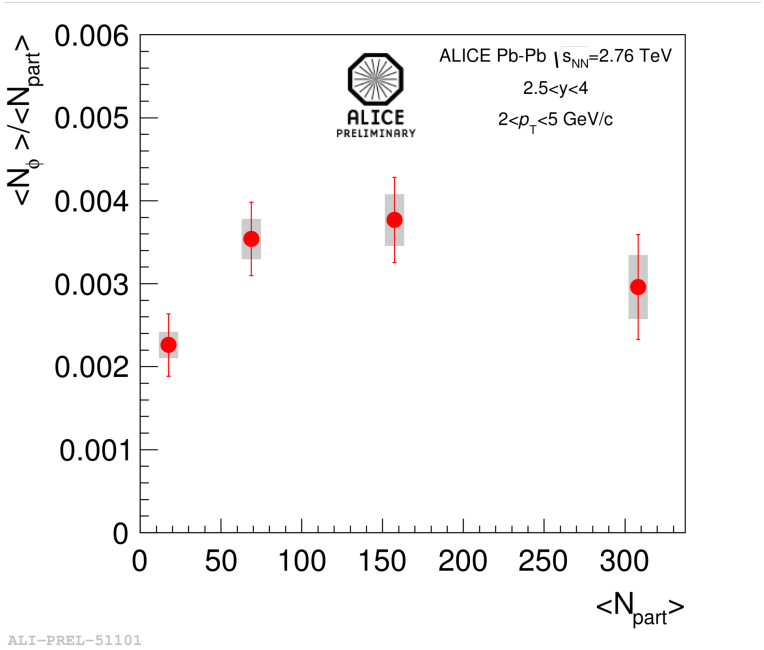

Figure 6.19: ϕ yield as a function of the number of participating nucleons.

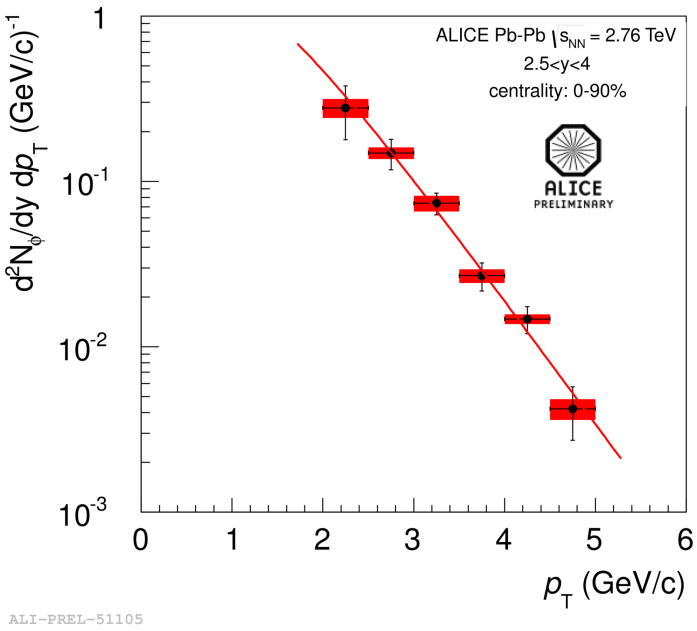

Figure 6.20: ϕ yield as a function of p_T, fitted with the Levy-Tsallis function.

The ϕ yield as a function of the number of participating nucleons has been calculated for each centrality class according to the formula

$$Y = \frac{N^{\phi}_{raw}}{A\varepsilon BR_{\phi\to e^+e^-}N_{MB}} \tag{6.3}$$

The number of minimum bias events has been obtained scaling the number of opposite sign dimuon triggers N_{OS} in each run by the normalization factor f_{norm} through the relation $N_{MB} = f_{norm} * N_{OS}$.

The normalization factor f_{norm} has been obtained through a fit with a constant to the run by run values of f^{run}_{norm}, where

$$f^{run}_{norm} = \frac{N^{trig}_{MB}}{N^{trig}_{OS\&MB}} \tag{6.4}$$

Here N^{trig}_{MB} is the number of events flagged with the minimum bias trigger and $N^{trig}_{OS\&MB}$ is the number of events triggered by both minimum bias and dimuon triggers in each run.

The final value of f_{norm} given by the fit is $f_{norm} = 27.28 \pm 0.02(\text{stat.}) \pm 0.54(\text{syst.})$ [86].

The ϕ yield as a function of the number of participating nucleons, for $2 < p_T < 5$ GeV/c, is shown in fig. 6.19. Its trend is similar to the one of the $\phi/(\rho + \omega)$ ratio, tending to saturate towards central collisions.
The yield as a function of p_T, integrated in centrality, is instead shown in fig. 6.20. The data are well fitted by the Levy-Tsallis function.

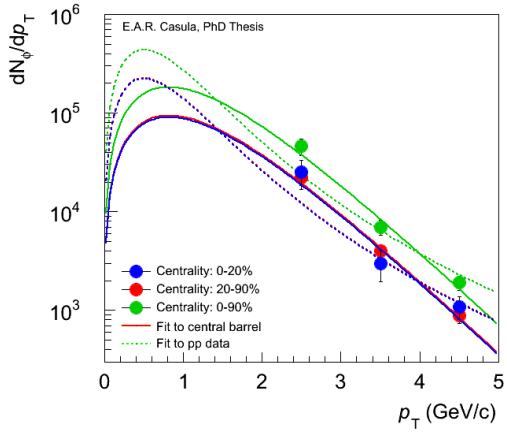

Figure 6.21: ϕ p_T distribution for different centralities compared with 2.76 TeV pp parametrization (used in our MC simulations, with dashed lines in the plot) and with the function used in $\phi \to K^+K^-$ analysis (used to resample the acceptance $\times$ efficiency, solid line).

The ϕ p_T distribution is shown in fig. 6.21 for the centrality classes 0-20 and 20-90% and integrated in centrality. Data are compared with the 2.76 TeV pp parametrization (dashed line in the plot) and with the function from $\phi \to K^+K^-$ analysis used to resample the acceptance (see 6.3, solid line in the plot). Data are clearly best described by the second function, showing the correctness of our decision to replace the 2.76 TeV pp parametrization with the one from $\phi \to K^+K^-$ analysis.
A comparison between the ϕ yield in the p_T range $2 < p_T < 5$ GeV/c per $\langle N_{part} \rangle$ as a function of $\langle N_{part} \rangle$, measured in the muon channel at forward rapidity and with the central barrel in the KK channel at midrapidity, is shown in fig. 6.22. Results from pp collisions at the same energy are shown for comparison too. While the ϕ yield in the muon channel grows from peripheral to central collisions and tends to saturate towards central collisions, the yield in the KK channel grows as a function of $\langle N_{part} \rangle$ but shows no saturation. The different yield measured in the muon and KK channels suggests a possible different hydrodynamic push at forward and midrapidity.

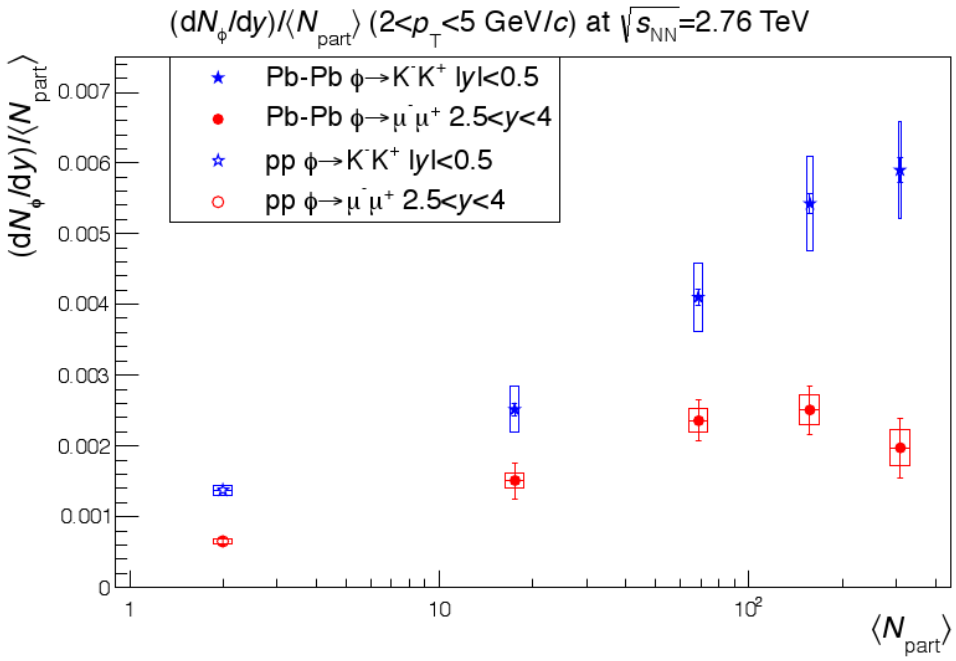

Figure 6.22: Comparison between $dN/dy/\langle N_{part}\rangle$ as a function of $\langle N_{part}\rangle$ measured in the muon channel at forward rapidity and with the central barrel in the KK channel at midrapidity, in Pb-Pb collisions at $\sqrt{s_{NN}} = 2.76$ TeV, for $2 < p_T < 5$ GeV/c. Results from pp collisions at the same energy are shown for comparison too.

6.6.1 Systematic uncertainty on ϕ yield

The systematic uncertainty on the ϕ yield comes from the systematic uncertainties on:

- N_{ϕ}^{raw} (see 6.4.1);
- acceptance × efficiency correction (already described in 6.3);
- branching ratio of ϕ in dielectrons (1%);
- scaling factor f_{norm} (2%).

These values are summarized in table 6.8.

6.7 ϕ nuclear modification factor R_{AA}

The nuclear modification factor R_{AA} (see also 1.4.0.1) is defined as the yield ratio of nucleus-nucleus collisions to inelastic pp collisions, normalized by the number of binary

Table 6.7: Systematic uncertainties on ϕ yield in different centrality classes

Centrality	0-20%	20-40%	40-60%	60-90%
N_{ϕ}^{raw}	11.63%	8.63%	7.51%	7.98%
A×ε (ϕ)	3.88%	3.32%	3.80%	4.45%
$BR_{\phi\to e^+e^-}$	1.02%	1.02%	1.02%	1.02%
f_{norm}	1.98%	1.98%	1.98%	1.98%
Total	12.46%	9.51%	8.71%	9.41%

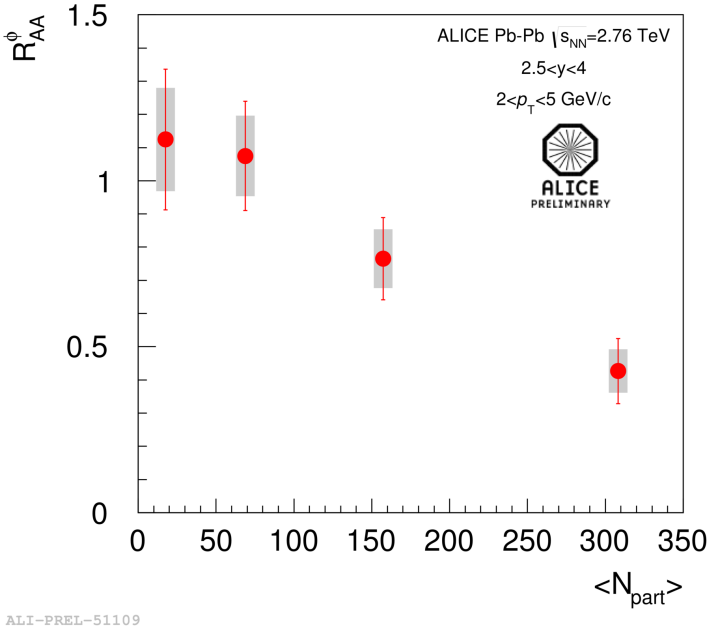

Figure 6.23: ϕ R_{AA} as a function of the number of participating nucleons.

inelastic nucleon-nucleon collisions.

The ϕ nuclear modification factor has been calculated for each centrality class in the rapidity range $2.5 < y < 4$ and in the dimuon p_T range $2 < p_T < 5$ GeV/c, through the formula:

$$R_{AA} = \frac{Y_{\phi}}{\langle T_{AA} \rangle \, \sigma_{\phi}^{pp}} \tag{6.5}$$

where Y_{ϕ} is the ϕ yield for that centrality class, $\langle T_{AA} \rangle$ is the nuclear overlap function in the same centrality class (see table 6.1) and σ_{pp} is the ϕ cross section measured in pp collisions at 2.76 TeV in the same p_T interval (see 4.5).

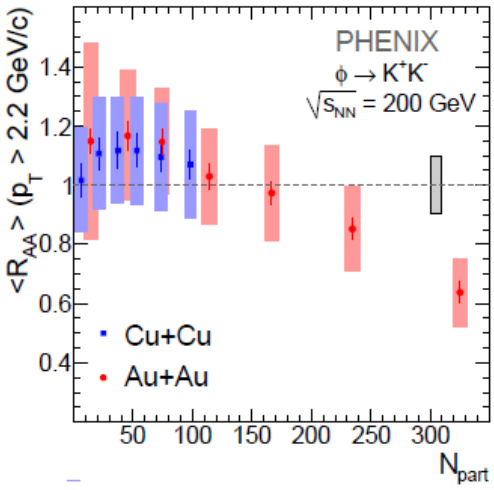

Figure 6.24: PHENIX - ϕ R_{AA} as a function of N_{part} in Au-Au and Cu-Cu collisions at $\sqrt{s_{NN}}$ = 200 GeV. The uncertainty in the determination of $\langle N_{coll} \rangle$ is shown as a box on the left.

The ϕ R_{AA} as a function of the number of participating nucleons is shown in fig. 6.23. R_{AA} is compatible with unity, within the uncertainty, in peripheral collisions, indicating that these collisions behave as a superposition of incoherent pp collisions. In the most central bin, ϕ R_{AA} value is about 0.5, showing a suppression of the ϕ yield with respect to the pp reference in the intermediate p_T region. This trend is similar to the one observed by the PHENIX experiment at similar p_T values [59] and shown in fig. 6.24. It has to be noticed that PHENIX measurement in Au-Au collisions at 200 GeV is less suppressed than ours in Pb-Pb collisions at the much higher energy of 2.76 TeV. to the energy of the collision, being more suppressed as the energy increases.

A comparison between our results in the muon channel at forward rapidity and the results obtained by the central barrel in the KK channel at midrapidity is shown in fig. 6.25. Within the uncertainties, each point measured in the dimuon channel is in agreement with the corresponding one in the hadronic channel.

It has however to be noticed that the most peripheral points of the R_{AA} in the muon channel are higher than the ones in KK, while the semicentral and especially the central points are lower, decreasing more rapidly with respect to the points in the KK channel. This is a consequence of the differences we observed in the ϕ yield in the two channels. These differences are currently under study.

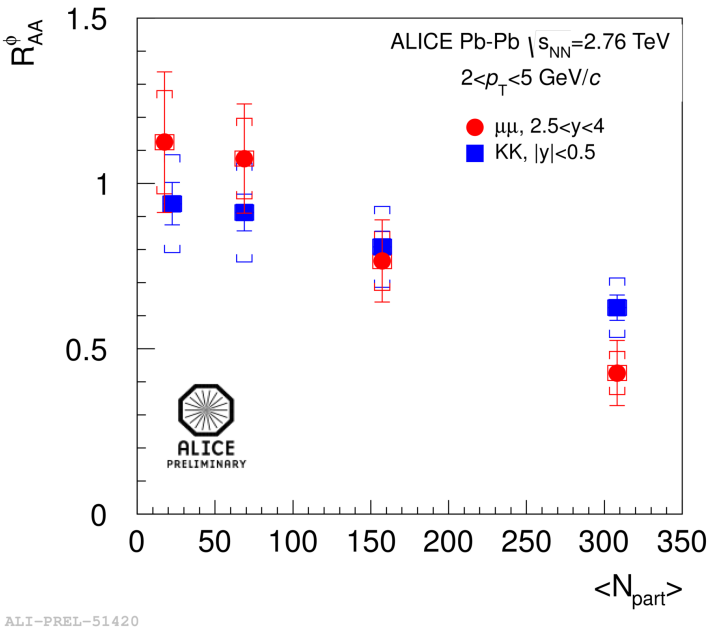

Figure 6.25: Comparison of ϕ R_{AA} as a function of N_{part} in the KK channel ($|y| < 0.5$) and in the $\mu\mu$ channel ($2.5 < y < 4$).

6.7.1 Systematic uncertainty on ϕ R_{AA}

The sources of systematic uncertainty in the evaluation of the nuclear modification factor of the ϕ meson come from the uncertainties on the yield (already discussed in 6.6.1), on the nuclear overlap functions T_{AA} and on the reference cross section measured in pp collisions at 2.76 TeV (described in 4.5.1).

These values are summarized in table 6.8.

Table 6.8: Systematic uncertainties on ϕ R_{AA} in different centrality classes, for dimuon $2 < p_T < 5$ GeV/c

Centrality	0-20%	20-40%	40-60%	60-90%
ϕ yield	13.9%	9.4%	8.4%	8.4%
T_{AA}	3.9%	4.1%	5.5%	9.7%
σ_{pp}	6.6%	6.6%	6.6%	6.6%
Total	15.9%	12.2%	12.0%	14.4%

6.8 ϕ nuclear modification factor R_{cp}

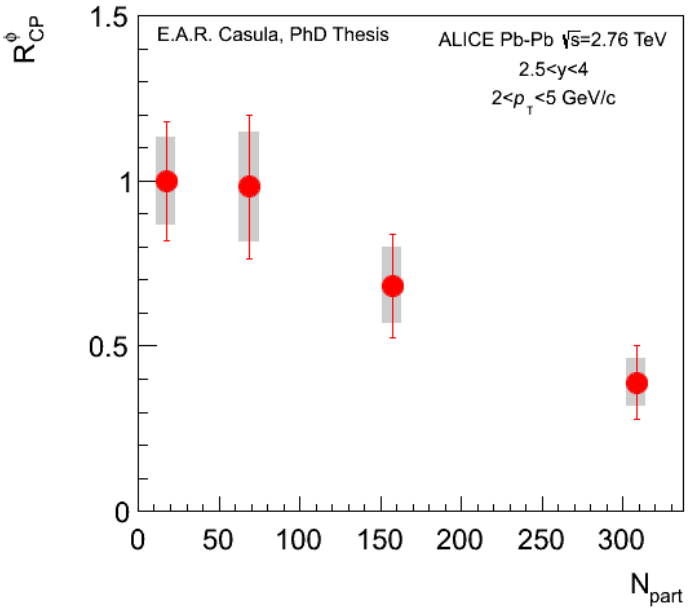

Figure 6.26: ϕ R_{cp} as a function of the number of participating nucleons

The R_{cp} (see also 1.4.0.1) is defined as the ratio of the yields in central to peripheral collisions normalized by N_{bin}.
For each centrality bin it has been calculated as:

$$R_{cp} = \frac{Y_{\phi}^{central} / \langle T_{AA} \rangle^{central}}{Y_{\phi}^{peripheral} / \langle T_{AA} \rangle^{peripheral}} \tag{6.6}$$

where the peripheral bin is the one corresponding to 60-90% centrality.
ϕ R_{cp} as a function of N_{part} is shown in fig. 6.26.
The contributions to systematic uncertainties are the ones on the ϕ yield and on T_{AA}, already described in 6.7.1.
R_{cp} is equal to unity in the most peripheral bin by definition; it is still compatible with unity for semiperipheral collisions, while it is suppressed for semicentral and central collisions.

Conclusions

The aim of this work was the study of the ϕ meson production at forward rapidity in pp, p-Pb and Pb-Pb collisions in the muon channel with the ALICE apparatus.
In pp analysis (2013 data) the ϕ differential and integrated cross sections for $1 < p_T < 5$ GeV/c and $2 < p_T < 5$ GeV/c have been extracted.
The integrated cross sections calculated in the two p_T ranges are:

$$\sigma_\phi(1 < p_T < 5\text{GeV}/c) = 0.542 \pm 0.052(\text{stat}) \pm 0.043(\text{syst})\text{mb}$$

$$\sigma_\phi(2 < p_T < 5\text{GeV}/c) = 0.1082 \pm 0.0095(\text{stat}) \pm 0.0071(\text{syst})\text{mb}$$

Comparison with PHOJET and with the PYTHIA tunes Perugia-0, Perugia-11, ATLAS-CSC and D6T shows that the PYTHIA tunes Perugia-0 and Perugia-11 strongly underestimate the measured cross section; PYTHIA ATLAS-CSC also underestimates the data (even if to a lesser degree than Perugia-0 and Perugia-11), while PYTHIA D6T slightly overestimates them. PHOJET is instead in good agreement with the measured values.
In p-Pb analysis (2013 data), the ϕ yield as a function of p_T, together with the ϕ nuclear modification factor R_{pPb} as a function of p_T at both forward and backward rapidities, and the nuclear modification factor R_{FB} in the common rapidity window between forward and backward rapidities have been extracted.
ϕ R_{pPb} at forward rapidity is compatible with unity for $p_T > 3$ GeV/c and it is larger at backward rapidity. This effect is due to the asymmetry in the particle production present between forward and backward rapidities.
The comparison between ϕ R_{pA}, obtained in the muon channel at both forward and backward rapidities, and the R_{pA} of the charged particles measured with the Central Barrel in the kaon channel at midrapidity, for $|\eta| < 0.3$, shows that the ϕ R_{pA} shape is similar to the one of the charged particles, even if its values are smaller in the entire

p_T range in the case of forward rapidity. The R_{pA} of the charged particles sits between the ϕ R_{pA} at forward and backward rapidities.

The yield ratio of forward to backward rapidity R_{FB} as a function of p_T, in the common rapidity window $2.96 < |y_{cm}| < 3.53$ between forward and backward rapidities, is constant within uncertainties; its integrated value in the range $1.5 < p_T < 7$ GeV/c is 0.53 ± 0.03, differing from unity by 47%: this is a consequence of the asymmetry in the particle production present between forward and backward rapidities.

In Pb-Pb analysis (2011 data), the $\frac{BR\sigma_\phi}{BR\sigma_\rho + BR\sigma_\omega}$ ratio and of the ϕ nuclear modification factors R_{AA} and R_{cp} as a function of the number of participating nucleons N_{part} have been extracted.

The comparison of $\phi_{\mu\mu}/(\rho_{\mu\mu} + \omega_{\mu\mu})$ ratio with the value obtained in pp analysis at 2.76 TeV shows that $\phi_{\mu\mu}/(\rho_{\mu\mu} + \omega_{\mu\mu})$ in Pb-Pb increases with respect to the value in pp by a factor of about 2, and tends to saturate from peripheral towards central events, indicating an enhancement of ϕ meson with respect to ρ and ω mesons in central collisions.

The comparison between the ϕ yield in the intermediate p_T range $2 < p_T < 5$ GeV/c per N_{part} as a function of N_{part}, measured in the muon channel at forward rapidity and with the central barrel in the KK channel at midrapidity, shows two different behaviors: the ϕ yield in the muon channel grows from peripheral to central collisions and tends to saturate towards central collisions, while the yield in the KK channel grows as a function of N_{part} but shows no saturation. This effect may be due to a possible different hydrodynamic push at forward and at midrapidity.

The ϕ R_{AA} as a function of the number of participating nucleons is compatible with unity, within the uncertainty, in peripheral collisions, indicating that these collisions behave as a superposition of incoherent pp collisions. In the most central bin, ϕ R_{AA} value is about 0.5, showing a suppression of the ϕ yield with respect to the pp reference in the intermediate p_T region.

A comparison between ϕ R_{AA} in the muon channel at forward rapidity and the ϕ R_{AA} measured by the central barrel in the KK channel at midrapidity shows that, within the uncertainties, each point measured in the dimuon channel is in agreement with the corresponding one in the kaon channel. However, the most peripheral points of the R_{AA} in the muon channel are higher than the ones in KK, while the semicentral and especially the central points are lower: this is a consequence of the differences between

forward and midrapidity observed before in the ϕ yield. These differences are still under investigation.

ϕ R_{cp} is equal to unity in the most peripheral bin by definition; it is compatible with unity for semiperipheral collisions and it is suppressed for semicentral and central collisions.

List of runs

List of LHC13g runs (pp analysis)

197692, 197669, 197643, 197616, 197613, 197611, 197608, 197606, 197584, 197583, 197555, 197553, 197501, 197500, 197499, 197497, 197471, 197470

List of LHC13d runs (p-Pb analysis)

195682, 195724, 195725, 195726, 195727, 195760, 195765, 195767, 195783, 195787, 195826, 195827, 195829, 195830, 195831, 195867, 195869, 195871, 195872, 195873

List of LHC13e runs (p-Pb analysis)

196311, 196310, 196309, 196308, 196214, 196201, 196200, 196199, 196194, 196187, 196185, 196107, 196105, 196091, 196090, 196089, 196085, 196006, 196000, 195994, 195989, 195958, 195955, 195954, 195950, 195949

List of LHC13f runs (Pb-p analysis)

197388, 197387, 197386, 197349, 197348, 197342, 197341, 197302, 197299, 197298, 197258, 197256, 197255, 197254, 197247, 197189, 197184, 197153, 197152, 197150, 197148, 197147, 197145, 197144, 197143, 197142, 197139, 197138, 197099, 197098, 197092, 197091, 197089, 197011, 197003, 196974, 196973, 196972, 196965, 196876, 196869, 196774, 196773, 196722, 196721, 196720, 196702, 196701, 196648, 196646, 196608, 196605, 196601, 196568, 196566, 196564, 196563, 196535, 196528, 196477, 196475, 196474, 196433

List of LHC11h runs (Pb-Pb analysis)

170593, 170572, 170390, 170389, 170388, 170387, 170313, 170312, 170311, 170309, 170308, 170306, 170270, 170269, 170268, 170230, 170228, 170207, 170204, 170203, 170193, 170163, 170162, 170159, 170155, 170091, 170089, 170088, 170085, 170084, 170083, 170081, 170040, 170036, 170027, 169969, 169965, 169859, 169858, 169855, 169846, 169838, 169837, 169835, 169683, 169590, 169588, 169587, 169586, 169557, 169555, 169554, 169553, 169550, 169515, 169512, 169506, 169504, 169498, 169475,

169420, 169419, 169418, 169417, 169415, 169411, 169238, 169236, 169167, 169160, 169156, 169148, 169145, 169144, 169138, 169099, 169094, 169091, 169045, 169044, 169040, 169035, 168992, 168826, 168777, 168514, 168512, 168511, 168467, 168464, 168461, 168460, 168458, 168362, 168361, 168342, 168341, 168325, 168322, 168318, 168311, 168310, 168213, 168212, 168208, 168207, 168206, 168205, 168203, 168181, 168175, 168173, 168172, 168115, 168108, 168107, 168076, 168069, 168066, 167988, 167987, 167986, 167985, 167921, 167920, 167915, 167818, 167814, 167813, 167808, 167807, 167806, 167713, 167706

Bibliography

[1] B. Povh, K. Rith, C. Scholz and F. Zetsche. *Particles and Nuclei - An Introduction to the Physical Concepts*. Springer, 2008. 5

[2] T. Åkesson et al. (HELIOS-1 collaboration). Low-Mass Lepton-Pair Production in p-Be Collisions at 450 GeV/c. *Z. Phys. C*, 68:47, 1995. 6

[3] B. Abelev et al. (ALICE collaboration). Light Vector Meson Production in pp Collisions at $\sqrt{s} = 7$ TeV. *Phys. Lett. B*, 710:557, 2012. 6, 44, 54

[4] L.G. Landsberg et al. Electromagnetic Decays of Light Mesons. *Phys. Rep.*, 128:301, 1985. 7

[5] H. Satz. *Extreme States of Matter in Strong Interaction Physics*. Springer, 2012. 9, 11, 12

[6] R. Baier et al. Bottom-Up Thermalization in Heavy Ion Collisions. *Phys. Lett. B*, 502:51, 2001. 9

[7] N. Brambilla et al. *Heavy Quarkonium Physics*. CERN-2005-005, 2005. 10

[8] R. Arnaldi et al. (NA60 collaboration). NA60 Results on Thermal Dimuons. *Eur. Phys. J. C*, 61:711, 2009. 11

[9] A. Adare et al. (PHENIX collaboration). Detailed Measurement of the e^+e^- Pair Continuum in p+p and Au+Au Collisions at $\sqrt{s_{NN}}$=200 GeV and Implications for Direct Photon Production. *Phys. Rev. C*, 81:034911, 2009. 11

[10] H. Satz. Color Deconfinement in Nuclear Collisions. *Rept. Prog. Phys.*, 63:1511, 2000. 11

[11] Z. Fodor and S.D. Katz. Critical Point of QCD at Finite T and mu, Lattice Results for Physical Quark Masses. *JHEP*, 0404:050, 2004. 11

[12] S. Ejiri et al. Study of QCD Thermodynamics at Finite Density by Taylor Expansion. *Progr. Theor. Phys. Suppl.*, 153:118, 2004. 11

[13] W. Weise. Phases of Strongly Interacting Matter. In *Gordon Conference on Photonuclear Reactions*, 2012. 12

[14] J. Kogut et al. Scales of chiral symmetry breaking in quantum chromodynamics. *Phys. Rev. Lett.*, 48:1140–1143, 1982. 13

[15] K. Fukushima. Relation Between the Polyakov Loop and the Chiral Order Parameter at Strong Coupling. *Phys. Rev. D*, 68:045004, 2003. 13

[16] T. Banks and A. Casher. Chiral Symmetry Breaking in Confining Theories. *Nucl. Phys. B*, 169:103–125, 1980. 13

[17] S. Okubo. ϕ-meson and Unitary Symmetry Model. *Phys. Lett.*, 5:165 – 168, 1963. 13

[18] G. Zweig. An SU(3) Model for Strong Interaction Symmetry and its Breaking. *CERN Report Nos. TH-401 and TH-412*, 1964. 13

[19] J. Iizuka, K. Okada and O. Shito. Systematics and Phenomenology of Boson Mass Levels. III. *Progr. Theor. Phys.*, 35:1061–1073, 1966. 13

[20] J. Rafelski and B. Müller. Strangeness Production in the Quark-Gluon Plasma. *Phys. Rev. Lett.*, 48:1066–1069, Apr 1982. 13

[21] J. Rafelski. Strangeness Production in the Quark-Gluon Plasma. *Nucl. Phys. A*, 418:215 – 235, 1984. 13

[22] P. Koch, B. Müller and J. Rafelski. Strangeness Production And Evolution in Quark-Gluon Plasma. *Z. Phys. A*, 324:453–463, 1986. 13

[23] A. Shor. ϕ-Meson Production as a Probe of the Quark-Gluon Plasma. *Phys. Rev. Lett.*, 54:1122–1125, Mar 1985. 13

[24] H. Sorge. Flavor Production in Pb (160 AGeV) on Pb Collisions: Effect of Color Ropes And Hadronic Rescattering. *Phys. Rev. C*, 52:3291–3314, 1995. 14

[25] M. Bleicher et al. Relativistic Hadron-Hadron Collisions in The Ultra-Relativistic Quantum Molecular Dynamics Model. *J. Phys. G*, 25:1859, 1999. 14

[26] J.Adams et al. (STAR collaboration). ϕ Meson Producton in Au+Au and p+p Collisions at $\sqrt{s_{NN}} = 200$ GeV. *Phys. Lett. B*, 612:181–189, 2005. 14

[27] B. Abelev et al. (STAR collaboration). Measurements of ϕ Meson Production in Relativistic Heavy Ion Collisions at RHIC. *Phys. Rev. C*, 79:064903, 2009. 14, 21

[28] M. Asakawa and C.M. Ko. ϕ Meson Mass in Hot and Dense Matter. *Nucl. Phys. A*, 572:732 – 748, 1994. 14

[29] C. Song. Effective Mass of Phi Mesons at Finite Temperature. *Phys. Lett. B*, 388:141 – 146, 1996. 14

[30] M. Asakawa and C.M. Ko. Seeing the QCD Phase Transition with ϕ Mesons. *Phys. Lett. B*, 322:33 – 37, 1994. 14

[31] K. Haglin. Collision Rates for ρ-, ω- and ϕ-Mesons at Nonzero Temperature. *Nucl. Phys. A*, 584:719 – 736, 1995. 14

[32] W. Smith and K.L. Haglin. Collision Broadening of the ϕ Meson in Baryon Rich Hadronic Matter. *Phys. Rev. C*, 57:1449–1453, 1998. 14

[33] C.M. Ko and D. Seibert. What Can We Learn from a Second ϕ Meson Peak in Ultrarelativistic Nuclear Collisions? *Phys. Rev. C*, 49:2198–2202, 1994. 14

[34] R. Muto et al. (KEK-PS E325 Collaboration). Evidence for In-Medium Modification of the ϕ Meson at Normal Nuclear Density. *Phys. Rev. Lett.*, 98:042501, 2007. 14

[35] F. Sakuma et al. (KEK-PS E325 Collaboration). Nuclear-Matter Modification of Decay Widths in the $\phi \to e^+e^-$ and $\phi \to K^+K^-$ Channels. *Phys. Rev. Lett.*, 98:152302, 2007. 14

[36] C. Adler et al. (STAR Collaboration). Azimuthal Anisotropy of K^0_S and $\Lambda + \bar{\Lambda}$ Production at Midrapidity from Au + Au Collisions at $\sqrt{s_{NN}} = 130$ GeV. *Phys. Rev. Lett.*, 89:132301, 2002. 14

[37] S.S. Adler et al. (PHENIX Collaboration). Elliptic Flow of Identified Hadrons in Au + Au Collisions at $\sqrt{s_{NN}} = 200$ GeV. *Phys. Rev. Lett.*, 91:182301, 2003. 14

[38] J. Adams et al. (STAR Collaboration). Experimental and Theoretical Challenges in the Search for the Quark Gluon Plasma: The STAR Collaboration's Critical Assessment of the Evidence from RHIC Collisions. *Nucl. Phys. A*, 757:102, 2005. 14

[39] H. Sorge. Highly Sensitive Centrality Dependence of Elliptic Flow: A Novel Signature of the Phase Transition in QCD. *Phys. Rev. Lett.*, 82:2048–2051, 1999. 14

[40] P. Huovinen, P.F. Kolb, U.W. Heinz, P.V. Ruuskanen and S.A. Voloshin. Radial and Elliptic Flow at RHIC: Further Predictions. *Phys. Lett. B*, 503:58–64, 2001. 14

[41] Z.W. Lin and C.M. Ko. Flavor Ordering of Elliptic Flows at High Transverse Momentum. *Phys. Rev. Lett.*, 89:202302, 2002. 14

[42] V. Greco, C.M. Ko and P. Lévai. Parton Coalescence and Anti-Proton / Pion Anomaly at RHIC. *Phys. Rev. Lett.*, 90:202302, 2003. 14, 15

[43] R.J. Fries, B. Müller, C. Nonaka and S.A. Bass. Hadron Production in Heavy Ion Collisions: Fragmentation and Recombination from a Dense Parton Phase. *Phys. Rev. C*, 68:044902, 2003. 14, 22

[44] D. Molnár and S.A. Voloshin. Elliptic Flow at Large Transverse Momenta from Quark Coalescence. *Phys. Rev. Lett.*, 91:092301, 2003. 14, 15

[45] R. J. Fries, B. Müller, C. Nonaka, and S. A. Bass. Hadronization in heavy-ion collisions: Recombination and fragmentation of partons. *Phys. Rev. Lett.*, 90:202303, 2003. 15, 22

[46] M.L. Miller, K. Reygers, S.J. Sanders, P. Steinberg. Glauber Modeling in High-Energy Nuclear Collisions. *Annu. Rev. Nucl. Part. Sci.*, 57:205, 2007. 15

[47] M.C. Abreu et al. (NA38 collaboration). Production of $\rho + \omega$ and ϕ in p-W and S-U Collisions at 200 GeV/nucleon. *Phys. Lett. B*, 368:239, 1996. 16

[48] B. Alessandro et al. (NA50 collaboration). ϕ Production in Pb-Pb Collisions at 158 GeV/c per Nucleon Incident Momentum. *Phys. Lett. B*, 555:147, 2003. 16

[49] D. Jouan (NA50 collaboration). The Production of ϕ, ω and ρ Mesons in p-, d-, S- and Pb- Induced Reactions at the CERN SPS. *Nucl. Part. Phys.*, 30:S277, 2004. 16

[50] C. Alt et al. (NA49 collaboration). Energy Dependence of ϕ Meson Production in Central Pb+Pb Collisions at $\sqrt{s_{NN}} = 6$ to 17 GeV. *Phys. Rev. C*, 78:044907, 2008. 18

[51] D. Adamová et al. (CERES collaboration). Leptonic and Charged Kaon Decay Modes of the ϕ Meson Measured in Heavy-Ion Collisions at the CERN Super Proton Synchrotron. *Phys. Rev. Lett.*, 96:152301, 2006. 18

[52] S.C. Johnson, B.V. Jacak, A. Drees. Rescattering of Vector Meson Daughters in High Energy Heavy Ion Collisions. *Eur. Phys. J. C*, 18:645, 2001. 19

[53] S. Pal, C.M. Ko, Z.-W. Lin. ϕ Meson Production in Relativistic Heavy Ion Collisions. *Nucl. Phys. A*, 707:525, 2002. 19

[54] A. De Falco (NA60 collaboration). NA60 Results on ϕ Production in the Hadronic and Leptonic Channels in In-In Collisions at 158 GeV. *Nucl. Phys. A*, 830:753c, 2009. 19

[55] R. Arnaldi et al. (NA60 collaboration). A Comparative Measurement of $\phi \to K^+K^-$ and $\phi \to mu^+mu^-$ in In-In Collisions at the CERN SPS. *Phys. Lett. B*, 699:325, 2011. 19

[56] J.W. Cronin et al. Production of Hadrons at Large Transverse Momentum at 200, 300, and 400 GeV. *Phys. Rev. D*, 11:3105–3123, 1975. 22

[57] D. Antreasyan et al. Production of Hadrons at Large Transverse Momentum in 200-, 300-, and 400-GeV p-p and p-Nucleus Collisions. *Phys. Rev. D*, 19:764–778, 1979. 22

[58] P.B. Straub et al. Nuclear Dependence of High-x_t Hadron and High-τ Hadron-Pair Production in p-A Interactions at $\sqrt{s}$ = 38.8 GeV. *Phys. Rev. Lett.*, 68:452–455, 1992. 22

[59] A. Adare et al. (PHENIX collaboration). Nuclear Modification Factors of ϕ Meson in d+Au, Cu+Cu and Au+Au Collisions at $\sqrt{s_{NN}}$ = 200 GeV. *Phys. Rev. C*, 83:024909, 2011. 24, 25, 112

[60] B. Alessandro et al. (ALICE collaboration). ALICE: Physics Performance Report, Volume II. *Nucl. Part. Phys.*, 32:1295, 2006. 28

[61] K. Aamodt et al. (ALICE collaboration). The ALICE Experiment at The CERN LHC. *JINST*, 3:S08002, 2008. 28

[62] A. Akindinov et al. Performance of the ALICE Time-Of-Flight Detector at the LHC. *Eur. Phys. J. Plus*, 128:44, 2013. 33

[63] L. Aphecetche et al. (ALICE collaboration). Numerical Simulations and Offline Reconstruction of the Muon Spectrometer of ALICE. *https://edms.cern.ch/document/1054937/1*, 2009. 44

[64] E. Incani. *Light Vector Meson Production at Forward Rapidity in pp Collisions at the LHC with the ALICE Detector*. PhD Thesis, 2013. 44, 49, 54, 92

[65] T. Sjöstrand et al. PYTHIA 6.4 Physics and Manual. *JHEP*, 0605:026, 2006. 44, 64

[66] P.Z. Skands. The Perugia tunes. *arXiv:0905.3418*, 2009. 44, 64

[67] K. Reygers (ALICE collaboration). Production of Neutral Pions and Eta-Mesons in pp Collisions Measured with ALICE. *J. Phys. G*, 38:124076, 2011. 46

[68] I. Abt et al. (HERA-B collaboration). K_0^* and ϕ Meson Production in Proton-Nucleus Interactions at $\sqrt{s}$ = 41.6 GeV. *Eur. Phys. J.*, 50:315, 2007. 46

[69] R. Arnaldi et al. (NA60 collaboration). Study of the Electromagnetic Transition Form-Factors in $\eta \to \mu^+\mu^-\gamma$ and $\omega \to \mu^+\mu^-\pi^0$ Decays with NA60. *Phys. Lett. B*, 677:260, 2009. 47

[70] L.G. Landsberg et al. Electromagnetic Decays of Light Mesons. *Phys. Rep.*, 128:301, 1985. 47

[71] S. van der Meer. ISR-PO/68-31. *KEK 68-64*. 50

[72] R. Engel. Photoproduction within the Two-Component Dual Parton Model: Amplitudes and Cross Sections. *Z. Phys. C*, 66:203, 1995. 64

[73] R. Engel and J. Ranft. Hadronic photon-photon interactions at high energies. *Phys. Rev. D*, 54:4244, 1996. 64

[74] P.Z. Skands. Tuning Monte Carlo Generators: The Perugia Tunes. *Phys. Rev. D*, 82:074018, 2010. 64

[75] C.M. Buttar, D. Clements, I. Dawson, A. Moraes. Simulations of Minimum Bias Events and the Underlying Event, MC Tuning and Predictions for the LHC. *Acta Phys. Pol. B*, 35:433, 2004. 64

[76] R. Field. Physics at the Tevatron. *Acta Phys. Pol. B*, 39:2611, 2008. 64

[77] B.B. Back et al. (PHOBOS collaboration). Pseudorapidity Distribution of Charged Particles in d+Au Collisions at $\sqrt{s_{NN}} = 200$ GeV. *Phys. Rev. Lett.*, 93:082301, 2004. 76

[78] G.J. Alner et al. (UA5 collaboration). Scaling of Pseudorapidity Distributions at c.m. Energies Up to 0.9-TeV. *Z. Phys. C*, 33:1, 1986. 76

[79] K. Aamodt et al. (ALICE collaboration). Rapidity and Transverse Momentum Dependence of Inclusive Production in pp Collisions at $\sqrt{s} = 7$ TeV. *Phys. Lett. B*, 704:442, 2011. 77

[80] X.N. Wang and M. Gyulassy. HIJING: A Monte Carlo Model for Multiple Jet Production in p p, p A and A A Collisions. *Phys. Rev. D*, 44:3501, 1991. 78

[81] S. Roesler, R. Engel, J.Ranft. The Monte Carlo Event Generator DPMJET-III. *arXiv:hep-ph/0012252*, 2000. 78

[82] K. Aamodt et al. (ALICE collaboration). Centrality Dependence of the Charged-Particle Multiplicity Density at Midrapidity in Pb-Pb Collisions at $\sqrt{s_{NN}} = 2.76$ TeV. *Phys. Rev. Lett.*, 106:032301, 2011. 81, 88

[83] B. Abelev et al. (ALICE collaboration). Transverse Momentum Distribution and Nuclear Modification Factor of Charged Particles in p+Pb Collisions at $\sqrt{s} = 5.02$ TeV. *Phys. Rev. Lett.*, 110:082302, 2013. 83

[84] B.B. Back et al. (PHOBOS collaboration). Pseudorapidity Dependence of Charged Hadron Transverse Momentum Spectra in d+Au Collisions at $\sqrt{s_{NN}} = 200$ GeV. *Phys. Rev. C*, 70:061901, 2004. 84

[85] I. Arsene et al. (BRAHMS collaboration). Evolution of the Nuclear Modification Factors with Rapidity and Centrality in d+Au Collisions at $\sqrt{s_{NN}} = 200$ GeV. *Phys. Rev. Lett.*, 93:242303, 2004. 85

[86] R. Arnaldi, A. Lardeux, P. Pillot, C. Suire, L. Valencia Palomo. J/ψ production in Pb-Pb collisions at $\sqrt{s} = 2.76$ TeV. *Analysis note*, 2013. 102, 108